RESPONSE OF MAJOR MODES OF EASTERN ARCTIC OCEAN VARIABILITY TO CLIMATE CHANGE

TILL M. BAUMANN

A Dissertation Submitted in Partial Fulfillment of the Requirements
for the Degree of

Doctor of Philosophy

in

Atmospheric Sciences

University of Alaska Fairbanks

December 2019

APPROVED:
Igor V. Polyakov, *Committee Chair*
Uma S. Bhatt, *Committee Member*
John E. Walsh, *Committee Member*
Thomas J. Weingartner, *Committee Member*
Javier G. Fochesatto, *Chair*
Department of Atmospheric Sciences
Kinchel Doerner, *Dean*
College of Natural Sciences and Mathematics
Michael Castellini, *Dean of the Graduate School*

ABSTRACT

The Arctic Ocean plays a central role in ongoing climate change, with sea ice loss being the most prominent indicator. Recent observations showed that Atlantic inflows play an increasingly important role in the demise of sea ice. This encroaching *atlantification* of the eastern Arctic Ocean impacts the mean state and the variability of hydrography and current dynamics throughout the basin. Among the most energetic modes of variability are the seasonal cycle and high frequency semidiurnal ($\sim$12-hourly) dynamics in the tidal and inertial frequency band. Limited observations indicated a substantial increase of both, hydrographic seasonal cycles as well as semidiurnal current dynamics in the eastern Arctic over the last decade. Using a uniquely comprehensive data set from an array of six moorings deployed across the eastern Eurasian Basin (EB) continental slope along the 125°E meridian between 2013 and 2015 within the NABOS project, we assess the state of hydrographic seasonal cycles in the eastern EB. Results show a complex pattern of seasonality with a remarkably strong (ΔT=1.4°C), deep reaching ($\sim$600 m) temperature signal over the continental slope and large-scale seasonal displacements of isopycnal interfaces. Seasonally changing background conditions are also the main source of variability of semidiurnal frequency band currents: During winter, vigorous baroclinic tidal currents whose amplitudes by far exceed predictions follow the vertical evolution of the pycnocline. During summer, extensive open-water periods additionally lead to strong wind-driven inertial currents in the upper ocean, routinely exceeding 30 cm/s far offshore in the deep basin. In order to obtain an Arctic-wide perspective on the impact of baroclinic tidal currents, a pan-Arctic tidal current atlas has been developed that

synthesizes all available observations from the last 20 years. This atlas allows for in-depth studies of regional baroclinic tidal current variability as well as for validation of ocean and climate models, an essential step towards more accurate projections of the future Arctic Ocean state. Our findings from the eastern EB region already indicate a new, more dynamic state of the eastern Arctic Ocean with direct implications for the ecosystem and further sea-ice reduction.

PUBLICATIONS

PUBLISHED

Baumann, T.M., Polyakov, I.V., Pnyushkov, A.V., Rember, R., Ivanov, V.V., Alkire, M.B., Goszczko, I. and Carmack, E.C., 2018. On the Seasonal Cycles Observed at the Continental Slope of the Eastern Eurasian Basin of the Arctic Ocean. Journal of Physical Oceanography, 48(7), pp.1451-1470.

Polyakov, I.V., Pnyushkov, A.V., Alkire, M.B., Ashik, I.M., **Baumann, T.M.**, Carmack, E.C., Goszczko, I., Guthrie, J., Ivanov, V.V., Kanzow, T. and Krishfield, R., 2017. Greater role for Atlantic inflows on sea-ice loss in the Eurasian Basin of the Arctic Ocean. Science, 356(6335), pp.285-291.

Pnyushkov, A.V., Polyakov, I.V., Rember, R., Ivanov, V.V., Alkire, M.B., Ashik, I.M., **Baumann, T.M.**, Alekseev, G.V. and Sundfjord, A., 2018. Heat, salt, and volume transports in the eastern Eurasian Basin of the Arctic Ocean from 2 years of mooring observations. Ocean Science, 14(6), pp.1349-1371.

SUBMITTED

Baumann, T.M., Polyakov, I.V., Padman, L., Danielson, S., Fer, I., Howard, S., Hutchings, J., Janout M., Nguyen, A., Pnyushkov, A.V., submitted. Semidiurnal Dynamics in the Arctic Ocean's Eastern Eurasian Basin. Journal of Physical Oceanography.

IN PREPARATION

Baumann, T.M., Polyakov, I.V., Padman, L. Pnyushkov, A. V., in preparation. Pan-Arctic Tidal Current Atlas. Nature Scientific Data.

Polyakov, I.V., Rippeth, T.P., Fer, I., **Baumann, T.M.**, Carmack, E.C., Ivanov, V.V., Janout, M., Padman, L., Pnyushkov, A.V. and Rember, R., in preparation. Transition to a new ocean dynamic regime in the eastern Arctic Ocean. Geophysical Research letters.

Polyakov, I.V., Rippeth, T.P., Fer, I., Alkire, M.B., **Baumann, T.M.**, Carmack, E.C., Ingvaldsen, R.B., Ivanov, V.V., Janout, M., Lind, S., Padman, L., Pnyushkov, A.V. and Rember, R., in preparation. Transition to a new ocean mixing regime increases eastern Arctic sea ice loss to Atlantic Ocean heat. Bulletin of the American Meteorological Society.

ACKNOWLEDGMENTS

Completing this dissertation would not have been possible without the support of my colleagues, friends and family! First and foremost, I would like to express my sincere gratitude to my academic adviser Igor Polyakov. His contagious passion for science and the resulting joyfully zealous scientific arguments greatly benefited me and my work. Further, I want to thank my committee members Uma Bhatt, John Walsh and Tom Weingartner, whose guidance and feedback smoothed the way throughout my studies.

Among the excellent co-authors I had the pleasure to work with and learn from, special thanks are due to Andrey Pnyushkov and Laurie Padman whose many constructive contributions played a substantial role in shaping this dissertation.

The two expeditions into the Arctic Ocean aboard the Russian icebreaker *Akademik Tryoshnikov* were outstanding experiences, in no small part due to the stimulating atmosphere created by many colleagues and friends aboard. I want to especially thank Ian Waddington for his mentorship in all things mooring and setting an inspiring example of seamanship.

Since life does not only happen behind desks and on ships, wholehearted thanks are also due to my friends that made Alaska home over the last four years and helped to create a healthy balance between work and adventure! Cheers to Sandro Dahlke and Sebastian Milinski for their friendship, support and banter on our parallel journeys through academia.

Last but not least, I thank my parents Christine and Ralf and my sister Silva for their loving support and for always being there.

TABLE OF CONTENTS

Page

LIST OF FIGURES

Page

LIST OF TABLES

Page

1

INTRODUCTION

1.1 ARCTIC CHANGE

The Arctic is warming almost twice as fast as the rest of the northern hemisphere (e.g. Bekryaev et al. 2010), a process known as Arctic amplification. Other climate-relevant measures of ocean, land and atmosphere also exhibit strongest trends in the Arctic domain (e.g. Serreze and Barry 2011). Among the metrics quantifying global climate change, Arctic sea ice loss is arguably the most prominent.

1.2 ARCTIC SEA ICE

The highly variable sea ice cover is a defining attribute of the Arctic Ocean. As a key element of the climate and ecosystem and as a major navigational hazard, its characteristics have been the subject of scientific investigations since the early days of Arctic exploration. Apart from the land fast ice found on the shallow shelves, Arctic sea ice is highly mobile and constantly shifts position due to wind and oceanic currents. The seasonal cycle dominates Arctic sea ice variability. The amplitude of the seasonal freeze-thaw cycle of sea ice in terms of area is $\sim$7M km^2 or about half of the maximum winter extent of $\sim$13-14M km^2 (at the beginning of the satellite era in 1978 (Cavalieri and Parkinson 2012)). Under current conditions, 65% of late-winter Arctic sea ice is purely seasonal and is either melted in summer or exported out of the Arctic domain before the onset of the next freezing cycle (Carmack et al. 2016). The remaining fraction

is multiyear ice that survived one or more summer seasons. In order to survive summer ablation, it has to be at least 2-3 m thick (Maykut and Untersteiner 1971; Flato and Brown 1996) which can be achieved through thermodynamic ice growth or ridging. Thick ice is mostly found on the North American side of the Arctic margin. Loss of multiyear ice occurs if summer ablation exceeds winter formation rates or if the ice is exported out of the Arctic domain before it melts.

Recent decades have seen an accelerated reduction of sea ice throughout the Arctic during all seasons (e.g. Serreze et al. 2007; Stroeve et al. 2012; Carmack et al. 2015). From a dataset based on a variety of historic sources ranging from hand-written observations from whaling captains in the 19th century to government agency reports of various Nordic countries, Walsh et al. (Walsh et al. 2017) concluded that the recent rate of sea-ice retreat and its current minimum extent of $\sim$5M km^2 is without precedent in the records dating back to 1850. Although sea ice is currently retreating in all seasons, there is a great seasonal difference in these trends. Over the satellite era, monthly anomalies show a declining trend of sea ice extent of 3.8% decade^{-1}. However, the declining trend amounts to 13.1% decade^{-1} for the sea ice minimum month of September (over 1978-2013, Vaughan et al. (2013), Fig.1.1). This demonstrates that the reduction of multiyear ice (the only part of the ice pack that is present during summer) accounts for a disproportionally large contribution to Arctic sea ice loss. In particular, multiyear sea ice extent decreased by $\sim$40% between 1980 and 2012 (i.e. from 6.2M km^2 to 2.5M km^2, Vaughan et al. (2013)). Apart from sea ice extent, similar declining trends are observed in ice thickness (indirectly indicating the demise of older, thicker multiyear ice) and volume (Haas et al. 2008; Rothrock et al. 2008), which may have important consequences for ocean dynamics.

The impacts of sea ice reduction are observed in all domains of the Arctic climate and ecosystem (see extensive review by Bhatt et al. (2014)).

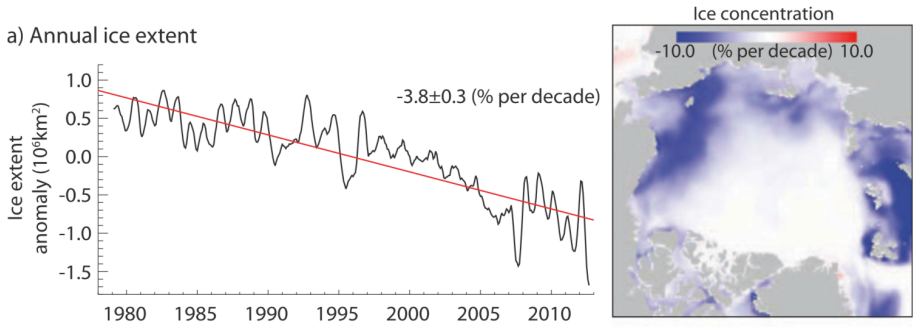

Figure 1.1: Anomalies in Arctic sea ice extent from satellite passive microwave observations, from Vaughan et al. (2013).

A direct consequence of reduced sea ice are higher temperatures in the lower atmosphere, mostly due to the well-known ice-albedo feedback mechanism during summer (e.g. Manabe and Stouffer 1980; Screen and Simmonds 2010). Extended areas and periods of open ocean also increase the moisture transport from the ocean to the atmosphere, which leads to enhanced cloud cover and may also contribute to an Arctic warming feedback loop, especially during winter (e.g. Francis et al. 2009). Direct terrestrial consequences of a warmer Arctic Ocean atmosphere in the absence of sea ice include the thawing of Arctic coastal permafrost (Romanovsky et al. 2007; Smith et al. 2010) and a modification of tundra vegetation (although the links between local warming and flora are complex and not yet fully understood, e.g. Bhatt et al. (2013)). On a large scale, Arctic warming is observed to cause pressure anomalies that act to decrease the meridional pressure gradients between the Arctic and mid-latitudes and thus slowing the jet stream. This is expected to lead to more meandering and more extreme and persistent mid-latitude weather systems and thus influences the climate in regions far south of the Arctic Circle (Francis and Vavrus 2012; Cassano et al. 2014; Screen and Simmonds 2013). However, the extent and causality of the link between sea ice cover and mid-latitude climate is still under debate and an area of active research (e.g. Blackport et al. 2019). With the retreat of the insulating sea ice cover, the ocean is more exposed

to atmospheric variability on all time and space scales. For instance, as part of the ice-albedo feedback, the upper ocean is warming rapidly in summer due to increased heat uptake from solar radiation, which acts to seasonally increase stratification in the surface mixed layer (SML). On the other hand, increased areas of open water and faster moving sea ice lead to a tighter coupling between the atmosphere and ocean and may increase momentum transfer and upper ocean dynamics such as mixing, which acts to weaken stratification (e.g. Polyakov et al. in prep.). These are two examples of a host of complicated interacting processes whose spatio-temporal distributions and amplitudes are subject to ongoing research (including this dissertation). From a biological perspective, a thinner/sparser sea ice cover during summer allows more light to penetrate the upper ocean, which may enhance primary production (e.g. Arrigo et al. 2008). At the same time, however, increased stratification in the SML may limit the upward flux of nutrients into the euphotic zone (e.g. McLaughlin and Carmack 2010). The spatial pattern and precise ramifications for the ecosystem are still under debate.

The drivers behind the ongoing sea-ice reduction in the Arctic can be divided into atmospheric and oceanic contributions. As this dissertation is devoted to oceanographic processes, we will only briefly outline major atmospheric drivers before considering the Arctic Ocean and its role in sea ice decline.

1.3 ATMOSPHERIC ROLE IN ARCTIC CHANGE

How do atmospheric changes in recent years contribute to sea ice loss in recent decades? Surface air temperature (SAT) has risen faster in the Arctic than in any other region of the world. Despite an intermittent cooling in the 1940s to 1960s, the long term trend exceeds 1.5°C century^{-1}, with a strong amplification reaching 0.9°C decade^{-1} over 1998-2017 (Fig. 1.2). The

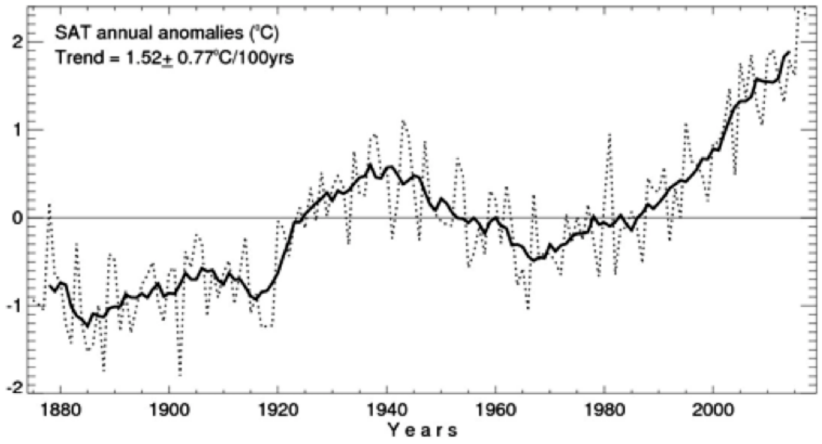

Figure 1.2: Composite time series of annual surface air temperature anomalies for the region poleward of 59°N. Dotted line shows unsmoothed values, solid line shows seven-year running mean. Adapted and expanded from Bekryaev et al. 2010).

global increase in radiative forcing due to greenhouse gas emissions has triggered a host of feedback mechanisms, such as the ice-albedo feedback, that govern Arctic SAT changes (e.g. Manabe and Stouffer 1980; Pithan and Mauritsen 2014). Due to the nature of a feedback loop, lower-level atmospheric warming is both a consequence and a driver of ongoing Arctic sea ice loss in summer. While direct heat-uptake from the ice is small due to its high albedo, solar radiation efficiently heats the upper ocean through cracks and open water, which in turn melts the ice (Perovich et al. 2017). During autumn, most of the solar heat input into the upper ocean is lost, but some of the solar heat input gained in summer may survive until winter and slow the growth of sea ice (Jackson et al. 2010). Apart from direct shortwave radiation and associated feedback loops, which are responsible for most of the observed sea ice decline, other meteorological factors are known to influence sea ice on synoptic to decadal scales. The large-scale atmospheric circulation links the sub-Arctic and mid-latitudes to the Arctic Ocean and sea ice. For instance, in recent years, atmospheric circulation changes were found to significantly contribute to wintertime atmospheric warming trends in the Atlantic sector of the Arctic (Dahlke and Maturilli

2017). Storm tracks have been observed to take a more northerly route as a consequence of climate change with Arctic cyclones increasing both in number and intensity (e.g. Zhang et al. 2004; Tamarin and Kaspi 2017). While their direct physical impacts are complicated (involving advection of heat and moisture, but also an increase of cloudiness and momentum transfer to the ice and ocean) and vary from case to case, Arctic storms are statistically connected to sea ice loss (Simmonds and Keay 2009; Kriegsmann and Brümmer 2014). Direct observations of winter storms in the central Arctic showed pulses of heat and moisture that directly reduced sea ice growth. Even though this effect is only temporary, the additional snow cover from these storms insulates the sea ice from the cold atmosphere throughout the winter season (Graham et al. 2019).

1.4 ARCTIC OCEAN'S ROLE IN CLIMATE

The oceanic contribution to Arctic sea ice loss has been studied extensively in recent years (e.g. Carmack et al. 2015; Polyakov et al. 2017; Årthun et al. 2019). The observed decline of sea ice volume over recent decades is consistent with an average ocean heat flux surplus of just 1 W m^{-2} (Kwok and Untersteiner 2011). Thus, relatively small changes in the flux of heat from the intermediate warm ocean layers to the fresh and cold waters of the surface mixed layer (SML) and sea ice might therefore contribute to the ice loss. Whether or not oceanic heat can reach the surface depends on the vertical structure (stratification) and dynamics of the water column.

1.4.1 *General Arctic Ocean hydrography and dynamics*

The Arctic Ocean can be usefully divided into two main regions: the Amerasian Basin (comprising Canada Basin and Makarov Basin) and the Eurasian Basin, roughly separated by the Lomonosov Ridge (Fig. 1.3). The

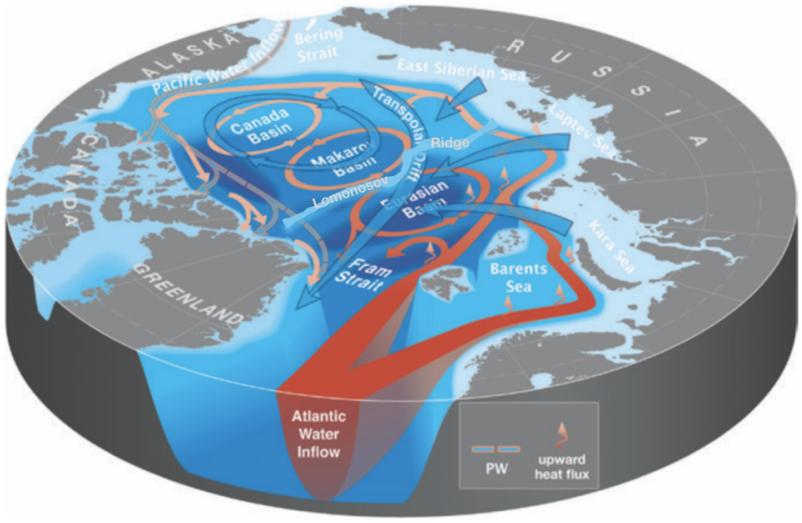

Figure 1.3: Geography and general circulation of the Arctic Ocean (adapted from Carmack et al. 2015).

hydrography of the Arctic Ocean is governed by the seasonal sea ice cover, freshwater inflow from several of the largest rivers on Earth onto the vast shelves and inflows from the Atlantic and Pacific Ocean. With temperatures close to the freezing point, salinity (or lack thereof) is the dominant factor that defines density (and thus stratification) throughout the Arctic. The Amerasian Basin (also referred to as the Pacific sector) is characterized by an inflow of ~1 Sv (1 Sv = 106 m^3/s) of Pacific water through the narrow (~80 km) and shallow (~50 m) Bering Strait (e.g. Woodgate 2018 and references therein). The Pacific water inflow represents an important (but variable) flux of heat and freshwater into the Arctic Ocean and is the result of two different water masses: winter waters with low temperatures and salinity maintaining the Amerasian Basin halocline (e.g. Aagaard et al. 1981) and summer waters, which create a temperature maximum in the upper halocline (~50-100 m) and contributes to sea ice decline in the western Arctic (Shimada et al. 2006; Woodgate et al. 2010). The internal circulation of the Amerasian Basin is governed by the Arctic High,

which leads to a generally anti-cyclonic (clockwise) circulation known as the Beaufort Gyre. Through Ekman convergence/divergence, the gyre accumulates fresh water and can be regarded as main freshwater storage in the Arctic, with its magnitude depending on the strength of the large-scale atmospheric circulation (Proshutinsky et al. 2009). The Eurasian Basin, or Atlantic sector, is governed by an inflow ($\sim$5 Sv) of warm (>2°C) and salty Atlantic Water (AW). North of Norway, the AW splits into two branches, one entering the Arctic through Fram Strait, propagating eastwards along the continantal slope within the Arctic Circumpolar Boundary Current (ACBC) while the other traverses the Barents Sea before rejoining the Fram Strait branch and the ACBC north of the Santa Anna Trough. In the Nordic Seas, the AW is present in the upper ocean, however upon entering the Arctic domain, both branches are subject to tremendous heat loss to the atmosphere around Svalbard and in the Barents Sea. With increased density, AW sinks to intermediate depth, where it resides beneath the halocline. Relative to Arctic water masses of the SML and halocline, AW is still warm (>0 °C) and eventually spreads throughout the whole Arctic Ocean. Compared to the Amerasian Basin, the Eurasian Basin is somewhat more dynamic, with stronger tidal currents (Kowalik and Proshutinsky 1994; Padman and Erofeeva 2004) and the ACBC reaching speeds of $\sim$20-30 cm/s accompanied by a train of mesoscale eddies (Pnyushkov et al. 2015; 2018). This complex system of inflows and circulation in the basins creates a unique vertical structure of water mass properties. A typical Arctic water column is characterized by a fresh and cold (at or near freezing) surface mixed layer ($\sim$20-50 m thick), overlaying the halocline, a layer defined by its strong salinity (and thus density) gradient. Beneath the halocline are the relatively warm and salty intermediate depth ($\sim$150-800 m) water masses originating from the Atlantic Ocean. The halocline with its strong density gradient acts as effective barrier between the heat from beneath and the sea ice at the surface (e.g. Rudels et al. 1996). The (seasonal) sea

ice cover and the strong upper ocean stratification also act to dampen the dynamic coupling between ocean and atmosphere. With small dynamical input from above, the amplitude of the background internal wave field, a measure of kinetic energy, is ∼2 orders of magnitude less than commonly found in the world ocean (e.g. D'Asaro and Morison 1992; Guthrie et al. 2013).

1.4.2 *Oceanic contribution to sea ice reduction*

Since the heat content of the AW layer is sufficient to melt the Arctic ice pack several times over, the ocean's contribution to recent sea ice loss depends on how efficiently the ice is insulated from the warmth beneath. Vertical heat fluxes are effectively constrained by stratification. If hydrographic changes act to reduce these density gradients or if dynamics becomes strong enough to overcome stratification and induce mixing, vertical heat fluxes are set to increase. A useful way to analyze variability of Arctic Ocean stratification is through the lens of anomalies of freshwater content. Recent years have seen a net freshening of the Arctic Ocean (e.g. Carmack et al. 2016). While the sources of this freshening are still under debate (e.g. Lique et al. 2011), the regional distribution and variability of freshwater anomalies can be linked to the general atmospheric circulation. Over the last two decades the general atmospheric pattern has been remarkably stagnant with a strong high-pressure system over the Beaufort Sea (Proshutinsky et al. 2015). This regime is causing the Beaufort Gyre to accelerate in recent years, which in turn leads to an accumulation of freshwater (and an acceleration of Pacific inflows (Woodgate 2018)) by way of Ekman convergence (e.g. Proshutinsky et al. 2015). With an increasingly thick layer of cold buoyant freshwater at the surface, stratification increases (Fig. 1.4) and the AW layer deepens. As a consequence, the sea ice of the Amerasian Basin is increasingly well insulated from deep-ocean heat un-

der current conditions. The observed substantial sea-ice loss in this region is thus directly due to the enhanced inflow of warm Pacific summer water (Shimada et al. 2006; Woodgate et al. 2010) and the ice-albedo feedback and not vertical heat fluxes from beneath the halocline. Whereas the Pacific

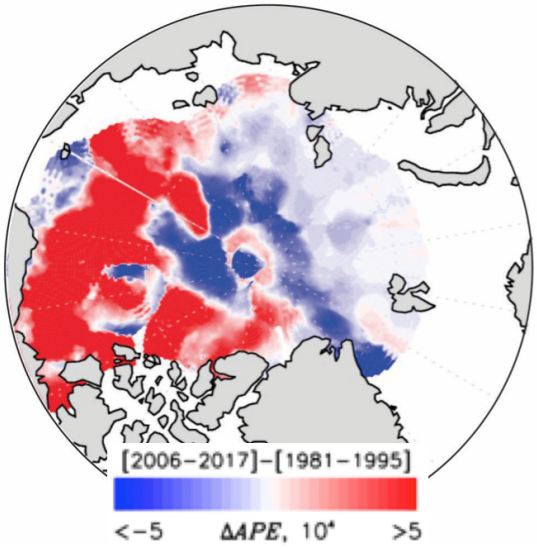

Figure 1.4: Map showing available potential energy difference ΔAPE (J m^{-2}), which can be interpreted as measure of stability of the water column) between 2006-17 and 1981-95 within the upper ocean including halocline and surface mixed layer. Adapted from Polyakov et al. 2018.

sector has seen an increase in stratification in recent years, the opposite is true for the Atlantic sector (Fig. 1.4, Polyakov et al. 2018). Polyakov et al. (2017) showed that an unprecedented erosion of halocline stratification in the eastern Eurasian Basin has led to a wintertime increase in the vertical heat flux from the AW layer to the surface with direct implications for sea ice formation. The origin of the reduced stratification in the eastern Eurasian basin may be associated with a positive trend in salinity in the Barents Sea (Polyakov et al. in prep.). Additional observations suggest a potential regional enhancement of vertical mixing (and heat fluxes) that may increase sea ice melt rates. These hydrographic and dynamic property changes in the eastern Eurasian Basin carry the signature of the upstream sub-polar North Atlantic and are thus termed the *atlantification* of the eastern Arctic Ocean. Many mechanisms and implications of these ongoing processes or tendencies are not well understood but have the

potential to substantially impact the evolution of the Arctic Ocean and its sea ice cover in the future. In this work, we analyze the hydrographic and dynamic variability of the eastern Eurasian Basin in the context of historical observations to further understand the governing mechanisms and to establish a baseline for future changes. In the following section we outline major gaps of knowledge in the changing Arctic Ocean system and in how this work is contributes to the closing of some of these gaps.

1.5 KNOWLEDGE GAPS ADDRESSED IN THIS WORK

There are several prominent timescales of variability in the Arctic, with the seasonal cycle dominating hydrographic variability and upper ocean processes. The most obvious contribution stems from the sea ice cover. In spring and summer, sea ice melt waters increase upper ocean stratification. Conversely, the brine rejected during sea ice formation in fall and winter leads to upper ocean salinification. The increased density reduces stratification and enables deep convection (down to ∼80 m depth) which is partly responsible for the creation of the halocline. However, hydrographic and dynamic seasonal variability is also found in water masses such as the AW that are not in direct contact to the atmosphere and can have substantial impact on the Arctic Ocean system. For example, the observed vertical heat fluxes through the halocline in the eastern Eurasian Basin are a quintessentially seasonal phenomenon, with heat fluxes peaking in winter (Polyakov et al. 2017). Consequently it is of critical interest to understand the full spectrum of seasonal variability in the Arctic Ocean. However, in the Arctic, spatio-temporally high-resolution ship-based observations are almost exclusively limited to the summer months, when environmental conditions facilitate expeditions. Year-round observations of the water column are only possible through moored instruments, or drifting buoys, which are expensive and thus relatively sparse. Conse-

quently, much of our understanding of seasonal processes in the Arctic Ocean relies predominantly on historical data (e.g. The Arctic Ocean Atlas, compiled by the US-Russian Environmental Working Group (1997) with data originating from wintertime airborne and ice camp surveys undertaken throughout the 50s to 90s) and model simulations. Although numerical models are continuously improving, they rely on observations for their validation and to to constrain their trajectories. For example, using model simulations to analyze the propagation of the seasonal cycle of the AW core temperature, (Lique and Steele 2012) found that the initially substantial seasonal cycle of AW temperature (>2°C) at Fram Strait rapidly decreases along its path to ∼0.1°C in the eastern Eurasian Basin. At the same location, observations showed a seasonal cycle of 0.25°C in the mid 2000s (Dmitrenko et al. 2009) that increased to ∼1°C by the mid 2010s (Polyakov et al. 2017). In addition, observations catalyze a better physical understanding of the governing processes which is needed to apprehend the ocean's variability and its susceptibility to future changes. The second chapter (*"On the seasonal cycles observed at the continental slope of the eastern Eurasian Basin of the Arctic Ocean"*) is devoted to a detailed description and analysis of the hydrographic and dynamical seasonal cycles in the eastern Eurasian Basin. We then discuss the possible drivers in the context of a changing ocean and their potential future evolution.

Time-series measurements in the Arctic Ocean show that high frequency processes in the semidiurnal (∼12-hourly) frequency band are often the dominant components of ocean and ice velocity variability (e.g. Plueddemann 1992; Kwok et al. 2003; Rainville and Woodgate 2009). These processes include tides and wind-forced inertial motion, the kinetic energy for each being highly variable in space and time. Tidal currents in the Arctic vary from negligible in the central basins to >100 cm/s over topographic features. Inertial oscillations are excited by variations in wind stress. In the Arctic, inertial motion in sea ice and the upper ocean can

be substantial (>20 cm/s) when ice concentration is less than ∼80-90%. Sparse measurements of ocean turbulence indicate that HF processes can dominate mixing rates and diapycnal fluxes (Padman and Dillon 1991; D'Asaro and Morison 1992; Ullgren et al. 2014). Recent years have seen an increase in semidiurnal current kinematics in the eastern Eurasian basin. Their increase is accompanied by a ∼5-7 fold increase in upper ocean vertical current shear since the early 2000s (Polyakov et al. in prep.). Shear is an important precursor for mixing and its increase may thus contribute to additional vertical heat fluxes and sea ice reduction. In the third chapter (*"Semidiurnal dynamics of the Arctic Ocean's eastern Eurasian Basin"*), we analyze upper ocean current observations to investigate the origin of the enhanced semidiurnal band currents and their interactions with sea ice.

Using all available moored current observations over the last two decades throughout the Arctic, we compiled a *pan-Arctic tidal current atlas*. The atlas contains detailed tidal current parameters and their variability over time and depth for over 300 records. This data set will be published separately and is intended to enable the validation of numerical ocean- and climate models with simulated 3-D tidal currents. Furthermore this atlas allows for detailed observation-based analyses of tidal currents at various locations over different time periods that may support a host of applications including physical process studies, navigation, fisheries and offshore construction.

1.6 REFERENCES

Aagaard, K., L. K. Coachman, and E. Carmack, 1981: On the halocline of the Arctic Ocean. Deep Sea Research Part A. Oceanographic Research Papers, 28, 529–545, doi:10.1016 0198-0149(81)90115-1.

Årthun, M., T. Eldevik, M. Årthun, T. Eldevik, and L. H. Smedsrud, 2019: The Role of Atlantic Heat Transport in Future Arctic Winter Sea Ice Loss. J. Climate, 32, 3327–3341, doi:10.1175 JCLI-D-18-0750.1.

Bekryaev, R. V., I. V. Polyakov, V. A. Alexeev, R. V. Bekryaev, and V. A. Alexeev, 2010: Role of Polar Amplification in Long-Term Surface Air Temperature Variations and Modern Arctic Warming. Journal of Climate, 23, 3888–3906, doi:10.1175 2010JCLI3297.1.

Bhatt, U. S., and Coauthors, 2013: Recent Declines in Warming and Vegetation Greening Trends over Pan-Arctic Tundra. Remote Sensing 2013, Vol. 5, Pages 4229-4254, 5, 4229–4254, doi:10.3390 rs5094229.

Bhatt, U. S., and Coauthors, 2014: Implications of Arctic Sea Ice Decline for the Earth System. http: dx.doi.org 10.1146 annurev-environ-122012-094357, 39, 57–89, doi:10.1146 annurev-environ-122012-094357.

Blackport, R., J. A. Screen, K. van der Wiel, and R. Bintanja, 2019: Minimal influence of reduced Arctic sea ice on coincident cold winters in mid-latitudes. Nat. Clim. Chang, 9, 697–704, doi:10.1038 s41558-019-0551-4.

Carmack, E. C., and Coauthors, 2016: Freshwater and its role in the Arctic Marine System: Sources, disposition, storage, export, and physical and biogeochemical consequences in the Arctic and global oceans. Journal of Geophysical Research: Biogeosciences, 121, 675–717, doi:10.1002 2015JG003140.

Carmack, E., and Coauthors, 2015: Toward Quantifying the Increasing Role of Oceanic Heat in Sea Ice Loss in the New Arctic. Bull. Amer. Meteor. Soc, 96, 2079–2105, doi:10.1175 BAMS-D-13-00177.1.

Cassano, E. N., J. J. Cassano, M. E. Higgins, and M. C. Serreze, 2014: Atmospheric impacts of an Arctic sea ice minimum as seen in the Community Atmosphere Model. International Journal of Climatology, 34, 766–779, doi:10.1002 joc.3723.

D'Asaro, E. A., and J. H. Morison, 1992: Internal waves and mixing in the Arctic Ocean. Deep Sea Research Part A. Oceanographic Research Papers, 39, S459–S484, doi:10.1016 S0198-0149(06)80016-6.

Dahlke, S., and M. Maturilli, 2017: Contribution of Atmospheric Advection to the Amplified Winter Warming in the Arctic North Atlantic Region. Advances in Meteorology, 2017, 1–8, doi:10.1155 2017 4928620.

Dmitrenko, I. A., and Coauthors, 2009: Seasonal modification of the Arctic Ocean intermediate water layer off the eastern Laptev Sea continental shelf break. J. Geophys. Res, 114, 11, doi:10.1029 2008JC005229.

Environmental Working Group, 1997: *Joint U.S.-Russian Atlas of the Arctic Ocean, Version 1*. L. Timokhov and F. Tanis, Eds.

Fer, I., A. K. Peterson, and J. E. Ullgren, 2014: Microstructure Measurements from an Underwater Glider in the Turbulent Faroe Bank Channel Overflow. http: dx.doi.org 10.1175 JTECH-D-13-00221.1, doi:10.1175 JTECH-D-13-00221.1.

Flato, G. M., and R. D. Brown, 1996: Variability and climate sensitivity of landfast Arctic sea ice. J. Geophys. Res. Oceans, 101, 25767–25777, doi:10.1029 96JC02431.

Francis, J. A., D. M. White, J. J. Cassano, W. J. Gutowski, L. D. Hinzman, M. M. Holland, M. A. Steele, and C. J. Vörösmarty, 2009: An arctic hydrologic system in transition: Feedbacks and impacts on terrestrial, marine, and human life. J. Geophys. Res. Oceans, 114, 890, doi:10.10292008JG000902.

Francis, J. A., and S. J. Vavrus, 2012: Evidence linking Arctic amplification to extreme weather in mid-latitudes. Geophys. Res. Lett, 39, doi:10.1029 2012GL051000.

Graham, R. M., and Coauthors, 2019: Winter storms accelerate the demise of sea ice in the Atlantic sector of the Arctic Ocean. Scientific Reports, 9, 9222.

Guthrie, J. D., J. H. Morison, and I. Fer, 2013: Revisiting internal waves and mixing in the Arctic Ocean. J. Geophys. Res. Oceans, 118, 3966–3977, doi:10.1002 jgrc.20294.

Haas, C., A. Pfaffling, S. Hendricks, L. Rabenstein, J. L. Etienne, and I. Rigor, 2008: Reduced ice thickness in Arctic Transpolar Drift favors rapid ice retreat. Geophys. Res. Lett, 35, 22697, doi:10.1029 2008GL034457.

Jackson, J. M., E. C. Carmack, F. A. McLaughlin, S. E. Allen, and R. G. Ingram, 2010: Identification, characterization, and change of the near-surface temperature maximum in the Canada Basin, 1993–2008. J. Geophys. Res. Oceans, 115, 146, doi:10.1029 2009JC005265.

Kowalik, Z., and A. Y. Proshutinsky, 1994: The Arctic Ocean Tides. American Geophysical Union (AGU), Washington, D. C, 22 pp.

Kriegsmann, A., and B. Brümmer, 2014: Cyclone impact on sea ice in the central Arctic Ocean: a statistical study. The Cryosphere, 8, 303–317, doi:10.5194 tc-8-303-2014.

Kwok, R., and N. Untersteiner, 2011: The Thinning of Arctic Ice. AIP Conference Proceedings, 1401, 220–231, doi:10.1063 1.3653854.

Kwok, R., G. F. Cunningham, and W. D. Hibler, 2003: Sub-daily sea ice motion and deformation from RADARSAT observations. Geophys. Res. Lett, 30, n a–n a, doi:10.1029 2003GL018723.

Lique, C., and M. Steele, 2012: Where can we find a seasonal cycle of the Atlantic water temperature within the Arctic Basin? J. Geophys. Res. Oceans, 117, n a–n a, doi:10.1029 2011JC007612.

Lique, C., G. Garric, A.-M. Treguier, B. Barnier, N. Ferry, C.-E. Testut, and F. Girard-Ardhuin, 2011: Evolution of the Arctic Ocean Salinity, 2007–08: Contrast between the Canadian and the Eurasian Basins. J. Climate, 24, 1705–1717, doi:10.1175 2010JCLI3762.1.

Manabe, S., and R. J. Stouffer, 1980: Sensitivity of a global climate model to an increase of CO2 concentration in the atmosphere. J. Geophys. Res. Oceans, 85, 5529–5554, doi:10.1029 JC085iC10p05529.

Maykut, G. A., and N. Untersteiner, 1971: Some results from a time-dependent thermodynamic model of sea ice. J. Geophys. Res. Oceans, 76, 1550–1575, doi:10.1029 JC076i006p01550.

Padman, L., and S. Erofeeva, 2004: A barotropic inverse tidal model for the Arctic Ocean. Geophys. Res. Lett, 31, 53–54, doi:10.1029 2003GL019003.

Padman, L., and T. M. Dillon, 1991: Turbulent mixing near the Yermak Plateau during the Coordinated Eastern Arctic Experiment. J. Geophys. Res. Oceans, 96, 4769–4782, doi:10.1029 90JC02260.

Perovich, D. K., and Coauthors, 2017: Arctic sea-ice melt in 2008 and the role of solar heating. Annals of Glaciology, 52, 355–359, doi:10.3189 172756411795931714.

Pithan, F., and T. Mauritsen, 2014: Arctic amplification dominated by temperature feedbacks in contemporary climate models. Nature Geoscience 2015 8:3, 7, 181–184, doi:10.1038 ngeo2071.

Plueddemann, A. J., 1992: Internal wave observations from the Arctic environmental drifting buoy. J. Geophys. Res. Oceans, 97, 12619–12638, doi:10.1029 92JC01098.

Pnyushkov, A. V., I. V. Polyakov, V. V. Ivanov, Y. Aksenov, A. C. Coward, M. Janout, and B. Rabe, 2015: Structure and variability of the boundary current in the Eurasian Basin of the Arctic Ocean. Deep Sea Research Part I: Oceanographic Research Papers, 101, 80–97, doi:10.1016 j.dsr.2015.03.001.

Pnyushkov, A., I. V. Polyakov, L. Padman, and A. T. Nguyen, 2018: Structure and dynamics of mesoscale eddies over the Laptev Sea continental slope in the Arctic Ocean. Ocean Sci, 14, 1329–1347, doi:10.5194 os-14-1329-2018.

Polyakov, I. V., and Coauthors, 2017: Greater role for Atlantic inflows on sea-ice loss in the Eurasian Basin of the Arctic Ocean. Science, doi:10.1126 science.aai8204.

Polyakov, I.V.and Coauthors, in preparation: Transition to a new ocean dynamic regime in the eastern Arctic Ocean. Geophysical Research letters.

Proshutinsky, A., and Coauthors, 2009: Beaufort Gyre freshwater reservoir: State and variability from observations. J. Geophys. Res. Oceans, 114, 14485, doi:10.1029 2008JC005104.

Proshutinsky, A., D. Dukhovskoy, M.-L. Timmermans, R. Krishfield, and J. L. Bamber, 2015: Arctic circulation regimes. Philosophical Transactions of the Royal Society A: Mathematical, Physical and Engineering Sciences, 373, 20140160, doi:10.1098 rsta.2014.0160.

Rainville, L., and R. A. Woodgate, 2009: Observations of internal wave generation in the seasonally ice-free Arctic. Geophys. Res. Lett, 36, 1487–5, doi:10.1029 2009GL041291.

Romanovsky, V. E., T. S. Sazonova, V. T. Balobaev, N. I. Shender, and D. O. Sergueev, 2007: Past and recent changes in air and permafrost temperatures in eastern Siberia. Global and Planetary Change, 56, 399–413, doi:10.1016 j.gloplacha.2006.07.022.

Rothrock, D. A., D. B. Percival, and M. Wensnahan, 2008: The decline in arctic sea-ice thickness: Separating the spatial, annual, and interannual variability in a quarter century of submarine data. J. Geophys. Res. Oceans, 113, 259, doi:10.1029 2007JC004252.

Rudels, B., L. G. Anderson, and E. P. Jones, 1996: Formation and evolution of the surface mixed layer and halocline of the Arctic Ocean. J. Geophys. Res. Oceans, 101, 8807–8821, doi:10.1029 96JC00143.

Screen, J. A., and I. Simmonds, 2010: The central role of diminishing sea ice in recent Arctic temperature amplification. Nature, 464, 1334–1337, doi:10.1038 nature09051.

Screen, J. A., and I. Simmonds, 2013: Caution needed when linking weather extremes to amplified planetary waves. PNAS, 110, E2327–E2327, doi:10.1073 pnas.1304867110.

Serreze, M. C., A. P. Barrett, A. G. Slater, M. Steele, J. Zhang, and K. E. Trenberth, 2007: The large-scale energy budget of the Arctic. J. Geophys. Res. Oceans, 112, D18107, doi:10.1029 2006JD008230.

Serreze, M. C., and R. G. Barry, 2011: Processes and impacts of Arctic amplification: A research synthesis. Global and Planetary Change, 77, 85–96.

Shimada, K., T. Kamoshida, M. Itoh, S. Nishino, E. Carmack, F. McLaughlin, S. Zimmermann, and A. Proshutinsky, 2006: Pacific Ocean inflow: Influence on catastrophic reduction of sea ice cover in the Arctic Ocean. Geophys. Res. Lett, 33, 3735, doi:10.1029 2005GL025624.

Simmonds, I., and K. Keay, 2009: Extraordinary September Arctic sea ice reductions and their relationships with storm behavior over 1979-2008. Geophys. Res. Lett, 36, 4045, doi:10.1029 2009GL039810.

Smith, S. L., A. G. Lewkowicz, C. R. Burn, M. Allard, and J. Throop, 2010: The thermal state of permafrost in Canada-Results from the International Polar Year. Geo2010, proceedings of the 63rd Annual Canadian Geotechnical Conference and the 6th Canadian Permafrost Conference, 12–16.

Stroeve, J. C., V. Kattsov, A. Barrett, M. Serreze, T. Pavlova, M. Holland, and W. N. Meier, 2012: Trends in Arctic sea ice extent from CMIP5, CMIP3 and observations. Geophys. Res. Lett, 39, n a–n a, doi:10.1029 2012GL052676.

Tamarin, T., and Y. Kaspi, 2017: Mechanisms Controlling the Downstream Poleward Deflection of Midlatitude Storm Tracks. Journal of the Atmospheric Sciences, 74, 553–572, doi:10.1175 JAS-D-16-0122.1.

Vaughan, D. G., and Coauthors, 2013: Observations: cryosphere. Climate change, 2103, 317–382, doi:10.2307 26216874.

Walsh, J. E., F. Fetterer, J. S. Stewart, and W. L. Chapman, 2017: A database for depicting Arctic sea ice variations back to 1850. Geographical Review, 107, 89–107, doi:10.1111 j.1931-0846.2016.12195.x.

Woodgate, R. A., 2018: Increases in the Pacific inflow to the Arctic from 1990 to 2015, and insights into seasonal trends and driving mechanisms from year-round Bering Strait mooring data. Progress in Oceanography, 160, 124–154, doi:10.1016 j.pocean.2017.12.007.

Woodgate, R. A., T. Weingartner, and R. Lindsay, 2010: The 2007 Bering Strait oceanic heat flux and anomalous Arctic sea-ice retreat. Geophys. Res. Lett, 37, n a–n a, doi:10.1029 2009GL041621.

Zhang, X., and Coauthors, 2004: Climatology and Interannual Variability of Arctic Cyclone Activity: 1948–2002. http: dx.doi.org 10.1175 1520-0442(2004)017<2300:CAIVOA>2.0.CO;2, 17, 2300–2317

2

ON THE SEASONAL CYCLES OBSERVED AT THE CONTINENTAL SLOPE OF THE EASTERN EURASIAN BASIN OF THE ARCTIC OCEAN

Till M. Baumann[1], Igor V. Polyakov[1], Andrey V. Pnyushkov[2], Robert Rember[2], Vladimir V. Ivanov[3], Matthew B. Alkire[4], Ilona Goszczko[5], Eddy C. Carmack[6]

1 *International Arctic Research Center and College of Natural Science and Mathematics, University of Alaska Fairbanks, 930 Koyukuk Drive, Fairbanks, AK, 99775, USA*

2 *International Arctic Research Center, University of Alaska Fairbanks, 930 Koyukuk Drive, Fairbanks, AK, 99775, USA*

3 *Moscow State university, Leninskiye gory, 1, 118991, Moscow, Russia, Hydrometeorological Center of Russia, 11-13, B, Predtechensky per., Moscow, 123242, Russia and Arctic and Antarctic Research Institute, 38 Bering Street, St. Petersburg, 199397, Russia*

4 *Polar Science Center, Applied Physics Lab, University of Washington, 1013 NE 40th Street, Seattle, WA 98105, USA*

5 *Institute of Oceanology, Polish Academy of Sciences, Powstancow Warszawy 55, 81-712 Sopot, Poland*

6 *Institute of Ocean Sciences, Fisheries and Oceans Canada, 9860 West Saanich Road, Sidney, BC, V8L 4B2, Canada*

Citation: Baumann, T.M., Polyakov, I.V., Pnyushkov, A.V., Rember, R., Ivanov, V.V., Alkire, M.B., Goszczko, I. and Carmack, E.C., 2018. On the Seasonal Cycles Observed at the Continental Slope of the Eastern Eurasian Basin of the Arctic Ocean. Journal of Physical Oceanography, 48(7), pp.1451-1470.

Abstract

The Eurasian Basin (EB) of the Arctic Ocean is subject to substantial seasonality. We here use data collected between 2013 and 2015 from six moorings across the continental slope in the eastern EB and identify three domains, each with its own unique seasonal cycle: 1) The *upper ocean* (<100 m) with seasonal temperature and salinity differences of $\Delta\ \theta$=0.16 °C and ΔS=0.17, chiefly driven by the seasonal sea ice cycle. 2) The *upper slope domain* is characterized by the influence of a hydrographic front that spans the water column around the ∼750 m isobath. The domain features a strong temperature and moderate salinity seasonality ($\Delta\ \theta$=1.4 °C, ΔS=0.06) which is traceable down to ∼600 m depth. Probable cause of this signal is a combination of along-slope advection of signals by the Arctic Circumpolar Boundary Current, local wind-driven upwelling and a cross-slope shift of the front. 3) The *lower slope domain,* located offshore of the front, with seasonality in temperature and salinity mainly confined to the halocline ($\Delta\ \theta$=0.83 °C, ΔS=0.11, ∼100-200 m). This seasonal cycle can be explained by a vertical isopycnal displacement (ΔZ ∼36 m), arguably as a baroclinic response to sea-level changes. Available long-term oceanographic records indicate a recent amplification of the seasonal cycle within the halocline layer, possibly associated with the erosion of the halocline. This reduces the halocline's ability to isolate the ocean surface layer and sea ice from the underlying Atlantic Water heat with direct implications for the evolution of Arctic sea ice cover and climate.

2.1 HYDROGRAPHY OF THE EASTERN EURASIAN BASIN REGION

2.1.1 *General overview*

The eastern Eurasian Basin (EB) of the Arctic Ocean comprises the Nansen and Amundsen Basin east of Severnaya Zemlya (∼95 °E) (Fig. 2.1). The

focal area of this study is the continental slope descending from the shallow Laptev Sea shelf to the abyssal plain at approximately 125 °E. We will refer to this as the eastern EB continental slope. The water column in the eastern EB is characterized by a ∼20-50 m thick surface mixed layer (SML) overlaying the halocline which is divided into the cold halocline layer (CHL, ∼50-100 m), distinguished by homogeneous near-freezing temperatures and the lower halocline waters (LHW, ∼100-200 m) with increasing temperature and salinity with depth (e.g. Rudels et al. 1991). The relatively warm (>0 °C) Atlantic Water (AW) resides at intermediate depths below the halocline (∼200-1000 m) (**Fig. 2)**. Strong vertical salinity (and thus density) gradients in the halocline shield the SML and sea ice from the AW heat (e.g. Aagaard et al. 1981, Rudels et al. 1996). However, this insulating property may be compromised locally by storms and ocean dynamics (Polyakov et al. 2013). In recent years, a weakening of the halocline in the eastern EB has led to enhanced vertical heat fluxes through the halocline layer with direct effects on sea ice formation (Polyakov et al. 2017).

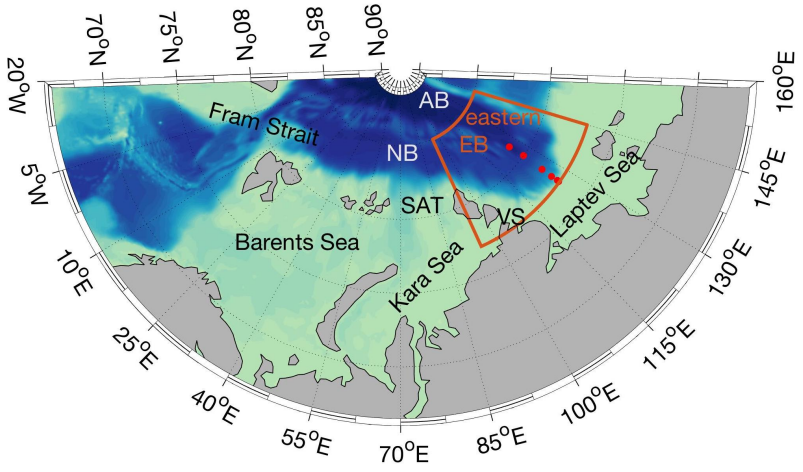

Figure 2.1: Topographic map of the Atlantic side of the Arctic Ocean with the eastern Eurasian Basin (EB) outlined in orange. Red dots indicate positions of the moorings used in this study, AB: Amundsen Basin, NB: Nansen Basin, SAT: St. Anna Trough, VS: Vilkitsky Strait.

The hydrography in the eastern EB continental slope region is strongly affected by the Arctic Circumpolar Boundary Current (ACBC). AW enters the Arctic Ocean through Fram Strait and the Barents Sea and is carried by the ACBC cyclonically along the continental margins and ridges of the Arctic Ocean (Timofeev 1960, Coachman and Barnes 1963, Aagaard 1989, Rudels et al. 1994). The 2013-2015 total transport within the ACBC amounts to 5.1 $\pm$0.1Sv at the Laptev Sea continental slope (Pnyushkov et al. 2017). The transport as well as the thermohaline properties of the ACBC are subject to substantial spatiotemporal fluctuations (see Pnyushkov et al. 2015 for detailed discussion).

2.1.2 *Hydrographic front along the continental slope*

The relatively warm and salty AW contrasts the abundant colder and fresher Arctic shelf water masses. Resulting horizontal property gradients form a hydrographic front that is observed along the AW pathways following the continental slope of the EB. Dmitrenko et al. (2014) reported a pronounced front at the eastern flank of the St. Anna Trough in 1996 and in 2008-2010 which extended throughout the entire water column with a horizontal density gradient between 0.0009-0.0022 kg/m^3/km. Similarly, in the Laptev Sea, Bauch et al. (2014) observed the front at the continental slope, separating shelf waters, continental slope waters and basin waters. Bauch et al. hypothesized that the front is maintained by lateral advection of water masses within the ACBC.

2.1.3 *Seasonal cycle in the eastern EB*

The seasonal cycle has long been recognized as one of the dominant modes of variability in the Arctic Ocean (e.g. Polyakov 1999). Historical data from averaged profiles taken during the 1950s – 1980s spanning the eastern

EB region show a distinct seasonal signal exhibited by a warmer and fresher SML during summer and colder and saltier SML in winter whereas water temperatures are lower in the lower halocline and upper AW layer compared to winter (**Fig. 2)**.

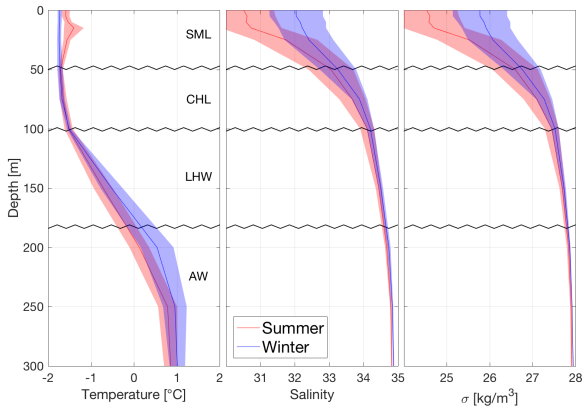

Figure 2.2: Summer and winter temperature, salinity and density (σ) profiles from the Environmental Working Group Joint U.S.-Russian Atlas of the Arctic Ocean (see section 2 for description) averaged over the eastern EB region (77-85 °N, 95-145 °E) from the 1950s – 1980s (shading is the standard deviation). Zigzag lines indicate approximate boundaries of the different layers: Surface mixed layer (SML), cold halocline (CHL), lower halocline water (LHW) and Atlantic Water (AW).

Data availability remains the major limitation for detailed analysis of seasonality in the continental slope region. The few existing long-term mooring observations generally lack the desired spatial resolution whereas summertime hydrographic sections with high spatial resolution provide only snapshots that cannot be used to document seasonality. Consequently, models have been employed to overcome these shortcomings. For example, in a study combining observations and modeling, Polyakov et al. (1999) analyzed pan-Arctic seasonality under different large-scale atmospheric circulation regimes. For the EB, they found a model-derived upper ocean (0-50 m) seasonal temperature and salinity change of 0.015 °C and 0.2, respectively, for anticyclonic regimes and changes of 0.09 °C and 0.55 for cyclonic regimes. In another effort, using model simulations supported

by moored observations, Lique et al. (2012) analyzed the propagation of the seasonal cycle of the AW core temperature, defined as the highest temperature in the profile above the 1500 m isobath, along the continental slope from Fram Strait through the eastern EB. They found that the substantial (>2 °C) seasonal cycle of AW temperature observed in Fram Strait is advected by the ACBC. By the time the signal reaches the eastern EB, its amplitude decreased to ∼0.1 °C. This value was derived under the assumption that the AW closely follows the 1500 m isobath. However, Pnyushkov et al. (2015) found, that in the eastern EB, the AW temperature core was located substantially further offshore, around the 3000 m isobath, and that at times it split into two separate cores located over the 3000 m and 3500 m isobaths. Long-term observations within the halocline (∼150 m) collected using moorings deployed at the 2700 m isobath on the eastern EB slope suggest that local seasonal temperature changes increased from 0.25 °C in 2004-2007 (Dmitrenko et al. 2009) to ∼1 °C in 2013-2015 (Polyakov et al. 2017, their figure 2c).

Here, we use a two-year long data set spanning the water column down to ∼700 m at six locations across the EB continental slope (section 2, Fig. 2.3) to identify hydrographic seasonal cycles in this region (section 3) and discuss likely drivers (section 4).

2.1.4 *Data and methods*

The central data set used in this study consists of moored observations obtained within the Nansen and Amundsen Basin Observational System (NABOS) Project. An array of six moorings ($M1_1$-$M1_6$) spanning along the 125 °E meridian from just offshore of the Laptev Sea shelf (∼77 °N, 250 m water depth) to the abyssal plain (∼81 °N, 3900 m depth) was deployed for two years from September 2013 to September 2015 (Fig. 2.3). All moorings were designed to carry out CTD (conductivity, temperature and depth),

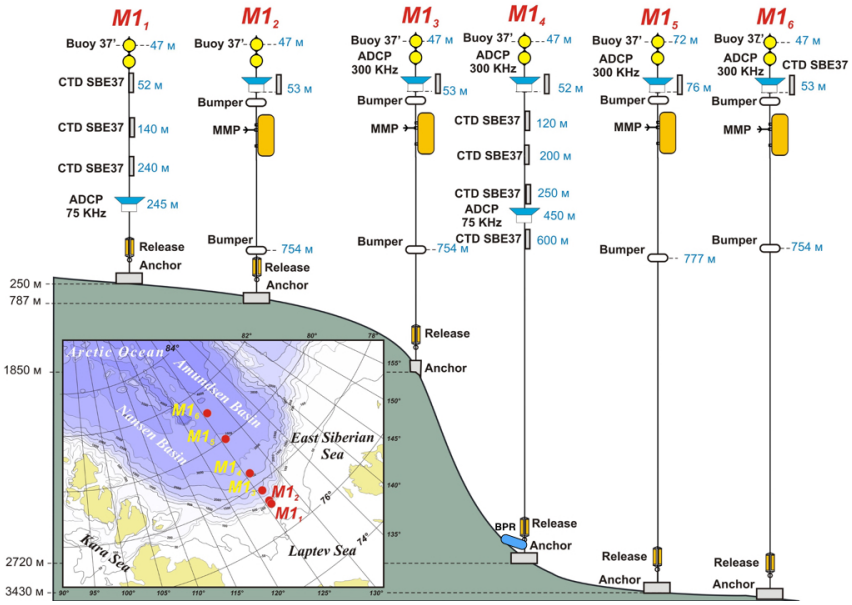

Figure 2.3: Schematics (not to scale) and locations (insert) of six moorings deployed in the eastern EB along the 125 °E in 2013-2015 (adapted from Pnyushkov et al. 2017).

as well as velocity measurements. For the $M1_1$ and $M1_4$ moorings, CTD observations were collected at up to six discrete depths using SeaBird SBE 37 MicroCATs. All other moorings were equipped with McLane moored profilers (MMP) that provided CTD and velocity profiles every other day between 50 m and 750 m depth (vertical resolution of ∼25 cm). The MMPs were equipped with high-resolution (<0.01 cm/s, error: ∼1 % ±0.5 cm/s) FSI (Falmouth Scientific Inc.) acoustic current meters and SBE 52-MP CTD sensors (expected accuracies: 0.0003 S/m, 0.002 °C and 0.1 % of full pressure range). All sensors were calibrated by the manufacturer before deployment in 2013. Upon recovery, the raw MMP data were processed using WHOI (Woods Hole Oceanographic Institution) software, which involved averaging the raw data over 2-dbar pressure bins. The MicroCATs were either sent back to the manufacturer for calibration or, if scheduled for immediate redeployment, were directly calibrated against the ship-

based SBE 911plus sensor with expected accuracies of 0.0003 S/m and 0.005 °C for conductivity and temperature.

Current velocities for the upper ∼250 m at moorings $M1_1$ and $M1_4$ were obtained by 75kHz ADCPs (acoustic Doppler current profiler) whereas all other moorings were equipped with 300kHz ADCPs to measure velocities in the upper ∼50 m (above the MMP range, see Fig. 2.3). Expected accuracies for velocities and directions are ±0.5 cm/s and ±2 ° with a vertical resolution of 2 m and 5 m for the 300kHz and 75kHz ADCPs, respectively. Unfortunately, the common problem of acoustic surface reflection rendered the upper ∼10 m (300kHz) and 25 m (75kHz) ADCP observations unusable. In addition, the ADCP at $M1_5$ stopped working after about one year. All data were linearly interpolated (MMP) or averaged (MicroCAT, ADCP) to daily values prior to analysis. The data are available online at https://arcticdata.io/catalog/ #view/arctic-data.7792.4 or http://research.iarc.uaf.edu/NABOS2/data/registered/main.php.

The Arctic Ocean Atlas, compiled by the US-Russian Environmental Working Group (1997) provides gridded hydrographic data from the Arctic Ocean over decadal periods spanning the 1950s to the 1980s. The horizontal resolution is 50 km and vertical resolution decreases from 5 m at the surface to 500 m below 1000 m depth. We use this data as historic reference state for eastern EB hydrography (77-85 °N, 95-145 °E).

Finally, daily ERA-Interim reanalysis output with a spatial resolution of 0.75 ° for both latitudes and longitudes (Dee et al. 2011) is utilized to evaluate the seasonal wind field over the eastern EB for the mooring deployment period (2013-2015).

In this study, seasonality is evaluated using two different measures.

First, seasonal cycles are defined based on calendric seasons, where *seasonal differences* are calculated by subtracting wintertime (December-January-February or DJF) averages from summertime (July-August-September or JAS) averages (note that we chose JAS as summer

months to include September, the month of minimum sea ice areal extent in our definition of Arctic summer). Secondly, wavelet analysis is employed to identify seasonal cycles. We used a standard package of wavelet programs by Torrence and Compo (1998) and calculated the wavelet transforms with the DOG Mother function. The package also provided estimates for the 95 % confidence intervals and cones of influence, indicating where the edges of the domain affect the wavelet. Time series of seasonal wavelet amplitudes with physical units (°C, cm/s, salinity) were obtained by regressing the wavelet transform at seasonal frequency (wavelet period closest to 365 days) onto the original (detrended) time series. With this measure, we define the halved differences between maxima and minima of the seasonal wavelet amplitude time series as *seasonal amplitudes*.

While seemingly redundant, both seasonal differences and wavelet-based seasonal amplitudes complement each other in that the former illustrates what is observed in a predefined seasonal frame (i.e. summer vs. winter) while the latter provides total magnitudes of variability at seasonal timescales.

2.2 SEASONAL SIGNAL OVER THE EASTERN EB CONTINENTAL SLOPE

Wavelet analysis of temperature[1] time series reveals that the seasonal cycle is the dominant mode of variability in our two-year long records. This is evident throughout the observed water column and at all mooring locations across the eastern EB continental slope.However, the position, vertical spread and phase of the strongest seasonal signals in the water column vary widely across the slope (shown for $M1_2$ and $M1_4$ in Fig. 2.4). This variety can be broken down into three patterns of seasonality

1 All mentions of "temperature" in this study are actually "potential temperature". Likewise all mentions of "density" refer to "potential density", referenced to the surface.

in three separate domains, hereafter referred to as *upper ocean, upper slope domain* (USD, moorings $M1_1$-$M1_3$) and *lower slope domain* (LSD, moorings $M1_4$-$M1_6$). In the following sections, we document the properties of the seasonal cycles in these three domains.

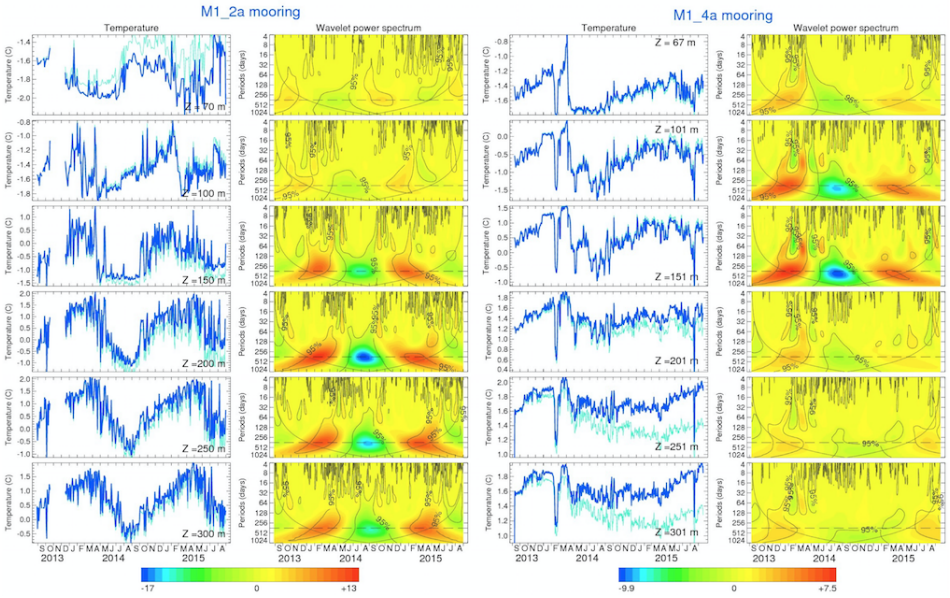

Figure 2.4: Original (light blue) and detrended (dark blue) time series and wavelet transforms of detrended time series of temperature at moorings $M1_2$ and $M1_4$. Solid black lines indicate 95 % confidence interval and the cone of influence. The horizontal dashed lines mark the seasonal (365-day) period of the wavelet transform.

2.2.1 *Seasonal signal in temperature and salinity*

SEASONAL CYCLE IN THE UPPER OCEAN

The seasonal cycle in the upper (<100 m) part of the water column, comprising the SML and CHL, is described using the offshore-most mooring $M1_6$ since it provides the observations closest to the sea surface (up to 28 m depth) among all the moorings across the section (the other moorings only reach up to 55-77 m depth). Upper ocean profiles from the gridded

Arctic Ocean Atlas at all mooring locations suggest that the surface water becomes continuously fresher and warmer (in summer) towards the shelf. While this likely influences the SML depth, we argue that the general drivers for upper ocean seasonality (sea ice cycle and atmospheric forcing) are comparable throughout the array, thus allowing to use $M1_6$ as proxy for upper ocean seasonality across the slope.

Fig. 2.5 shows the time series and their wavelets for temperature and salinity at different depths in the upper ocean at the $M1_6$ mooring position. The upper ocean variability is characterized by strong seasonality of temperature and salinity with an underlying trend. At the uppermost available depth level (28 m), the variability of the detrended salinity ranges between 31.8 and 33.2 with seasonal minima in October-November and maxima in late April-May for both years. Seasonal differences reach 0.16 °C and 0.17 for temperature and salinity, respectively. The wavelet-derived amplitudes of the seasonal signal are 0.12 °C and 0.53. The detrended seasonal temperature signal peaks at ∼-1.6 °C in mid-September, with short-lived events increasing the summer temperature up to -1.4 °C in 2014. Through winter, temperature decreases as salinity increases, and reaches minima around -1.8 °C (freezing point) in March-April for both years. The phases between the seasonal cycles of temperature and salinity are thus shifted by about one month, with salinity trailing temperature.

At 50 m, the amplitude of the seasonal signal is reduced by ∼50 % for salinity, but much less so for temperature (Fig. 2.5, middle panels). Deeper, at 76 m, the seasonal cycle of salinity is in phase with that of temperature, in contrast to their opposition in the upper ocean (Fig. 2.5, lower panels vs. upper panels), indicating the influence of an independent seasonal signal within the halocline, which will be described in section 3.1.3.

On the other hand, depth-time diagrams of temperature and salinity provide evidence for seasonal variability in the halocline (down to140 m depth) resembling that of the surface seasonality (Fig. 2.6a,b). For exam-

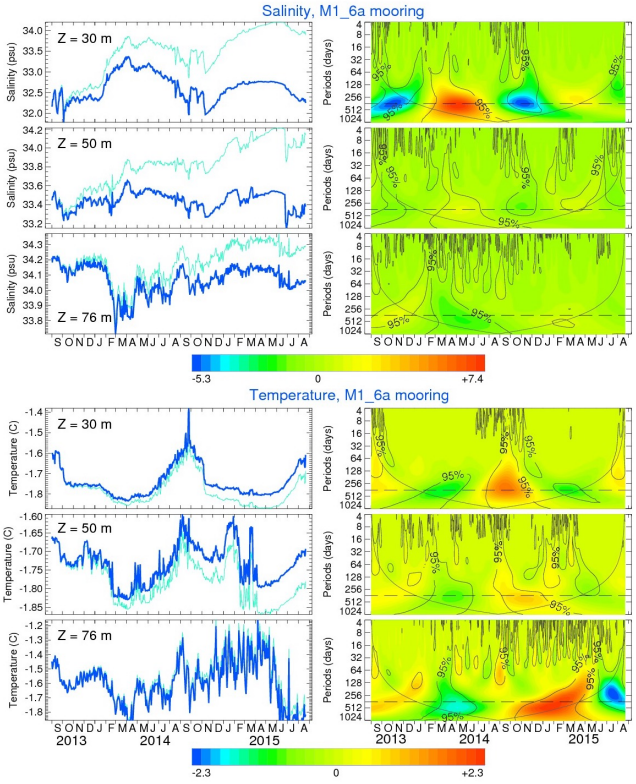

Figure 2.5: Original (light blue) and detrended (dark blue) time series (left) and wavelet transforms of detrended time series (right) of upper ocean salinity (top) and temperature (bottom) at the $M1_6$ mooring. Solid black lines indicate 95 % confidence interval and the cone of influence. The horizontal dashed lines mark the seasonal (365-day) period of the wavelet transform.

ple, ventilation of the upper ocean led to isotherm/isohaline deepening throughout the halocline.

The seasonal evolution of the SML depth at the $M1_6$ mooring location is shown in Fig. 2.6a,b (white lines). In calculating SML depth, we followed Monterey and Levitus (1997) who defined the SML thickness by the depth at which density exceeds the surface density by 0.125 kg/m^3 (in our case, the surface density was approximated by the density of the uppermost available observation). Note that while the available mooring data restricted to below 28 m allow reliable definition of the SML depth in winter, the summer estimate of 30 m is very close to the shallow limit of

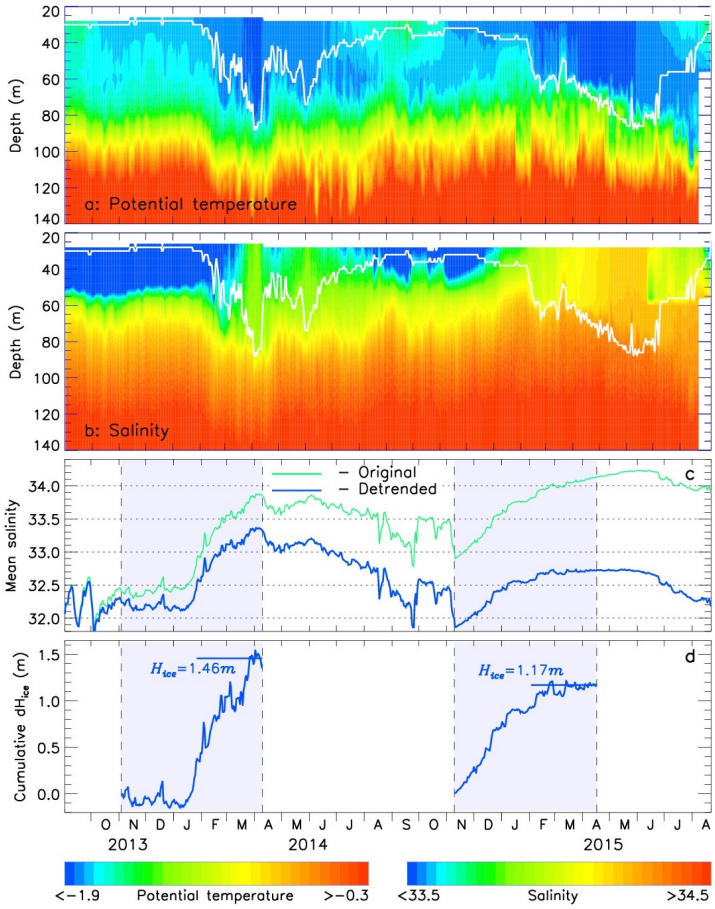

Figure 2.6: (a, b) Time series of upper water column temperature and salinity at $M1_6$, respectively. White line indicates surface mixed layer (SML) boundary. (c) Salinity averaged over SML. (d) Ice growth calculated from salinity increase during winter representing brine rejection. Shading in (c) and (d) marks the ice-growing season based on salinity increases.

observations and thus requires further justification. Summer CTD profiles carried out near $M1_6$ indicated that SML depths were 22 m SML depth in 2013 and 23 m in 2015. These values are somewhat less than our estimate of ∼30 m derived from the mooring data, but we argue that they are close enough to justify the approach. The prominent feature of the observed seasonal signal is a deepening of the SML from ∼30 m in summer to ∼80 m in winter.

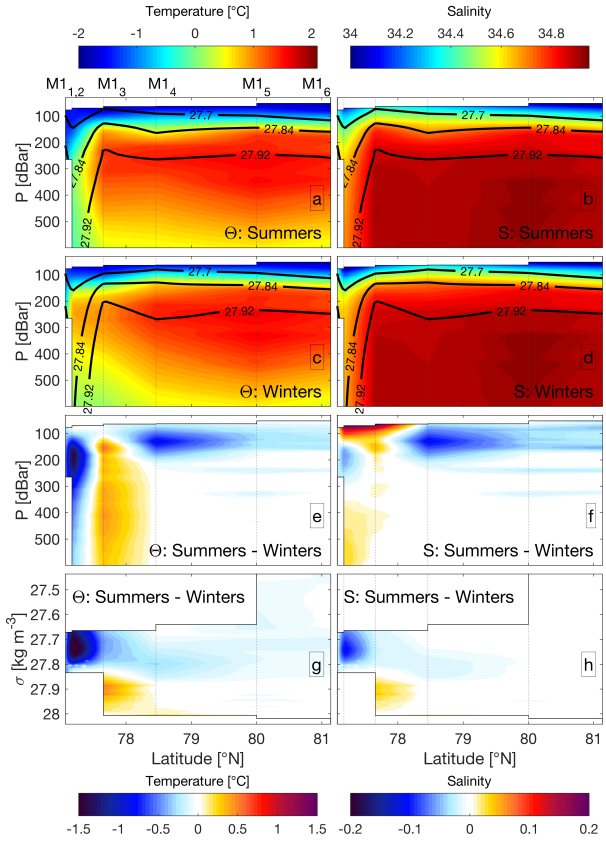

Figure 2.7: (a-d) Sections of moored observations of seasonal temperature (θ) and salinity (S). Black contours are 27.7, 27.84 and 27.92 isopycnals. Dashed lines and figure borders indicate mooring positions (as indicated above (a)). (e, f) Seasonal differences of θ and S. (g, h) Same as (e, f), but with density as vertical coordinate.

SEASONAL CYCLE IN THE UPPER SLOPE DOMAIN

The USD spanning from the $M1_1$ mooring (250 m water depth) to the $M1_3$ mooring (1850 m water depth) is rather narrow (covering 65 km of the upper slope) and all mooring records are influenced by the proximity to the hydrographic front. Because the front is apparent in-between moorings $M1_2$ and $M1_3$ (cf. sloping isopycnals in Fig. 2.7a-d), its exact location cannot be determined. However, ship based CTD sections of up to 19 casts across the slope undertaken in summers 2013 and 2015 suggest that the front lies just offshore of the $M1_2$ mooring position (750 m depth, not shown), at least in late summer. Seasonal differences in the USD show

a strong temperature signal spreading throughout the observed water column below ∼100 m. Specifically, at the $M1_1$ and $M1_2$ mooring locations, the seasonal cycle features colder summers compared to winters below 100 m as shown in cross-slope sections (Fig. 2.7a,c) and temperature-salinity (θ-S) diagrams (Fig. 2.8, upper panels). Seasonal temperature differences (summers minus winters) peak at -1.4 °C at 180 m depth (Fig. 2.7e). Wavelet-based amplitudes of the seasonal signal reach 0.8-0.9 °C between 160 and 300 m depth at $M1_2$ and decrease gradually to ∼0.4 °C at 600 m depth (Fig. 2.9, top).

Contrasting to the more onshore moorings $M1_1$ and $M1_2$, the AW at $M1_3$ shows higher summer temperatures compared to winters with seasonal differences and wavelet derived amplitudes both reaching 0.5 °C, which is smaller than the seasonal change observed at $M1_2$ (Fig. 2.7e and Fig. 2.9, top). A common feature shared by all USD moorings ($M1_1$-$M1_3$) is the vast vertical spread of temperature seasonality throughout the water column in the vicinity of the hydrographic front.

The seasonality of salinity exhibits a very different pattern compared to temperature. Below ∼100 m, in the region of the strongest temperature signal, seasonality of salinity is small, with summertime fresher water (∼150 m-250 m) above summertime saltier water (>400 m) (Fig. 2.7f). The amplitude of the salinity signal is generally lower than 0.06 (Fig. 2.9, middle). An exception is the strong salinity seasonality in the CHL (shallower than ∼100 m depth) at $M1_2$ and $M1_3$ mooring locations that reaches a maximum seasonal difference of 0.2 at the very top of the observed water column (70 m) at both moorings and rapidly decreases with increasing depth (Fig. 2.7f). θ-S diagrams reveal that the seasonal thermohaline properties of this signal are essentially collinear along the salinity axis, especially at $M1_2$ (Fig. 2.8 diamonds). This suggests that isopycnal displacement, rather than a seasonal change of water mass may be the source of this signal. The absence of this signal in isopycnal

coordinate plots further supports this notion (Fig. 2.7e,g,h). Unfortunately, because only the deepest part of the signal (> ∼70 m) is captured, a meaningful quantification of the isopycnal displacement is not feasible. However, in the following section, we will demonstrate that this signal is similar to the seasonality observed in the LSD (albeit centered in the LHW at >100 m depth and not in the CHL).

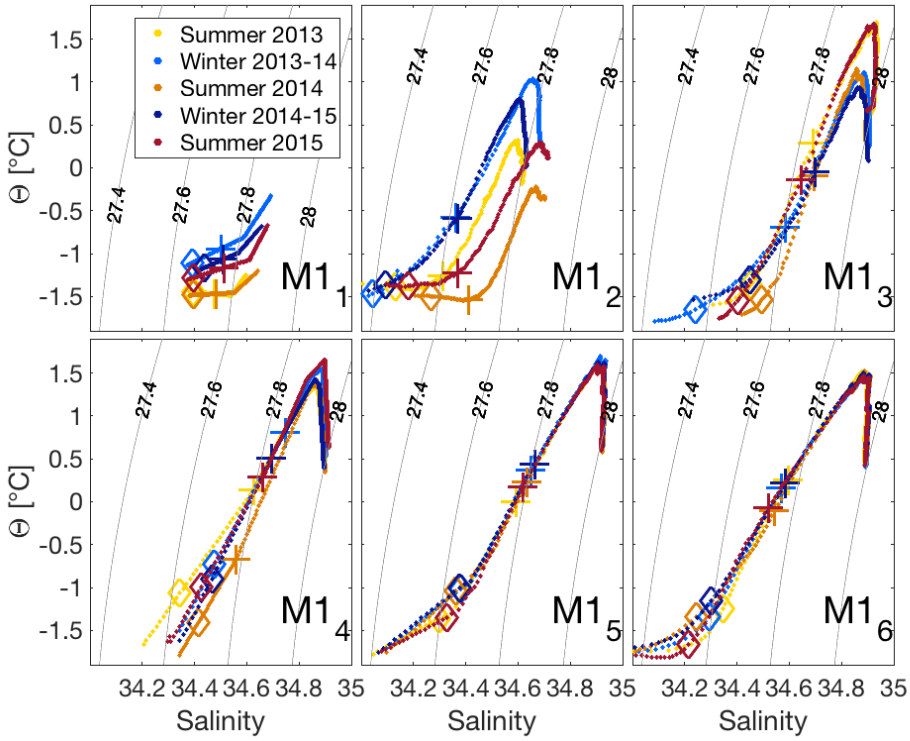

Figure 2.8: θ-S diagrams for the cross-slope mooring array in the eastern EB. Color notation for the seasonal averaging is shown in insert. Diamonds and crosses denote thermohaline properties at 85 m and 130 m depth, respectively

SEASONAL CYCLE IN THE LOWER SLOPE DOMAIN

In the LSD (moorings $M1_4$-$M1_6$), beneath the upper ocean domain, the seasonal cycle is confined to the halocline and upper AW layer (∼100-200 m) with colder and fresher summers relative to winters (Fig. 2.7e,f and Fig. 2.8). Maximum seasonal salinity and temperature differences

are -0.11 and -0.83 °C while wavelet-derived amplitudes reach maxima of 0.1 and 0.77 °C for salinity and temperature, respectively at ∼130 m depth at the $M1_4$ mooring location (Fig. 2.9, top and middle). Colder and fresher summers compared to winters are also evident in historical records from the 1950s through the 1980s (Fig. 2.2). However, while in this early period the temperature signal was found between 100 m and 300 m depth with the maximum located around 200 m, in recent years, the maximum seasonal cycle in the LSD was considerably shallower, centered around 130 m depth.

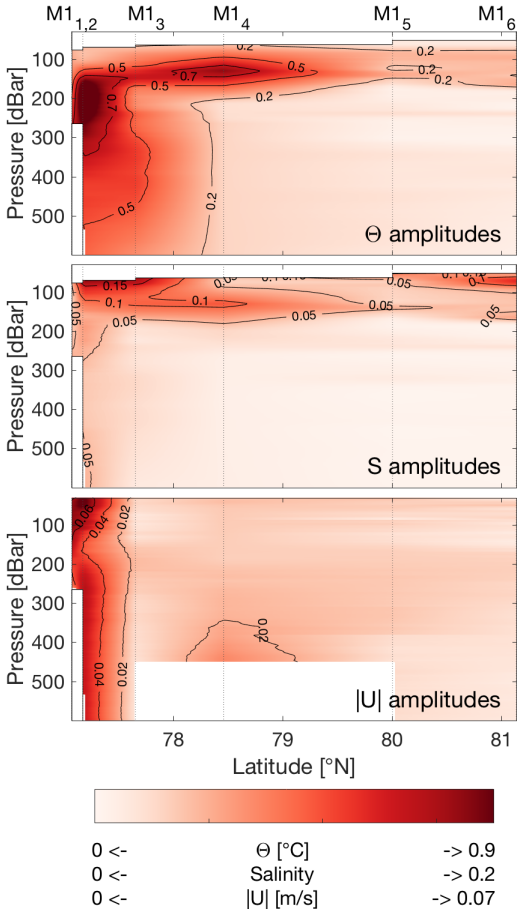

Figure 2.9: Sections of wavelet derived seasonal amplitudes for temperature, salinity and current speed.

The seasonal thermohaline properties around 130 m (marked by crosses in Fig. 2.8, lower panel) are practically collinear, thus indicating little seasonal water mass change in the halocline and upper AW. Similar to the CHL salinity signal found in the USD, the spread of the crosses suggests that the observed seasonal signal is due to a vertical displacement of isopycnals. Analysis of the LSD seasonal changes on isopycnal surfaces supports this finding: Fig. 2.7g,h shows that the temperature and salinity differences presented in a density coordinate system exhibit almost no seasonal signal in the halocline (around the σ =27.84 level). Comparison of seasonal density profiles showed a 36 m isopycnal displacement between summers (low) and winters (high) at ~130 m depth at $M1_4$ (Fig. 2.10). Note that this measure of isopycnal displacement depends on linear vertical interpolation between the available discrete measurements and should thus be regarded as point of reference only.

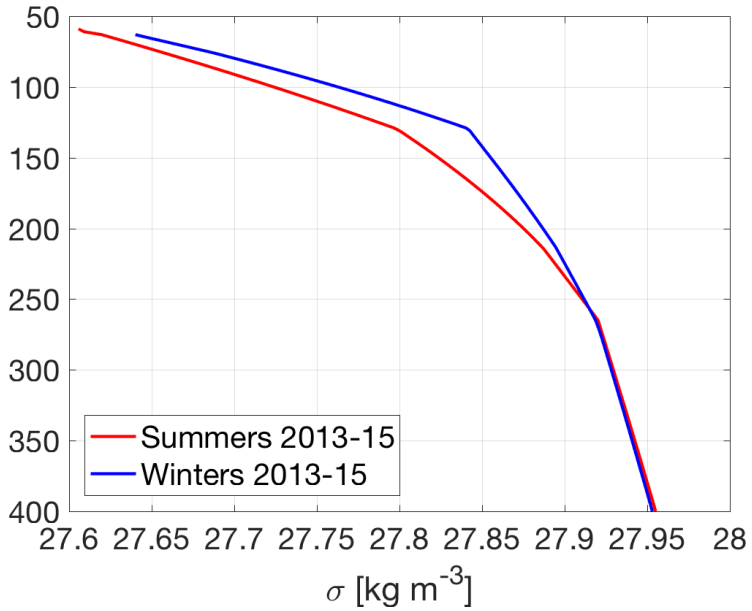

Figure 2.10: Seasonal density profiles from individual instruments at the $M1_4$ mooring site.

2.2.2 *Seasonal signal in current velocities*

Velocity measurements reach up to 10-25 m depth at most moorings. Thus, these time series of current speed records and their wavelet analysis provide an opportunity to resolve details of the seasonal signal of oceanic currents within the SML (Fig. 2.11).

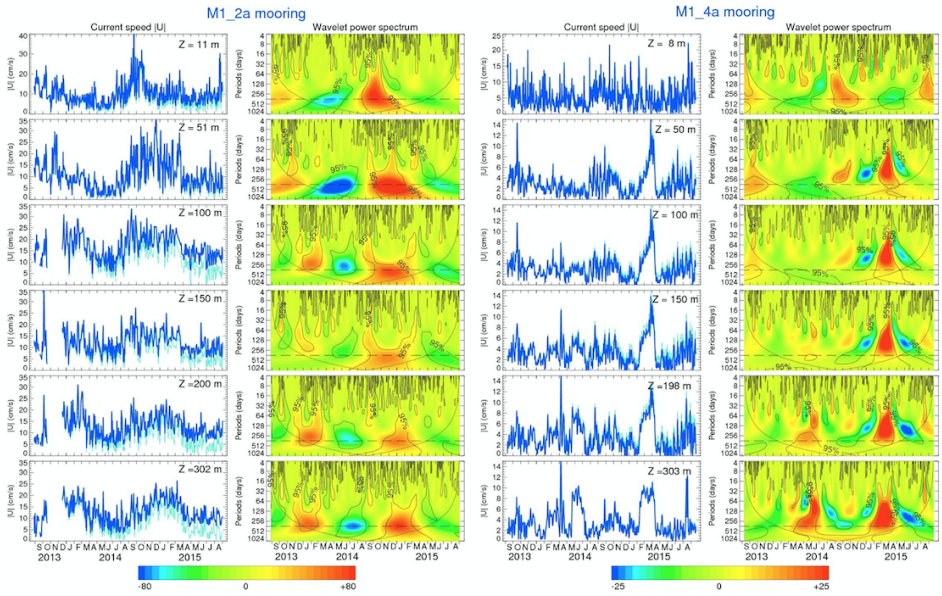

Figure 2.11: Original (light blue) and detrended (dark blue) time series (left) and wavelet transforms of detrended time series (right) of current speed at moorings $M1_2$ and $M1_4$. Solid black lines indicate 95 % confidence interval and the cone of influence. The horizontal dashed lines mark the seasonal (365-day) period of the wavelet transform.

Within the SML, both moorings $M1_2$ and $M1_4$ feature seasonality with maximum current speed in September-October and minima in April. This agrees with the storm activity pattern for the Laptev Sea area derived from land based stations that show highest storm frequency and intensity in October (Atkinson 2005). The wavelet-derived amplitudes of seasonal current speed within the SML differ greatly between the mooring locations, with 5.5 cm/s at $M1_2$ and 1.3 cm/s at $M1_4$ (**Fig. 11 and Fig. 9,** bottom). Fig. 2.12a shows seasonally averaged SML currents. It becomes apparent that

there is no consistent pattern linking current strength and season across the mooring array. While at $M1_3$ and $M1_6$ summer velocities are slightly greater, at $M1_2$ and $M1_4$ the opposite is true. The flow on the steeper part of the slope, at moorings $M1_2$ - $M1_4$ is mostly aligned with the underlying topography throughout all averaging periods, regardless of wind direction (cf. Fig. 2.13).

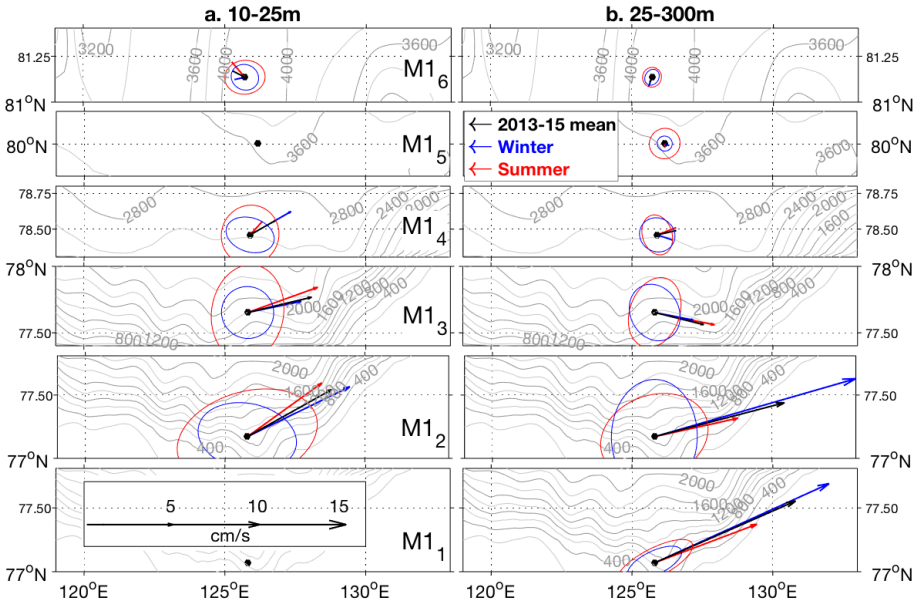

Figure 2.12: (a) Current vectors across the mooring array averaged over the observed SML (10-25 m) and over seasons as well as associated ellipses of standard deviation (all vectors and ellipses are scaled as indicated in the bottom left panel). To improve readability, each mooring is in an individual panel (note that latitudes between panels may overlap). Due to too short records or missing data, no vectors are plotted at $M1_1$ and $M1_5$ (see data description section 2). (b) Same as (a) but for the ocean below the SML (25-300 m). Gray lines indicate topography.

In the USD (in the vicinity of the hydrographic front), below the SML, the seasonal signal at the $M1_2$ mooring remains strong and evident from both visual inspection of the time series and wavelet analysis, with a notable delay of around three months between the surface and 300 m (Fig. 2.11). Wavelet-based amplitudes reach up to 7 cm/s in the upper 100 m at $M1_1$ and $M1_2$, decreasing further offshore to $\sim$1 cm/s from $M1_3$ on (Fig. 2.9, bottom). In general, the mean currents at the $M1_1$-$M1_3$ mooring

locations as well as the seasonally averaged currents are aligned with the topography (Fig. 2.12b).

In the LSD, offshore of the hydrographic front and below the SML (~25 m), variability of the time series of current speed at the $M1_4$ mooring location is dominated by sub-seasonal fluctuations on timescales from days to months that mask the seasonal cycle. For example, the pronounced signal that passed the mooring in early 2015 produced a maximum in the wavelet analysis that extends to seasonal timescales, thus modulating the seasonal signal (Fig. 2.11). Wavelet-derived seasonal amplitudes are relatively small (<2 cm/s) but consistent in magnitude throughout the LSD (Fig. 2.9). The only exception is a region of higher amplitude (>2 cm/s) below 300 m at the $M1_4$ mooring location. Seasonally averaged currents in Fig. 2.12b are also small (<1 cm/s) with no discernible structure in their rotation. This indicates little seasonal persistence of current directions, possibly due to mesoscale fluctuations such as eddies.

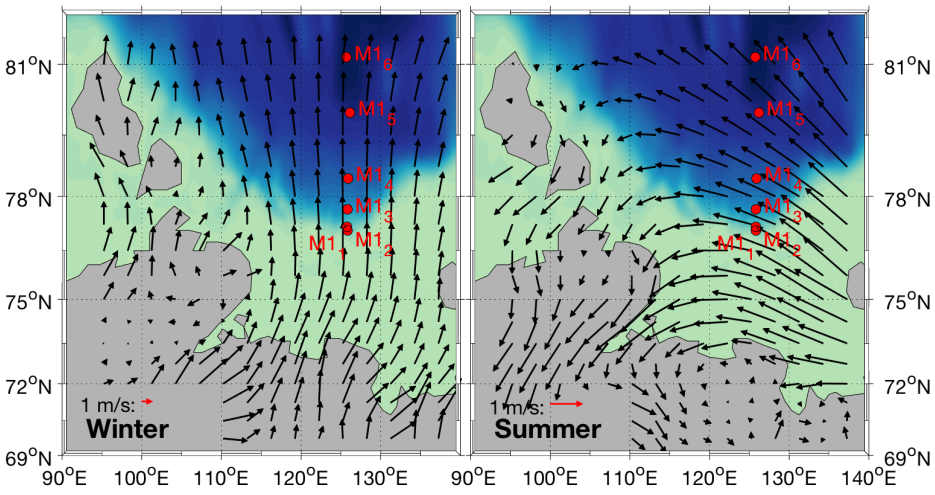

Figure 2.13: ERA-Interim reanalysis wind, averaged over winters (left) and summers (right) over the mooring deployment period 2013–2015. Note the different scaling (red arrows) between the plots.

2.3 DISCUSSION OF DRIVERS FOR THE OBSERVED SEASONAL CYCLES

2.3.1 *Upper Ocean*

LOCAL ICE MELT AND FREEZING PROCESSES

Processes associated with the annual sea ice cycle are the main driving factors behind the seasonal thermohaline cycle in the upper Arctic Ocean (e.g. Rudels et al. 1996). The fact that seasonal amplitudes for temperature and salinity at 30 m are substantially greater than at 50 m (as evidenced by wavelet analysis) supports the notion of seasonal forcing that originates at the surface (Fig. 2.5). Vertical mixing across the halocline is an important contributor to the observed SML seasonality (e.g. Fer et al. 2017, Polyakov et al. 2017). As shown in section 3.1.1, there is an approximately one-month delay of the seasonal salinity signal relative to that of temperature. After the SML temperature reaches its maximum in mid-September, its stored heat must be removed by surface cooling before freeze-up and related brine rejection can start; hence the offset. In winter, the SML temperature remains close to the freezing point, a function of salinity, therefore the winter maximum of salinity and minimum of temperature are in phase.

The seasonal increase of SML salinity in winter together with temperature decrease and deepening of the SML can be attributed to free convection driven by brine rejection during freeze-up (Fig. 2.6b,c). From the salinity change in the SML, a quantitative estimate of local ice formation can be derived assuming an average sea ice salinity of 3, balanced with the observed average SML salinity. While the assumed salinity is on the lower side of the typical range for first-year Arctic sea ice salinity of 2-6 (Barry et al. 1993), changing the values of prescribed sea ice salinity has only minor effect on ice thickness ($\sim$3 % thickness change per unit sea ice salinity). The estimates yield a sea ice thickness of $\sim$1.5 m in the first

and ∼1.2 m in the second winter (Fig. 2.6d). Ice thickness measurements carried out by an upward looking sonar at the $M1_4$ mooring location yield a maximum monthly modal sea ice thickness of 1.44 m and 1.42 m for 2014 and 2015, respectively, which is reasonably close to our estimates. Using satellite data acquired since 1982, Maslanik et al. (2007) showed that the eastern EB is covered almost exclusively with first year ice in winter. Note that because the shallowest observed depth level of 28 m is about 5-6 m deeper than late summer SML depth (as derived from CTD casts, see section 3.1.1), fall SML salinification associated to early season freeze-up cannot be observed until *after* the SML has deepened by 5-6 m. However, the good agreement between the salinity-derived ice-thickness and direct sonar measurements suggests a rapidly increasing SML depth at the onset of winter.

Chemical analysis of the stable oxygen isotope ratio ($\Delta^{18}O$) in water samples collected during the NABOS cruises in late summers 2013 and 2015 shows that up to ∼6-10 % of the water at 20 m depth across the mooring section (above the reach of the moorings) consists of meteoric water (a characterization that includes both river water and precipitation) (not shown; see Alkire et al. 2017). The fact that meteoric water is present in the SML throughout the entire section indicates that sea ice may be not the sole factor modifying seasonally SML salinity.

2.3.2 *Upper slope domain*

In this section, we identify possible drivers for the deep reaching temperature signal in the vicinity of the front.

ALONG-STREAM ADVECTION

In agreement with the description of signal advection within the ACBC (Pnyushkov et al. 2015), drivers for the observed seasonal cycle may originate from upstream locations. For example, Ivanov et al. (2009) found that seasonally changing surface waters off Spitsbergen retain their seasonality as they propagate to intermediate depths during their advection along the continental slope. A caveat of this hypothesis is that velocities change substantially across the slope (Fig. 2.12b), making it questionable as to whether the original upstream signal would "survive" a long period of advection all the way from Spitsbergen to the study site (approximately 1900 km) without being completely distorted by different advection rates across the slope.

On smaller spatiotemporal scales, this may look different, however. The seasonal signal in temperature with opposing sign at $M1_2$ and $M1_3$ may be interpreted as originating from a common upstream signal whose phase is shifted between the two moorings due to sheared flow during advection from the source to the mooring section. From the phase shift ($\sim$2.5 months, not shown) and the average current speed difference between the moorings (4.3 cm/s), it emerges that under the assumption of a constant along-stream advection rate, the source signal would have to originate $\sim$270 km upstream of the mooring array. This point of origin coincides with the Vilkitsky Strait outflow (see Fig. 2.1). Numerical models and chemical analyses suggest that seasonally varying volumes of cold and relatively fresh Kara Sea shelf water flow through the Vilkitsky Strait and Trough and merge with the ACBC to propagate eastwards along the upper part of the continental slope (Aksenov et al. 2011, Bauch et al. 2016, Janout et al. 2015). While Aksenov et al. suggested that the waters entering the Laptev Sea through the Vilkitsky Strait overlay waters within the ACBC, Janout et al. argued that the interaction between the two merging water

flows is not well known and requires further investigation. With no data available to quantify the process, we can only point toward the possibility that Vilkitsky Strait outflows either mix with ACBC waters or push them further offshore. The latter may be similar to processes further upstream, where the Barents Sea branch of the AW acts to displace the Fram Strait branch from the upper slope farther offshore into the basin interior as they converge at the St. Anna Trough (e.g. Rudels et al. 2000).

WIND-DRIVEN UPWELLING AT THE SLOPE

Dmitrenko et al. (2006) analyzed AW seasonality using mooring data from 2002-2004 at the eastern EB continental slope, and identified seasonally changing wind patterns as the main driver behind the observed AW seasonal cycle, which they interpreted as cross-shore shift of the AW core. The wind pattern in recent years has changed: for the 2013-2015 deployment period, ERA-Interim reanalysis data shows that summer wind conditions were generally easterly (Fig. 2.13), as opposed to westerly during 2003 (the only year for which Dmitrenko et al. had summer data), therefore favoring upwelling as opposed to downwelling. Likewise, easterly wind conditions prevailed when Janout et al. (2013) observed upwelling signatures in current profiles and thermohaline properties further onshore on the Laptev Sea shelf in 2009 and 2010.

During the deployment period, upwelling-favorable wind conditions (northeasterly to southeasterly) occurred about twice as often during summer (44 % of days) compared to winter (23 % of days). For comparison, the opposite downwelling-favorable wind conditions (northwesterly to southwesterly) occurred only on 15 % and 12 % of days in summer and winter, respectively. The direct effect of wind stress on the ocean is confined to the Ekman layer, in which a balance of turbulent drag and Coriolis force

is established (described by Ekman, 1905). The depth of this layer is given by:

$$d_E = \sqrt{2K_m/f} \tag{2.1}$$

with the Coriolis parameter f and the turbulent diffusivity K_m. For a typical value of $K_m = 0.1m^2s^{-1}$ and $f = 1.41710^{-4}s^{-1}$ at 77 °N, the estimated depth of the Ekman layer is 37 m. The effect of up- and downwelling-favorable winds on cross-shore currents relative to the velocity at the bottom of the Ekman layer can be seen in Fig. 2.14a. There is a surface intensified offshore current anomaly reaching 2.8 cm/s at 9 m depth during upwelling-favorable winds and a moderate onshore anomaly reaching 0.6 cm/s in downwelling-favorable wind conditions. For depths below the Ekman layer, contributions of up- or downweling circulations to cross-shore velocity profiles cannot easily be analyzed with the data at hand, because the shape of the profiles is governed by multiple factors, including other seasonal processes (e.g. advection or front displacement, as discussed in sections 4.2.1 and 4.2.3). A dedicated modeling study may be able to verify indirect (upwelling related) wind effects on the deeper ocean velocity profiles.

A seasonal breakdown of cross-shore velocity profiles under upwelling-favorable conditions referenced to the Ekman layer depth is shown in Fig. 2.14b. During summer and fall, the offshore anomalies (indicative of upwelling) are strongest, reaching 3.7 cm/s and 3.6 cm/s at 9 m depth, respectively. Note that the weight of the summer profile contributing to the mean is substantially greater than that of the fall profile (83 days of upwelling-favorable winds in summer compared to 32 days in fall). The change of direction of the fall profile between ∼20 m and ∼26 m indicates that some additional factor(s) play a role in shaping the profile. In winter and spring, the surface response to upwelling-favorable winds does not exceed 2.2 cm/s. We thus argue that the discussed features of the velocity

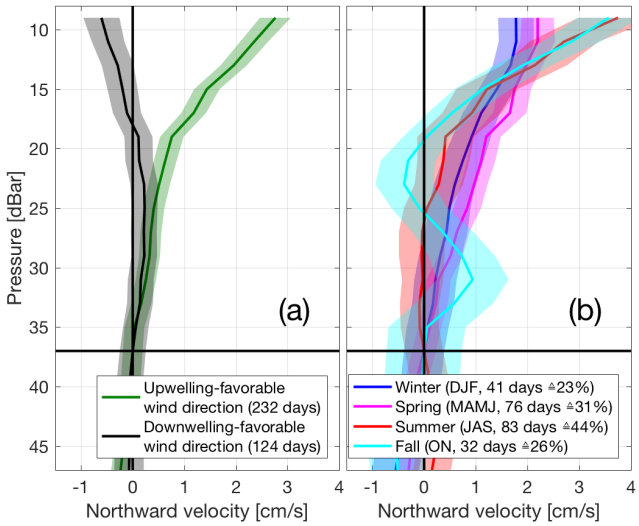

Figure 2.14: (a) Profiles of northward (approximately cross-shore) velocity anomalies relative to their velocity at the Ekman layer depth (37 m, horizontal black line) at the $M1_2$ mooring location averaged over all days with upwelling-favorable (northeasterly to southeasterly) wind direction (green) and over days with downwelling-favorable (northwesterly to southwesterly) wind direction (black). (b) Seasonal breakdown of the green profile in (a), again referenced to their velocity at the Ekman layer depth. Given in the legend are the months included in each season, the total number of upwelling-favorable wind days per season and what percentage of days per season that represents. Shading denotes one standard error of the mean.

profiles as well as the doubling of the number of upwelling-favorable wind conditions during summer strengthen the upwelling hypothesis.

Upwelling signatures also manifest in shoaling of isopycnals at the front near the slope in summer, relative to the preceding winter (Fig. 2.15 shows this at the example of the 27.84 isopycnal). Upwelled water may explain the observed summertime colder water onshore of the front (Fig. 2.7e).

We conclude that the upwelling hypothesis is qualitatively supported by the ERA-wind data, seasonal isopycnal pattern and upper ocean current observations, and is possibly an important driver for the lower temperatures close to the slope in summer. However, it cannot explain the large positive seasonal difference in temperature at the $M1_3$ mooring site (Fig. 2.7e). We also note that since upwelling is directly dependent on the large-scale atmospheric circulation, which is known to vary on inter-annual timescales

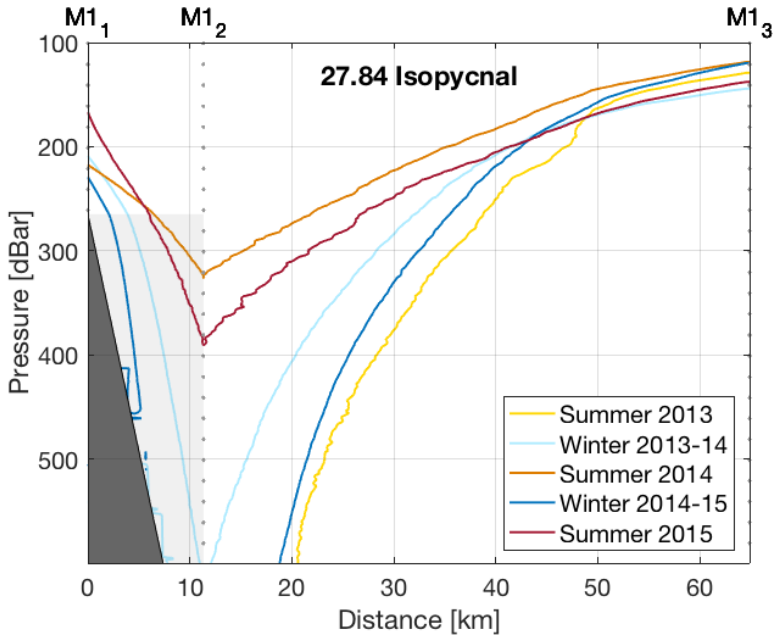

Figure 2.15: Seasonally averaged position of the 27.84 isopycnal at the three onshore-most moorings. Dark gray shading marks the approximate position of the continental slope, light gray shading indicates area where isolines are due to extrapolation as the depth difference between the moorings does not allow for horizontal interpolation.

as well as in response to sea ice loss (e.g. Overland and Wang 2010), the contribution of upwelling to the observed seasonality will change over time.

FRONT DISPLACEMENT

In addition to along-slope advection and upwelling, lateral displacement of the hydrographic front may be a factor in contributing to the seasonality observed in the USD. This relocation process can be linked to prevailing upwelling wind conditions, as has been observed, for example, by Houghton et al. (1994). They found that in the Middle Atlantic Bight, wind-driven upwelling events displace the local front onshore by about 20 km from its equilibrium position. Chapman (2000) explored the physical mechanisms defining shifts of the position of a front using an idealized

model. The model simulates a surface-to-bottom front between a buoyant shelf current and a homogeneous ocean on a sloping topography. The practical applicability of this simple model has been demonstrated in a number of publications (e.g. Hetland and Signell 2005, Weingartner et al. 2005). Chapman showed that, in accordance with Wright (1989), the bottom attachment point -or depth- of the front can be approximated as:

$$h_0 = (2U_0 f/\epsilon g)^{1/2} \tag{2.2}$$

with U_o the alongshore transport at the front, f the Coriolis parameter, $\epsilon = \Delta\rho/\rho_0$, the density anomaly across the front and g the gravitational acceleration. Note that the position of the front depends solely on the transport at the front and the density difference across it. Assuming that the front is located somewhere between the moorings $M1_2$ and $M1_3$, we can roughly estimate these variables: U_o is approximated as the mean of the vertically integrated (>750 m) transports at $M1_2$ and $M1_3$ multiplied by the distance between the moorings. Similarly, ϵ is calculated using the difference of vertically averaged density between these moorings (Table 2.1). Table 2.2 shows estimates for the front attachment depth (i.e. its position on the slope) dependent on either constant or seasonally-averaged density and transport. It emerges that seasonally changing density gradients counteract the effect of seasonally changing transports on the front attachment depth, but changes in transport are dominant in defining the observed seasonal movement of the front. The estimated front attachment depth h_o would thus be about 100 m shallower in summer ($\sim$608 m) compared to winter ($\sim$704 m) (Table 2.2) (both estimates are shallower than the expected $\sim$750 m depth of the front and are likely due to the idealized approach). At the eastern EB continental slope, a 100 m depth difference translates to a cross-slope displacement of about 4 km.

This seasonal movement of the front potentially contributes to the seasonal cycle observed in the USD. Reduced alongshore transport in

Table 2.1: Values for U_o, the alongshore transport at the front and $\epsilon = \Delta\rho/\rho_0$, the density anomaly across the front. Calculations were made using data from moorings $M1_2$ and $M1_3$ integrated over the top 750 m of the water column (see text for details). Overbars denote all-time (two-year) averages while primes indicate seasonal averages.

	ϵ'	U_0'	$\overline{\epsilon}$	$\overline{U_0}$
Summer	1.41 10^{-4}	1.8 10^6 m^3/s	1.57 10^{-4}	2.18 10^6 m^3/s
Winter	1.73 10^{-4}	2.96 10^6 m^3/s		

summer forces the front to move farther onshore, bringing warmer waters from the offshore AW core closer to the $M1_3$ mooring. The effect of this displacement on measurements at moorings onshore of the front ($M1_1$ and $M1_2$) depends on the shape of the front. Since the moored observations cannot fully resolve it (the depth difference between $M1_1$ and $M1_2$ is ∼500 m), there are two possibilities: Either the front is V-shaped (Gill 1973), as indicated by the isopycnals in Fig. 2.7a-d and Fig. 2.15, comprising a "wedge" of cold, fresh and less dense water in its center, or it is simply retrograde (sloping down towards the continental slope), as is hinted by repeat hydrographic sections (not shown). In the first case, the summertime onshore moving front may bring the cold water within the wedge towards $M1_1$ and $M1_2$ and thus contribute to the observed seasonality, in the latter case, the seasonality on-shore of the front cannot be explained by its seasonal displacement.

With the data at hand, we cannot draw final conclusions as to the seasonal movement of the front. A denser array of moorings in this region is needed in order to obtain direct observational evidence. However, we

Table 2.2: Front depth h_0 as by equation 2.2, calculated using different combinations of transport and density anomaly averages from table 2.1.

	$\overline{\epsilon}, U_0'$	$\epsilon', \overline{U_0}$	ϵ', U_0'
Summer h_0	576m	783m	608m
Winter h_0	739m	707m	704m
Δh_0	-163m	76m	-96m

hypothesize that due to the relatively small expected lateral displacement, frontal movement is arguably less important than upwelling and advection in shaping the seasonality in the USD.

ISOPYCNAL DISPLACEMENT IN THE COLD HALOCLINE LAYER

The origin of isopycnal displacement in the CHL of the USD as deduced from the seasonal salinity signal is too widespread (at least 60 km and across the front) and deep (down to ∼100 m) to be a direct consequence of any of the aforementioned mechanisms. Instead, we refer to the following section where the isopycnal displacement in the LSD is discussed in detail. Even though the signal in the USD is located in the CHL as opposed to the LHW in the LSD, it is not unlikely that both signals have a similar origin.

2.3.3 *Lower slope domain*

There are several potential contributors to the observed seasonal displacement of isopycnal surfaces in the LSD halocline. We argue that along-slope advection cannot play the dominant role in this seasonal cycle, because the intensity and direction of currents varies substantially across the LSD (Fig. 2.12b). This makes it difficult to explain the observed in-phase pattern of the seasonal signal at all moorings with lateral advection (Fig. 2.7e,f).

Alternatively, the observed isopycnal displacement may be linked to seasonal variations of sea-level height. Local sea-level variations are evaluated using a two-year long (2013-15) bottom pressure record from the Bottom Pressure Recorder (BPR) deployed the $M1_4$ mooring at 2720 m depth. Complementing the BPR are pressure measurements provided by five MicroCATs distributed between ∼600 m and ∼62 m at the mooring (Fig. 2.3). The bottom pressure shows a seasonal cycle with higher pressure in summer compared to winter with a seasonal difference of 0.068

dbar (Fig. 2.16c). A similar seasonality is observed at all five MicroCAT pressure records as evidenced by high correlations (R=0.69-0.74) and the same range of seasonal variations (exemplarily shown for the shallowest and deepest instruments in Fig. 2.16a,b). This suggests that the observed pressure changes originate in the upper 60 m layer and can be caused either by seasonal density variations in this layer or by sea-level change. Estimates based on the $M1_6$ upper ocean array data -(nearest neighbor) extrapolated to the surface- show that average seasonal density variability ($\Delta\ \sigma$=0.03 kg/m^3) can only account for 0.002 dbar of seasonal pressure change, over one order of magnitude less than the observed seasonal change at the BPR. Thus, we conclude that seasonal pressure variations are caused by sea-level changes, with elevated sea level (higher pressure) in summer and depressed sea level (lower pressure) in winter, with 0.068 dbar pressure difference. This is equivalent to about 6.8 cm of seasonal sea-level change.

Let us now compare the seasonal changes of sea level and isopycnal displacements. We first note the out-of-phase (i.e. opposed) displacement of isopycnals compared to the seasonal change of sea level, with 36 m elevation of isopycnal surfaces in winter relative to summer (section 3.1.3). This pattern follows the well-established baroclinic response of density interfaces to sea-level variations (e.g. Chaen and Wyrtki 1981). The baroclinic response can be further analyzed using theoretical considerations. For an idealized non-rotating two-layer ocean, the following expression was derived (e.g. Gill 1982):

$$\eta/h \approx -g'H_2/gH \tag{2.3}$$

where the ratio between the surface displacement (η) and the interface displacement (h) is approximated as a function of reduced gravity (g'=g(ρ_2- ρ_1)/ ρ_2 = 0.002 m/s^2), with ρ_1=1027.68 kg/m$_3$ and ρ_2=1027.96 kg/m$_3$, the densities of the upper layer and lower layer, respectively (derived

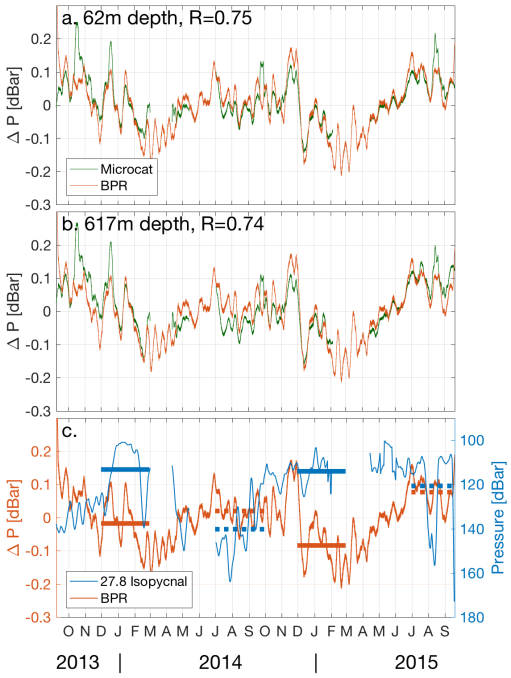

Figure 2.16: (a, b) Smoothed (using 7-day running mean) time series of pressure anomalies from the Bottom Pressure Recorder (BPR) at 2720 m depth and MicroCATs at approximately 62 m and 617 m depth at the $M1_4$ mooring. R denotes the correlation coefficient between the BPR and MicroCATs. (c) Time series of BPR pressure anomaly and 27.8 isopycnal pressure, both smoothed with a 7-day running mean. Thick horizontal solid and dotted lines mark winter and summer averages. Note that in the time series of MicroCAT pressures and isopycnal depth, three "dive events" are removed (March-April 2014, Mai-July 2014 and February-April 2015). During these events, the mooring was presumably tilted by currents, resulting in instruments effectively measuring several meters deeper than their intended depth.

from observations at the $M1_4$ mooring)), the equilibrium thickness of the lower layer (H_2=2590 m), gravity (g=9.81 m/s^2) and the total ocean depth (H=2720 m). Using this expression, the expected sea-level change needed to explain the observed 36 m isopycnal displacement is estimated to be 7 mm, or about one order of magnitude less than observed via the BPR. Thus, while observations and theoretical estimates qualitatively agree with out-of-phase displacements of sea level and the interface layer, quantitatively they differ substantially. This misfit is probably due to the high degree of simplification involving the theoretical considerations that may

not adequately represent the observed phenomenon. Further analysis is needed in order to understand this complex relationship between seasonal sea-level and isopycnal displacements.

2.4 CONCLUDING REMARKS

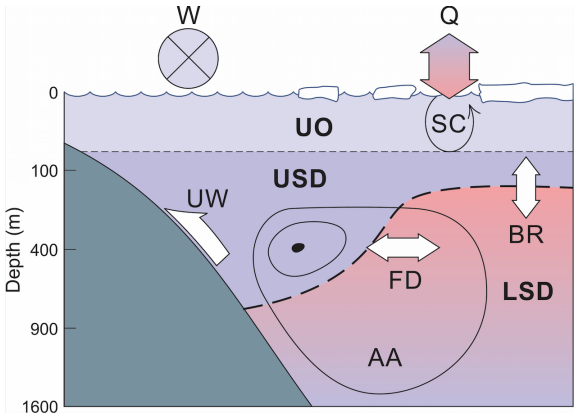

Figure 2.17: Sketch summarizing the different mechanisms of seasonality discussed in this study. Upper ocean (UO): seasonal convection (SC) due to brine rejection, wind mixing and surface heatfluxes (Q). Upper slope domain (USD): upwelling (UW) due to summertime easterly winds (W), alongstream advection (AA) within the ACBC and front displacement (FD). Lower slope domain (LSD): isopycnal displacement as baroclinic response (BR) to seasonal sea-level change.

The Laptev Sea continental slope area shows a complex pattern of seasonality. The individual cycles and their hypothesized drivers can be summarized as follows (Fig. 2.17):

- *Upper ocean*: Wintertime cooling and salinification due to sea ice formation impacts the upper ∼80 m of the water column.
- *Upper slope domain (USD) in the vicinity of the hydrographic front*: Signal advection within the ACBC, summertime wind-driven upwelling (in recent years) and cross-slope displacement of the front due to seasonal changes in alongshore dynamics may play a role in the temperature-dominated seasonality down to ∼600 m.

- *Lower slope domain (LSD) halocline*: Seasonality is caused by a vertical displacement of isopycnals of up to 36 m. A baroclinic response to seasonal sea-level changes is a potential driver behind this seasonality. With the data at hand we cannot pinpoint the final mechanism responsible for the sea-level variations.

Arguably, the most striking discovery is that of large temperature seasonality in the USD. A seasonal difference of up to 1.4 °C implies that a substantial shift of heat across the slope may take place with possible impacts on local dynamics, air-sea interactions and sea ice formation, making it imperative to investigate the extent to which the three potential drivers presented in this study contribute to the observed cycle and how persistent they are on inter-annual timescales. Furthermore, the large temperature variability, combined with the overall warming trend in this region may point towards increasing temperature's role in determining seawater density (see Carmack 2007, Timmermans et al. 2016).

The seasonality of the LSD halocline at $M1_4$ is the signal documented by Dmitrenko et al. (2009) and Polyakov et al. (2017) and found to have increased in recent years. This implies that the associated vertical displacement of isopycnals may also be increasing. Further research is needed to investigate whether extensive seasonal variability within the halocline increases mixing and thus contributes to its ongoing erosion and facilitate convection (thus representing a positive feedback) which was described as 'atlantification' of the Arctic Ocean by Polyakov et al. (2017). They observed an increased upward heat flux from the AW into the upper ocean with direct consequences for sea ice formation and a potential for impacting atmosphere/ocean exchange and the Arctic climate. Because such convection also involves other ocean properties, such as nutrients and components of the carbon cycle, it will likewise impact Arctic ecosystems (Bluhm et al. 2015). To make reasonable future projections, it is essential to fully understand the role of seasonality in this process.

While the NABOS mooring array enabled us to identify, for the first time, a complex pattern of seasonality in the eastern Eurasian Basin, its design is not ideal for a detailed analysis of each seasonal cycle. For a quantitative study, the spacing between moorings in the USD must be narrower to fully resolve the seasonal movement and shape of the front. Moorings with instruments reaching up closer to the surface are required to capture SML hydrography. Nevertheless, a set of plausible drivers of seasonality have been identified that may provide a base for further observational and modeling efforts seeking to better understand the variability of the eastern Arctic Ocean and the implications for global climate.

2.5 ACKNOWLEDGMENTS

The mooring- and ship-based oceanographic observations in the eastern EB were conducted within the framework of the NABOS project, with support from NSF (grants 1203473, 1249133 and 1203146) and the National Oceanic and Atmospheric Administration (grants NA150AR4310155 and NA150AR4310156). We would like to thank two anonymous reviewers for providing very insightful comments and suggestions that helped to improve the manuscript.

2.6 REFERENCES

Aagaard, K., 1989: A synthesis of the Arctic Ocean circulation. *Rapp. P.-v. Rcun. Cons. int. Explor. Mer*, **188**, 11–22, doi:10.4095/126774.

Aagaard, K., L. K. Coachman, and E. Carmack, 1981: On the halocline of the Arctic Ocean. *Deep Sea Research Part A. Oceanographic Research Papers*, **28**, 529–545, doi:10.1016/0198-0149(81)90115-1.

Aksenov, Y., V. V. Ivanov, A. J. G. Nurser, S. Bacon, I. V. Polyakov, A. C. Coward, A. C. Naveira-Garabato, and A. Beszczynska-Moeller, 2011: The Arctic Circumpolar Boundary Current. *J. Geophys. Res*, **116**, 11–28, doi:10.1029/2010JC006637.

Alkire, M. B., I. Polyakov, R. Rember, A. Pnyushkov, V. Ivanov, and I. Ashik, 2017: Combining physical and geochemical methods to investigate lower halocline water formation and modification along the Siberian continental slope. *Ocean Sci*, **13**, 983–995, doi:10.5194/os-13-983-2017.

Atkinson, D. E., 2005: Observed storminess patterns and trends in the circum-Arctic coastal regime. *Geo-Mar Lett*, **25**, 98–109, doi:10.1007/s00367-004-0191-0.

Barry, R. G., M. C. Serreze, J. A. Maslanik, and R. H. Preller, 1993: The Arctic Sea Ice-Climate System: Observations and modeling. *Reviews of Geophysics*, **31**, 397–422, doi:10.1029/93RG01998.

Bauch, D., E. Cherniavskaia, and L. Timokhov, 2016: Shelf basin exchange along the Siberian continental margin_ Modification of Atlantic Water and Lower Halocline Water. *Deep-Sea Research Part I*, **115**, 188–198, doi:10.1016/j.dsr.2016.06.008.

Bauch, D., S. Torres-Valdes, I. Polyakov, A. Novikhin, I. Dmitrenko, J. McKay, and A. Mix, 2014: Halocline water modification and along-slope advection at the Laptev Sea continental margin. *Ocean Sci*, **10**, 141–154, doi:10.5194/os-10-141-2014.

Bluhm, B. A., K. N. Kosobokova, and E. C. Carmack, 2015: A tale of two basins: An integrated physical and biological perspective of the deep Arctic Ocean. 1–33, doi:10.1016/j.pocean.2015.07.011.

Carmack, E. C., 2007: The alpha/beta ocean distinction: A perspective on freshwater fluxes, convection, nutrients and productivity in high-latitude seas. *Deep Sea Research Part II: Topical Studies in Oceanography*, **54**, 2578–2598, doi:10.1016/j.dsr2.2007.08.018.

Chaen, M., and K. Wyrtki, 1981: The 20 °C isotherm depth and sea level in the western equatorial pacific. *Journal of the Oceanographical Society of Japan*, **37**, 198–200, doi:10.1007/BF02309057.

Chapman, D. C., 2000: Boundary layer control of buoyant coastal currents and the establishment of a shelfbreak front. *J. Phys. Oceanogr*, **30**, 2941–2955, doi:10.1175/1520-0485(2001)031<2941:blcobc>2.0.co;2.

Coachman, L. K., and C. A. Barnes, 1963: The Movement of Atlantic Water in the Arctic Ocean. *ARCTIC*, **16**, 8–16, doi:10.14430/arctic3517.

Dee, D. P., and Coauthors, 2011: The ERA-Interim reanalysis: configuration and performance of the data assimilation system. *Quarterly Journal of the Royal Meteorological Society*, **137**, 553–597, doi:10.1002/qj.828.

Dmitrenko, I. A., and Coauthors, 2014: Heat loss from the Atlantic water layer in the northern Kara Sea: causes and consequences. *Ocean Sci*, **10**, 719–730, doi:10.5194/os-10-719-2014.

Dmitrenko, I. A., and Coauthors, 2009: Seasonal modification of the Arctic Ocean intermediate water layer off the eastern Laptev Sea continental shelf break. *J. Geophys. Res*, **114**, 11, doi:10.1029/2008JC005229.

Dmitrenko, I. A., I. V. Polyakov, S. A. Kirillov, L. A. Timokhov, H. L. Simmons, V. V. Ivanov, and D. Walsh, 2006: Seasonal variability of Atlantic water on the continental slope of the Laptev Sea during 2002–2004. *Earth and Planetary Science Letters*, **244**, 735–743, doi:10.1016/j.epsl.2006.01.067.

Ekman, V W. 1905. "On the Influence of the Earth's Rotation on Ocean-Currents.*Arkiv Mat., Astr., Fys.* 2 (11).

Environmental Working Group, 1997: *Joint U.S.-Russian Atlas of the Arctic Ocean, Version 1*. L. Timokhov and F. Tanis, Eds.

Fer, I., A. K. Peterson, A. Randelhoff, and A. Meyer, 2017: One dimensional evolution of the upper water column in the Atlantic sector of the Arctic Ocean in winter. *J. Geophys. Res. Oceans*, **122**, 1665–1682, doi:10.1002/2016JC012431.

Gill, A. E., 1973: Circulation and bottom water production in the Weddell Sea. *Deep Sea Research and Oceanographic Abstracts*, **20**, 111–140, doi:10.1016/0011-7471(73)90048-X.

Gill, A. E., 1982: Atmosphere-Ocean Dynamics. 1–681.

Hetland, R. D., and R. P. Signell, 2005: Modeling coastal current transport in the Gulf of Maine. *Deep Sea Research Part II: Topical Studies in Oceanography*, **52**, 2430–2449, doi:10.1016/j.dsr2.2005.06.024.

Houghton, R. W., C. N. Flagg, and L. J. Pietrafesa, 1994: Shelf-slope water frontal structure, motion and eddy heat flux in the southern Middle Atlantic Bight. *Deep Sea Research Part II: Topical Studies in Oceanography*, **41**, 273–306, doi:10.1016/0967-0645(94)90024-8.

Ivanov, V. V., and Coauthors, 2009: Seasonal variability in Atlantic Water off Spitsbergen. *Deep Sea Research Part I: Oceanographic Research Papers*, **56**, 1–14, doi:10.1016/j.dsr.2008.07.013.

Janout, M. A., and Coauthors, 2015: Kara Sea freshwater transport through Vilkitsky Strait: Variability, forcing, and further pathways toward the western Arctic Ocean from a model and observations. *J. Geophys. Res. Oceans*, **120**, 4925–4944, doi:10.1002/2014JC010635.

Janout, M. A., J. Hölemann, and T. Krumpen, 2013: Cross-shelf transport of warm and saline water in response to sea ice drift on the Laptev Sea shelf. *J. Geophys. Res. Oceans*, **118**, 563–576, doi:10.1029/2011JC007731.

Lique, C., and M. Steele, 2012: Where can we find a seasonal cycle of the Atlantic water temperature within the Arctic Basin? *J. Geophys. Res. Oceans*, **117**, n/a–n/a, doi:10.1029/2011JC007612.

Maslanik, J. A., C. Fowler, J. Stroeve, S. Drobot, J. Zwally, D. Yi, and W. Emery, 2007: A younger, thinner Arctic ice cover: Increased potential for rapid, extensive sea-ice loss. *Geophys. Res. Lett*, **34**, C10017–5, doi:10.1029/2007GL032043.

Monterey, G. I., and S. Levitus, 1997: *Climatological Cycle Of Mixed Layer Depth In The World Ocean US Gov*. Printing Office: NOAA NESDIS.

Overland, J. E., and M. Wang, 2010: Large-scale atmospheric circulation changes are associated with the recent loss of Arctic sea ice. *Tellus A: Dynamic Meteorology and Oceanography*, **62**, 1–9, doi:10.1111/j.1600-0870.2009.00421.x.

Pnyushkov, A. V., I. V. Polyakov, V. V. Ivanov, Y. Aksenov, A. C. Coward, M. Janout, and B. Rabe, 2015: Structure and variability of the boundary current in the Eurasian Basin of the Arctic Ocean. *Deep Sea Research Part I: Oceanographic Research Papers*, **101**, 80–97, doi:10.1016/j.dsr.2015.03.001.

Pnyushkov, A., and Coauthors, Heat, salt, and mass transports in the eastern Eurasian Basin of the Arctic Ocean, from two years of mooring observations. *Deep Sea Research Part I: Oceanographic Research Papers*.

Polyakov, I., 1999: Modeling of the seasonal variability in the Arctic Ocean. *Oceanology*, 493–503.

Polyakov, I. V., A. V. Pnyushkov, R. Rember, L. Padman, E. C. Carmack, and J. M. Jackson, 2013: Winter Convection Transports Atlantic Water Heat to the Surface Layer in the Eastern Arctic Ocean. *J. Phys. Oceanogr*, **43**, 2142–2155, doi:10.1175/JPO-D-12-0169.1.

Polyakov, I. V., A. Y. Proshutinsky, and M. A. Johnson, 1999: Seasonal cycles in two regimes of Arctic climate. *J. Geophys. Res. Oceans*, **104**, 25761–25788, doi:10.1029/1999JC900208.

Polyakov, I. V., and Coauthors, 2017: Greater role for Atlantic inflows on sea-ice loss in the Eurasian Basin of the Arctic Ocean. *Science*, doi:10.1126/science.aai8204.

Rudels, B., A.-M. Larsson, and P.-I. Sehlstedt, 1991: Stratification and water mass formation in the Arctic Ocean: some implications for the nutrient distribution. *Polar Research*, **10**, 19–32, doi:10.3402/polar.v10i1.6724.

Rudels, B., E. P. Jones, L. G. Anderson, and G. Kattner, 1994: On the Intermediate Depth Waters of the Arctic Ocean. *The Polar Oceans and Their Role in Shaping the Global Environment*, Vol. 188 of *Johannessen/The Polar Oceans and Their Role in Shaping the Global Environment*, American Geophysical Union, Washington, D. C., 33–46.

Rudels, B., L. G. Anderson, and E. P. Jones, 1996: Formation and evolution of the surface mixed layer and halocline of the Arctic Ocean. *J. Geophys. Res. Oceans*, **101**, 8807–8821, doi:10.1029/96JC00143.

Rudels, B., R. D. Muench, J. Gunn, U. Schauer, and H. J. Friedrich, 2000: Evolution of the Arctic Ocean boundary current north of the Siberian shelves. *Journal of Marine Systems*, **25**, 77–99, doi:10.1016/S0924-7963(00)00009-9.

Timmermans, M.-L., S. R. Jayne, M.-L. Timmermans, and S. R. Jayne, 2016: The Arctic Ocean Spices Up. *J. Phys. Oceanogr, http://dx.doi.org/10.1175/JPO-D-16-0027.1*, **46**, 1277–1284, doi:10.1175/JPO-D-16-0027.1.

Timofeev, V. T., 1960: Water Masses of the Arctic Basin. *Gidrometeoizdat*, p.190.

Torrence, C., and G. P. Compo, 1998: A Practical Guide to Wavelet Analysis. *Bull. Amer. Meteor. Soc*, **79**, 61–78, doi:10.1175/1520-0477(1998)079<0061:APGTWA>2.0.CO;2.

Weingartner, T. J., S. L. Danielson, and T. C. Royer, 2005: Freshwater variability and predictability in the Alaska Coastal Current. *Deep Sea Research Part II: Topical Studies in Oceanography*, **52**, 169–191, doi:10.1016/j.dsr2.2004.09.030.

Wright, D. G., 1989: On the Alongshelf Evolution of an Idealized Density Front. *J. Phys. Oceanogr,* ***19****, 532–541, doi:10.1175/1520-0485(1989)019<0532:OTAEOA>2.0.CO;2*.

3

SEMIDIURNAL CURRENT DYNAMICS IN THE ARCTIC OCEAN'S EASTERN EURASIAN BASIN

Till M. Baumann[1], Igor V. Polyakov[1], Laurie Padman[2], Seth Danielson[3], Ilker Fer[4], Susan Howard[2], Jenny Hutchings[5], Markus Janout[6], An Nguyen[7], Andrey V. Pnyushkov[8]

1 *International Arctic Research Center and College of Natural Science and Mathematics, University of Alaska Fairbanks (UAF), Fairbanks, AK, USA and Finnish Meteorological Institute, Helsinki, Finland*

2 *Earth & Space Research, Corvallis, OR, USA*

3 *College of Fisheries and Ocean Sciences, UAF, Fairbanks, AK, USA*

4 *Geophysical Institute, University of Bergen and Bjerknes Centre for Climate Research, Bergen, Norway*

5 *College of Earth, Ocean and Atmospheric Sciences, Oregon State University, Corvallis, OR, USA*

6 *Alfred Wegener Institute Helmholtz Centre for Polar and Marine Research, Bremerhaven, Germany*

7 *University of Texas at Austin, Institute for Computational Engineering and Sciences, Austin, TX, USA*

8 *International Arctic Research Center, UAF, Fairbanks, AK, USA*

Citation: Baumann, T.M., Polyakov, I.V.,Padman, L.,Danielson, S., Fer, I., Howard, S., Hutchings, J., Janout, J., Nguyen, A.T., Pnyushkov, A.V., in review. Semidiurnal current dynamics in the Arctic Ocean's eastern Eurasian Basin. Journal of Physical Oceanography

Abstract

In the Arctic Ocean, semidiurnal-band processes including tides and wind-forced inertial oscillations are significant drivers of ice motion, ocean currents and shear contributing to mixing. Two years (2013-2015) of current measurements from seven moorings deployed along 125° E from the Laptev Sea shelf (∼50 m) down the continental slope into the deep Eurasian Basin (∼3900 m) are analyzed and compared with models of baroclinic tides and inertial motion to identify the primary components of semidiurnal-band current (SBC) energy in this region. The strongest SBCs, exceeding 30 cm/s, are observed during summer in the upper ∼30 m throughout the mooring array. The largest upper-ocean SBC signal consists of wind-forced oscillations during the ice-free summer. Strong barotropic tidal currents are only observed on the shallow shelf. Baroclinic tidal currents, generated along the upper continental slope, can be significant. Their radiation away from source regions is governed by critical latitude effects: the S_2 baroclinic tide (period = 12.000 h) can radiate northwards into deep water but the M_2 (∼12.421 h) baroclinic tide is trapped to the continental slope. Baroclinic upper-ocean tidal currents are sensitive to varying stratification, mean flows and sea ice cover. This time-dependence of baroclinic tides complicates our ability to separate wind-forced inertial oscillations from tidal currents. Since the shear from both sources contributes to upper-ocean mixing that affects the seasonal cycle of the surface mixed layer properties, a better understanding of both, inertial motion and baroclinic tides is needed for projections of mixing and ice-ocean interactions in future Arctic climate states.

3.1 INTRODUCTION

The Eurasian Basin (EB) of the Arctic Ocean comprises the Nansen Basin and Amundsen Basin (Fig. 3.1). Our study region is confined to east of

Severnaya Zemlya (∼95° E), and is characterized by a continental slope ascending from the abyssal plain (∼3900 m) to the shallow Laptev Sea shelf (∼50 m). We refer to this whole region (comprising the deep basin, continental slope and Laptev Sea shelf) as "eastern EB". The hydrography in the eastern EB continental slope region is strongly affected by the Arctic Circumpolar Boundary Current (ACBC). Atlantic Water enters the Arctic Ocean through Fram Strait and the Barents Sea and is carried by the ACBC cyclonically along the continental margins and ridges of the Arctic Ocean at intermediate depths of about 200-1000 m (Timofeev 1960; Coachman and Barnes 1963; Aagaard 1989; Rudels et al. 1994; Pnyushkov et al. 2018a); see Figs.3.1 and3.2. Substantial changes in stratification have been observed in the eastern Arctic Ocean in recent years, associated with increasing importance of Atlantic Water inflows (Polyakov et al. 2017). This "atlantification" of the eastern Arctic coincides with increases in instantaneous current speeds and velocity shear in the basin, which are associated with a regime change from a calm double-diffusive to a more vigorous shear-driven mixing environment (Polyakov et al., submitted). These changes may play a direct role in the observed reduction of sea ice volume and an indirect role through feedbacks (e.g. Carmack et al. 2015).

Turbulent mixing, below the well-mixed surface layer, is driven by shear instabilities. In the eastern Arctic, much of the shear can be attributed to semidiurnal baroclinic waves (e.g. Polyakov et al., submitted), either tides or wind-forced near-inertial motion. Observations of semidiurnal currents from Arctic Ocean moorings reveal strong seasonal variability related to changes in the sea ice cover (Rainville and Woodgate 2009; Pnyushkov and Polyakov 2012). Models of baroclinic tides generated by barotropic tidal flow over steep and/or rough bathymetry indicate that tidal currents are also sensitive to background stratification and currents. These prior studies suggest that changes in sea ice cover, stratification and circulation

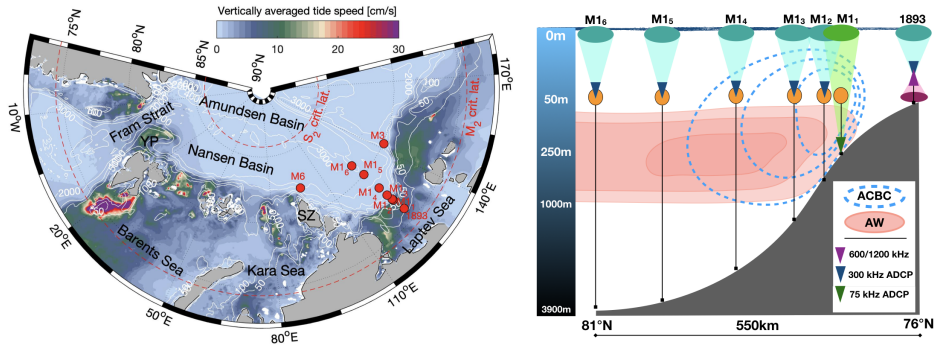

Figure 3.1: Left: Map showing vertically averaged barotropic tidal current speed from the inverse barotropic tidal model of Padman & Erofeeva (2004) for the Atlantic side of the Arctic Ocean. Dashed red lines indicate the critical latitude of the S_2 and M_2 constituents. White lines and labels show isobaths. Red dots indicate the positions of moorings whose data are used in this study. YP = Yermak Plateau, SZ = Severnaya Zemlya. Right: sketch (not to scale) of the moorings comprised in the section along 125°E and their approximate location relative the Atlantic Water (AW) layer and the Arctic Circumpolar Boundary Current (ACBC).

in the eastern Arctic could cause substantial changes in the intensity of shear instabilities and the associated turbulent mixing.

As a step towards a better understanding of future changes in eastern Arctic current dynamics, we investigate the sources and variability of upper-ocean semidiurnal-band energy across the eastern EB continental slope. The paper is organized as follows. In **section 2** we summarize our present knowledge of Arctic tidal currents and wind-forced inertial motion, and their contributions to the state of the Arctic ocean and ice system. We then describe a data set of upper-ocean currents collected in the eastern EB during 2013-2015, and the analysis methods we use to discuss contributions to the semidiurnal band variability (**section 3**). The results of the tidal analysis are presented in **section 4**. In **section 5**, we discuss the results, including shortcomings of classical harmonic tidal analysis. The summary of our findings is provided in **section 6**.

Table 3.1: Principal semidiurnal tidal constituents and their periods (in hours) as well as inertial periods (f) for the southern and northern extremes of the mooring array, and Rayleigh periods (time for separation of two components by one cycle in days, calculated as $1/(\omega_1\text{-}\omega_2)$, with $\omega_{1,2}$ being the frequencies of the two components to be separated). Adapted from Padman et al. (2018).

	Period (h)	Rayleigh period (days)									
		K_2	S_2	f_{north}	f_{south}	M_2	N_2	K_1	P_1	O_1	Q_1
K_2	11.967	-	182.63	41.75	16.78	13.66	9.13	1	0.99	0.93	0.9
S_2	12		-	54.12	18.48	14.76	9.61	1	1	0.93	0.9
f_{north}	12.112			-	-	20.3	11.69	1.02	1.02	0.95	0.92
f_{south}	12.334				-	73.38	20.03	1.06	1.05	0.98	0.95
M_2	12.421					-	27.55	1.08	1.07	1	0.96
N_2	12.658						-	1.12	1.11	1.03	1
K_1	23.934							-	182.63	13.66	9.13
P_1	24.066								-	14.76	9.61
O_1	25.819									-	27.55
Q_1	26.868										-

3.2 TIDAL AND WIND-FORCED INERTIAL CURRENTS IN THE ARCTIC

Variability of semidiurnal band current (SBC) velocities and associated mixing processes in the upper Arctic Ocean has usually been attributed to wind-driven inertial currents that depend directly on sea ice cover and changes in wind stress (e.g. Rainville and Woodgate 2009; Martini et al. 2014; Fer 2014). For some portions of the Arctic continental shelves and slopes, however, tidal variability may also play a substantial role: for a record from the Beaufort Sea shelf, Kulikov et al. (2004) found that the tidal contribution to the observed signal is spatially highly variable but reaches up to 74% of the total signal.

The periods of the eight most energetic tidal constituents (**Table 1**) range from 11.967 h to 26.868 h. The inertial period, T_I=2/f, where f=2sin() is the Coriolis frequency, is the planetary rotation rate and is the latitude, ranges from ∼12.334 h to ∼12.112 h over the latitude range of the mooring array (∼76-81°N). The close spacing of semidiurnal tidal and inertial periods complicates empirical separation of these components; see **section 3**.

3.2.1 *Tides*

Tidal currents play an important role in shaping the Arctic Ocean hydrography and sea ice cover; see, for example, Kowalik and Proshutinsky (1994), Holloway and Proshutinsky (2007) and Luneva et al. (2015). Tidal currents can be partitioned into barotropic and baroclinic components, with the barotropic currents representing the fraction that would be present in a homogeneous ocean with a free surface, and baroclinic currents being associated with the presence of stratification. Barotropic tidal currents vary regionally but are relatively uniform over time and depth at any location. Exceptions are frictional boundary layers, close to the top and bottom of the water column, which may expand substantially close to the critical latitude (described below), and diurnal tides that can vary with changes in along-slope currents (e.g. Skarðhamar et al. 2015). Barotropic tidal models (e.g. Kowalik and Proshutinsky 1994; Padman and Erofeeva 2004) based on the depth-integrated momentum and continuity equations provide amplitude and phase coefficients of tide height and depth-averaged currents for major tidal constituents throughout the Arctic. These models show very little barotropic tidal energy (currents <0.5 cm/s) in the central Arctic deep basins, but strong amplitudes (>10 cm/s) over portions of the continental shelves (Fig. 3.1).

Where barotropic tidal currents flow across steep slopes or rough topography in the presence of stratification, energy can be converted from barotropic to baroclinic (internal) tides whose energy finally dissipates in mixing processes (e.g. Wunsch 1975; Simmons et al. 2004). In contrast to barotropic tides, for baroclinic tides the processes of generation, propagation and dissipation are very sensitive to stratification, mean flow, and energy losses through friction and mixing within the water column. They may, therefore, change substantially in time with variations in the background ocean state associated with weather-band and seasonal changes

in forcing, ocean mesoscale variability such as eddies (e.g. Pnyushkov et al. 2018b), and as the Arctic Ocean changes on longer time scales (e.g. Carmack et al. 2015).

Baroclinic tidal waves cannot freely propagate poleward of their critical latitude, the latitude at which their frequency equals the local inertial frequency (e.g. Prinsenberg and Bennett 1989). For diurnal tides, this latitude is roughly 30° , and all baroclinic diurnal energy in the Arctic is trapped to the "wave guide" of the continental slope (Kowalik & Proshutinsky 1993). For the dominant semidiurnal tide M_2 (period ∼12.42 h), the critical latitude is ∼74.5° N while for S_2 (period of 12.00 h) it is ∼86° N (see Fig. 3.1). Most of the EB continental slope is between these latitudes, suggesting that baroclinic S_2 tides can propagate freely across-slope but M_2 cannot. Instead, the energy either radiates along the slope (Hughes and Klymak 2019) or is dissipated locally through mixing or nonlinear energy transfer to high frequency waves (e.g. Falahat et al. 2015; Rippeth et al. 2017; Kozlov et al. 2017).

Regions of high tidal energy along the shelf edges generally coincide with the pathway of Atlantic Water in the ACBC through the eastern Arctic. The phenomenon of tidal energy conversion and turbulent mixing has been studied in detail near the Yermak Plateau, north of Svalbard (e.g. Padman et al. 1992; Fer et al. 2010; 2015). There, intense tide-forced mixing cools and freshens the incoming AW. Using a general circulation model with a relatively simple parameterization of tidal friction at the seabed, Holloway & Proshutinsky (2007) proposed that tides were a critical component of mixing responsible for setting the distributions of Atlantic Water hydrographic properties throughout the Arctic. Limited microstructure measurements obtained across the Arctic Ocean between 2007 and 2013 support the notion of tidally driven mixing along the continental margins, but the dissipation strongly depends on the steepness of the continental slope and generally decreases in the eastward direction along the Atlantic

Water path (Rippeth et al. 2015). However, Lenn et al. (2011) found intense tidally driven mixing far east on the continental shelf of the Laptev Sea, in a region where Janout and Lenn (2014) found strong M_2 tidal currents (up to ∼30 cm/s) that experienced substantial seasonal changes as stratification varied. Pnyushkov and Polyakov (2012) reported that, further offshore over the continental slope at the $M1_4$ mooring location at 2700 m (see Fig. 3.1 for location), tidal currents were weak ($O(1)$ cm/s) in winter but increased to >8 cm/s during ice-free summer months. Interpretation of the variability in semidiurnal-band currents is, however, complicated by the seasonal covariation of several factors including changing sea ice, ocean stratification (discussed in **section 5.1**) and wind forcing as a driver of near-inertial waves that are close in frequency to the most energetic semidiurnal tidal constituents (Table 3.1).

The interactions between sea ice cover and tides are complex. For high-concentration pack ice, the ice provides a frictional boundary that may increase energy dissipation (Morison et al. 1985), potentially leading to a deepening of the surface mixed layer (SML) (Padman et al. 1992). For low-concentration or easily deformed thin ice, however, reported effects on tidal currents and associated dissipation range from negligible (e.g. Danielson and Kowalik 2005; Rippeth et al. 2015) to substantial (e.g. Pnyushkov and Polyakov 2012). At the same time, stress from tidal currents at the ice base can force tidal motion of the sea ice. If the tidal stress is periodically divergent, tides can increase the time-averaged fraction of leads in sea ice cover (Mack et al. 2013), which may cause substantial changes in upper ocean hydrography with implications for mixing and new sea ice formation (e.g. Padman and Kottmeier 2000; Padman et al. 2006; Hutchings and Heil 2012). A modeling study by Kowalik and Proshutinsky (1994) suggested that this process leads to substantial changes in the seasonal cycle of ice volume growth and loss in the Arctic Ocean. Holloway and Proshutinsky (2007) reported much smaller impacts of tides on sea ice; however, Luneva

et al. (2015) found that the addition of tidal currents to an atmospherically forced three-dimensional simulation reduced pan-Arctic sea ice volume by ∼15% . Those authors attributed this sea ice reduction to the entrainment of warm subsurface Atlantic Water into the cold near-surface waters by increased surface stresses, and by upper-ocean shear instabilities from the combination of baroclinic tides and the atmospherically forced three-dimensional circulation.

3.2.2 *Wind-forced inertial currents*

The inertial frequency is the natural frequency of sea ice and ocean current responses to changes in wind stress. The efficiency of the transfer of momentum from atmosphere to ocean depends on the presence and properties of sea ice. From ice tethered profiler data, Cole et al. (Cole et al. 2018) found that the energy of the internal wave field, generated by inertial motions, is weakest for near 100% ice cover and abruptly increases once sea ice concentration drops below ∼80% . Inertial internal waves below the SML can propagate freely and eventually dissipate, redistributing wind energy through the water column (Munk and Wunsch 1998). Although the Arctic Ocean is historically known as having relatively low wind-forced total internal wave energy (Levine et al. 1985), evidence for the importance of inertial motions in the Arctic is well documented from measurements of ocean currents (e.g. Rainville and Woodgate 2009; Fer 2014; Martini et al. 2014) and sea ice drift (e.g. Gimbert et al. 2012). Observations suggest increases in variability and amplitude of the near-inertial wave field in recent years, which are mostly attributed to the widespread reduction of sea ice cover and thickness (Dosser et al. 2016).

3.3 DATA AND ANALYSIS METHODS

3.3.1 *Data*

3.3.1.1 *The 125° E Mooring array*

The principal dataset used in this study consists of moored observations from the Nansen and Amundsen Basin Observational System (NABOS) project (https://uaf-iarc.org/NABOS/). An array of six moorings ($M1_1$–$M1_6$) along the 125° E meridian from just offshore of the Laptev Sea shelf (∼77° N; 250 m water depth) to the abyssal plain (∼81° N; 3900 m depth) was deployed for two years from September 2013 to September 2015 (Fig. 3.1, see Table 3.2 for bottom depth at each mooring). All moorings were designed to obtain profiles of velocity ($\mathbf{u}(t,z)$, with orthogonal components u (eastward) and v (northward)) over limited depth ranges (see Table 3.2), and measurements of temperature and salinity at fixed depths. Velocities were obtained at hourly resolution for the upper ∼50 m using 300kHz Acoustic Doppler Current Profiler (ADCP) instruments at all moorings except for $M1_1$, where a 75kHz ADCP moored near the seabed was used to capture velocities throughout most of the water column, and mooring $M1_5$, which missed its target depth and was deployed ∼30 m too deep. The ADCPs generally returned full 2-year data records; however, the ADCP at $M1_5$ stopped working after about 10 months.

Manufacturer-provided accuracies for speeds and directions are ± 0.5 cm/s and ± 2° for vertical averaging bin sizes of 2 m and 5 m for the 300kHz and 75kHz ADCPs, respectively. Signals from all ADCPs were contaminated close to the surface by surface reflections of sidelobe energy. This error depends on the range, bin size and beam angle of the ADCP. For the upward-looking 300kHz ADCPs moored near 50 m depth, the upper 8 m could not be used; for the 75kHz ADCP mounted at ∼250 m depth at $M1_1$, the top 30 m was discarded.

The NABOS mooring array was supplemented by mooring 1893, deployed in September 2013 on the Laptev Sea shelf in ∼50 m water depth near 76° N, 126° E, within the German-Russian "Laptev Sea System" partnership during the Transdrift 21 expedition. The mooring was recovered and redeployed in 2014 during Transdrift 22 to obtain an additional year of data. Both deployments carried an upward-looking 300kHz ADCP at 35 m (2013) and 37 m (2014) depth, and downward-looking, higher frequency-instruments (600kHz mounted at 30 m in 2013 and 1200kHz at 35 m in 2014) to resolve the near-bottom part of the water column.

3.3.1.2 *Additional mooring data*

Moorings M3 (∼80° N, 142° E in 1360 m of water) and M6 (∼82° N, 97° E in 2700 m) were located outside the main mooring array (see Fig. 3.1 for their locations). Each was equipped with 75kHz and 300kHz ADCPs, recording hourly with vertical averaging bin sizes of 5 m and 2 m, respectively. The 75kHz ADCPs sampled currents from 450-200 m depth and the 300kHz ADCPs were deployed at ∼60 m depth to monitor the upper ocean. We used these data to evaluate the relationship between upper-ocean averaged currents and mid-depth, quasi-barotropic tidal currents.

3.3.1.3 *Sea ice and atmospheric conditions*

Local sea ice concentration and 10-m winds at each mooring location were obtained from ERA5 reanalysis output (Copernicus Climate Change Service 2017), which has a spatial grid spacing of 0.25° and temporal sampling of 1 h. We used modeled winds and sea ice to simulate wind-forced inertial currents in the surface mixed layer (SML, **section 3.2.4**).

3.3.2 *Methods*

3.3.2.1 *Semidiurnal-band currents*

In order to quantify the properties and spatio-temporal changes in the semidiurnal band current (SBC) energy, we band-passed the current records to retain only signals between 10-h and 14-h periods; this gives an effective modulation time scale of about 36 h. We performed the filtering with a band-pass Butterworth filter, applied separately to the u and v components.

3.3.2.2 *Harmonic tidal analysis*

We analyzed the current velocities using the T_TIDE Matlab toolbox (Pawlowicz et al. 2002), which is based on tidal analysis methods described by Foreman (1978). T_TIDE performs a harmonic analysis based on the known frequencies for up to 69 tidal constituents and calculates all relevant tidal ellipse parameters (major and minor axis amplitudes, orientation, sense of rotation direction and phase) with their confidence intervals.

The number of resolvable constituents is determined by the length of the time series. In most ocean environments, the bulk of the total tidal variance is in eight constituents, four semidiurnals (M_2, S_2, K_2, N_2) and four diurnals (O_1, K_1, P_1, Q_1); see Table 3.1 for periods of these constituents. Formal separation of these eight constituents requires about 183 days (six months) of data (Table 3.1). Tidal analysis on shorter records (e.g. 30 days, as commonly available from temporary tide gauge deployments, and as used in our study), report the combination of S_2 and K_2 as S_2 only, while K_1 and P_1 are reported as K_1. For barotropic tide heights, where amplitudes and phases are stable in time, these pairs can be separated in short records by "inference" (Foreman 1978; Pawlowicz et al. 2002). In the present analysis, however, we expect that much of the tidal energy is in time-varying baroclinic modes where the assumptions required for

inference may not apply. For analysis of short records, we therefore define the inseparable sum of K_1 and P_1 as K_1* and the sum of S_2

and K_2 as S_2* .

With the exception of barotropic tidal estimates in the following section, all tidal analysis presented in this study is based on the application of T_TIDE to 30-day sliding windows, run over the whole record at each depth level. This analysis yields a full set of tidal ellipse parameters at the same time and depth coordinates as the raw data (excluding the first and last 15 days of each record). T_TIDE also provides a "tidal prediction", derived from the summation of currents for all tidal constituents with sufficiently high signal-to-noise ratio. We refer to the east and north components of these currents as $u_{\text{T\_TIDE}}$ and $v_{\text{T\_TIDE}}$, respectively. The resulting time series of speed is then defined as $|\mathbf{u}|_{\text{T\_TIDE}}=(u_{\text{T\_TIDE}}{}^2 + v_{\text{T\_TIDE}}{}^2)^{1/2}$, with the subscripts reminding the reader that these are not necessarily true tidal currents but are the tidal reconstructions from the T_TIDE analyses.

3.3.2.3 *Differentiating between barotropic and baroclinic tidal currents*

The barotropic component of tidal currents is the component that would be present in an ocean of homogeneous potential density. Barotropic tide models (e.g. Kowalik and Proshutinsky 1994; Padman and Erofeeva 2004) evaluate the vertically integrated transport, and define the barotropic tidal current as the depth-averaged current (transport divided by total water depth). In three-dimensional tide-forced models with stratification (e.g. Mueller et al. 2012; 2018), the barotropic component is also evaluated as the depth-averaged current, and the baroclinic component is defined as the depth-dependent current anomaly relative to the barotropic value.

If velocity data are available for the entire water depth, partitioning total tidal currents into barotropic and baroclinic components could be achieved as for three-dimensional models. However, with the exception of

mooring 1893 on the shelf and mooring $M1_1$ on the upper slope, the ADCP observations along the 125° E array span only small portions of the entire water column; therefore, the instantaneous depth average of measured currents is not necessarily a good measure of the barotropic current. To investigate the dependence of averaged tidal currents on the vertical coverage of observations, we utilized moorings $M1_1$, M3 and M6, whose observations span most of the water column ($M1_1$) or a substantial part of the interior ocean (M3 and M6: 200-450 m depth) and can, therefore, be expected to yield a reasonable approximation of barotropic tidal currents.

For each mooring M3 and M6, we performed a single T_TIDE analysis on the full (∼2-year) records obtained from depth-averaging of currents from each ADCP. We treat the mid-depth records as the best estimate of the barotropic current. For mooring $M1_1$, we used the T_TIDE analysis of the entire depth range sampled by the 75kHz ADCP (30-230 m, in 250 m of water; see Table 3.2) to represent the barotropic current, and the depth-average for 30-65 m from the same instrument as the upper-ocean time series.

At the $M1_1$ mooring location, upper-ocean tidal currents of all major tidal constituents are about twice as large as the barotropic tidal currents (see Table A3.1 and Fig. A3.1 of the appendix). Orientation, eccentricity and phase are largely unaffected (note that there is a 180° ambiguity in orientation, as seen, for example, for O_1). At moorings M3 and M6, only the leading semidiurnal constituents (M_2 and S_2) have significant major axis amplitudes. At mooring M3, upper-ocean major axis amplitudes for M_2 and S_2, are 41% and 133% greater than the full barotropic estimates. For the M_2 constituent, the ellipse phase and orientation for the two estimates differ by about 70° . At mooring M6, the upper-ocean major axis amplitude of M_2 is smaller than that of the full barotropic estimate with eccentricity, orientation and especially phase being closely matched. For the S_2 constituent, the major axis amplitude for the upper ocean is 29%

greater than for the full barotropic case and orientation and phase are very different (129° , and 140° , respectively).

This analysis shows that separation of barotropic and baroclinic tidal currents is only useful where either full-depth ($M1_1$) or wide-range observations of the ocean interior are available. None of our other observations (i.e. 300kHz observations in the upper ∼50 m as available at moorings $M1_2$-$M1_6$) allow for a reliable separation. We thus proceed to discuss tidal currents without separation into barotropic and baroclinic components.

3.3.2.4 *Estimating wind-driven inertial currents in the surface mixed layer*

We used a damped slab model (Pollard and Millard 1970; D'Asaro 1985) to estimate the wind-driven inertial currents in the surface mixed layer (SML). This model provides the time evolution of the SML current vector for a given time series of vector wind stress, specified SML depth and a decay constant representing damping terms including dissipation and energy losses through internal wave radiation. The temporal resolution of the wind stress has a substantial influence on the generation of inertial currents. For mid-latitudes, D'Asaro (1985) found that the energy flux from wind to inertial motions is underestimated by ∼20% using 3-hourly wind input whereas for hourly wind input this error is only ∼2% . Thus, hourly output of wind velocity from ERA5 (**section 3.1.3**) is deemed adequate to generate an inertial response in the ocean. Changes in both amplitude and direction of the wind stress vector can excite or dampen resonant motions. We followed Andreas et al. (2010) to account for the effect of sea ice concentration on wind stress penetration into the ocean using concentration values from the ERA5 reanalysis at the grid points closest to each mooring site. Distances of the closest grid point are always less than 13 km. The damping time scale is usually taken to be in the range of 2 to 14 days (D'Asaro 1985). In an Arctic application, Martini et al. (2014) used a damping time scale of 3.5 days in the Beaufort Sea based on theoretical

considerations described by Alford (2001). To obtain results likely to be at the higher end of realistic inertial currents, we made computations using a mixed layer depth of 10 m and a decay time scale of 14 days. We expect that uncertainties in ERA5 winds due to the paucity of data constraints in the eastern Arctic may further contribute to uncertainties in predicted SML inertial currents.

3.3.2.5 *Modeling three dimensional tidal currents*

We used the Regional Ocean Modeling System (ROMS) version 3.7 (Haidvogel et al. 2000; Shchepetkin and McWilliams 2005) to study tidal currents and the differences in the behavior of semidiurnal constituents M_2 and S_2. ROMS is a hydrostatic 3-D primitive equation model using a terrain-following (sigma-level) coordinate system. The model was run on the Extreme Science and Engineering Discovery Environment (XSEDE) (Towns et al., 2014). Our model covers the Eastern Arctic region with 51 vertical levels on a horizontal grid with spacing of 2 km. The bathymetry was based on IBCAO version 3 (Jakobsson et al. 2012) and smoothed to a Beckmann and Haidvogel number (rx0) of 0.2 to reduce pressure gradient errors (Haidvogel and Beckmann 1993).

The model was forced at the open boundaries with both tidal currents and elevation values from the Arctic Ocean 5 km forward model (AODTM-5) developed by Padman and Erofeeva (2004). The initial conditions (stratification and background currents) were taken from a 4-km, 90-level ocean and sea ice Arctic Ocean simulation using the community ocean model MITgcm (Marshall et al. 1997; Losch et al. 2010). This Arctic simulation used hydrographic data from release 1 of the Arctic Subpolar gyre state Estimate, ASTE

(Nguyen et al. 2017). We used simulated 2014 mean-March and mean-September modeled fields, interpolated to our ROMS grid, to represent winter and summer conditions, respectively. We tested for errors associated

with interpolation and the ROMS grid structure by conducting no-forcing runs to ensure that the background conditions did not vary significantly from initial conditions over the course of a tidal run.

We ran multiple 20-day simulations, forced with M_2 and S_2 separately, to examine differences in behavior of the semidiurnal tides due to seasonal changes in stratification and circulation, and the maximum likely effect of adding sea ice to winter stratification. Ice was applied as a thin plate of land-fast ice at 100% concentration to add friction at the ocean surface.

3.4 RESULTS

3.4.1 *Current velocities*

Variability of hourly currents along the 125° E mooring array was large in both time and space (Fig. 3.2). At mooring 1893 on the shelf, speeds were high throughout the two years, with no dominant direction. Speeds varied with a roughly 2-week cycle and the depth of maximum current speed varied on an annual cycle, being shallowest in the summer period with no sea ice present. Further down the slope (moorings $M1_1$ and $M1_2$), velocities were generally eastward, consistent with these moorings being within the core of the ACBC (e.g. Pnyushkov et al. 2015). North of mooring $M1_2$, the directional coherence and average velocity decreased with increasing distance offshore (moorings $M1_3$ to $M1_6$). However, at the offshore moorings there were pronounced summertime velocity amplifications, especially in August to late October in 2014. These summer maxima became stronger with increasing distance offshore. The largest current speed in the offshore moorings exceeded 30 cm/s for a short period in October 2014 at mooring $M1_6$.

Rotary spectra of the depth-averaged (see Table 3.2 for depth ranges) velocities for each mooring time series show that, in general, the power

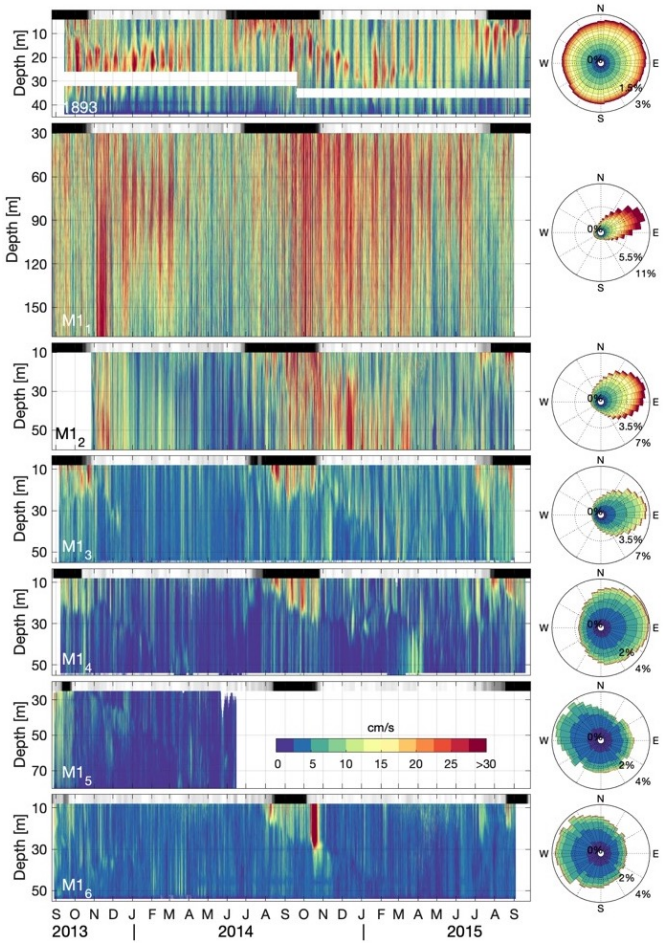

Figure 3.2: (Left column) Time-depth plots of observed currents speed at the mooring locations shown in Fig. 3.1. Gray shading at the top of the plots indicates sea-ice concentration (white= 100% , black= 0%). (Right column) The distribution of direction (the length of each 10° bin is proportional to the percentage of data within this bin) and amplitude (colors) of the observed currents.

in the clockwise component surpassed that of the counter-clockwise component (Fig. 3.3). These spectra were obtained from averaging of 50% overlapping windows of 1/3 the length of each time series; for a 2-year record, a spectrum represents oscillatory signals that remain stationary for ∼8 months. The preferred polarization of current ellipses is determined by the Earth's rotation (e.g. Gonella 1972). The highest energy density for each mooring is in the semidiurnal band, with distinct peaks centered at frequencies for the M_2, S_2, and N_2 constituents. Peak power is highest at M_2 for all moorings over the slope and shelf (onshore of, and including

Table 3.2: Tidal ellipse parameters for four constituents at all moorings across the array. Values are averaged over time and depth (see last columns for depth ranges and bottom depth). Italic font for major axis amplitudes indicates amplitudes at or below 95% confidence level. For Eccentricity, italic font indicates that major axis amplitude and/or minor axis amplitude are at or below 95% confidence level.

	Major axis				Eccentricity				Orientation ° from East				Phase ° from Greenwich				Depth range [m]	Bottom depth [m]
	M_2	S_2*	K_1*	O_1	M_2	S_2*	K_1*	O_1	M_2	S_2*	K_1*	O_1	M_2	S_2*	K_1*	O_1		
1893	6.7	4.1	1.8	*1.4*	1.2	1.3	*2.3*	*2.4*	49	62	113	106	267	270	206	215	4-44	50
$M1_1$	4.3	2.6	*1.5*	*1.4*	1.4	1.6	*2.8*	*3.5*	97	94	75	82	254	249	136	172	30-230	250
$M1_2$	5.3	3.8	1.3	*1*	1.4	1.5	*3.6*	*3.5*	86	101	95	92	251	293	151	166	10-60	790
$M1_3$	2.9	2.6	*0.6*	*0.6*	1.2	1.2	*3.3*	*3.5*	63	102	93	89	242	226	179	177	8-48	1850
$M1_4$	2.2	2.3	*0.5*	*0.6*	1.4	1.3	*3.4*	*3.3*	83	76	95	84	206	229	177	191	8-50	2720
$M1_5$	1.2	2.1	*0.2*	*0.2*	*2.1*	1.3	*3.2*	*3.1*	96	132	87	91	207	285	183	171	25-82	3440
$M1_6$	1.5	2.1	*0.5*	*0.5*	*2.1*	1.3	*3.3*	*3.4*	91	106	89	89	204	240	176	187	8-46	3900

mooring $M1_4$); however, the greatest power at the offshore moorings $M1_5$ and $M1_6$ is at S_2. The peaks become broader in frequency with increasing distance offshore, indicative of increasing baroclinicity (e.g. Munk 1997; Kulikov 2004). We attribute the lack of distinct power peaks at the inertial frequency (located between M_2 and S_2

frequencies at all moorings; see Table 3.1) to time variability of wind events leading to a lack of phase coherence of wind-forced near-inertial oscillations throughout each entire mooring record. For the dominant diurnal constituents, K_1 and O_1, peaks are only distinguishable at the inshore moorings 1893 and $M1_1$. A little further down the slope, at $M1_2$, only K_1 is identifiable (Fig. 3.3). In further analyses, we focus on the semidiurnal band current (SBC) variability.

3.4.2 *SBCs and total tidal currents*

Averaged over time and depth, the mean speed of SBCs is 53% of the mean measured current speed across the array (Table 3.3). Values at the individual mooring sites range from 34% for mooring $M1_1$, which is predominantly governed by the strong flow of the ACBC, to 71% at mooring 1893 on the shelf, where almost no background flow is present (Fig. 3.2).

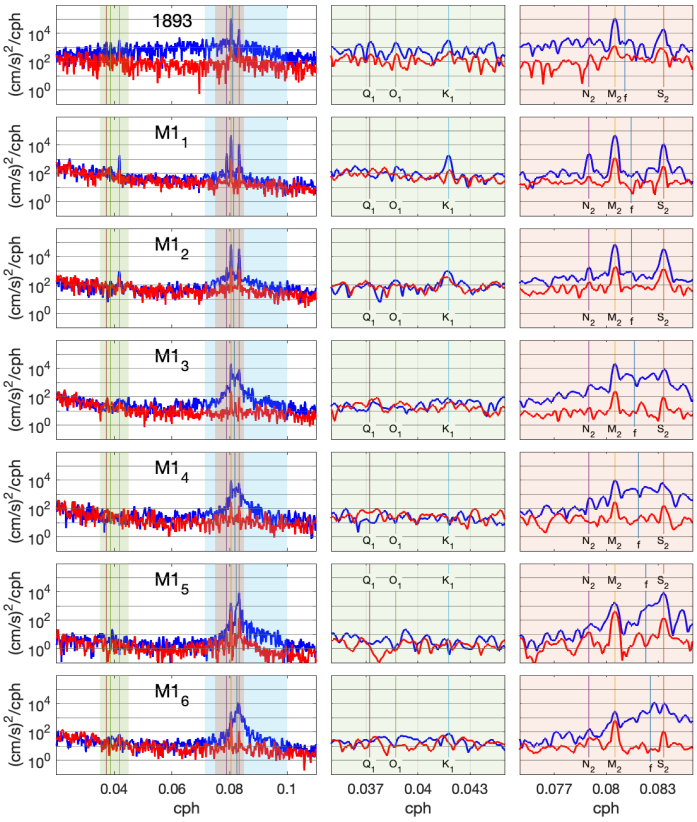

Figure 3.3: Left column: Rotary spectra (using Welch's method with window length of 1/3 of the length of the time series and 50% overlap) of depth-averaged velocities. Blue indicates the clockwise component, red the counter-clockwise component. Middle and right columns are zoomed-in on diurnal (green shading) and semidiurnal (red shading) frequency bands, respectively. Colored lines and labels mark the frequencies of the dominant tidal constituents as well as local inertial frequency (f). Blue shading in the left column indicates the frequency band (10-14 h period) used for the band-pass filtered semidiurnal band currents.

SBCs exhibit substantial variability with depth and on a broad range of time scales including seasonal and fortnightly frequencies (Fig. 3.4, left column). The strongest SBCs are almost always in the upper 30 m in summer 2014 and reach peak velocities of 49 cm/s in October at the offshore mooring $M1_6$. The summer signals follow a pattern of progressive deepening over the course of the ice-free season; strong currents are confined to the upper limit of observations ($\sim$10 m) at the onset of ice melt (June-July), then gradually deepen to about 30 m by late October. This

pattern is typical of the impact of wind forcing on seasonally ice-free seas (e.g. Rainville and Woodgate 2009), where rapid sea ice melting in early summer creates a shallow, strongly-stratified SML that deepens by mixing through summer once the primary source of surface buoyancy is removed.

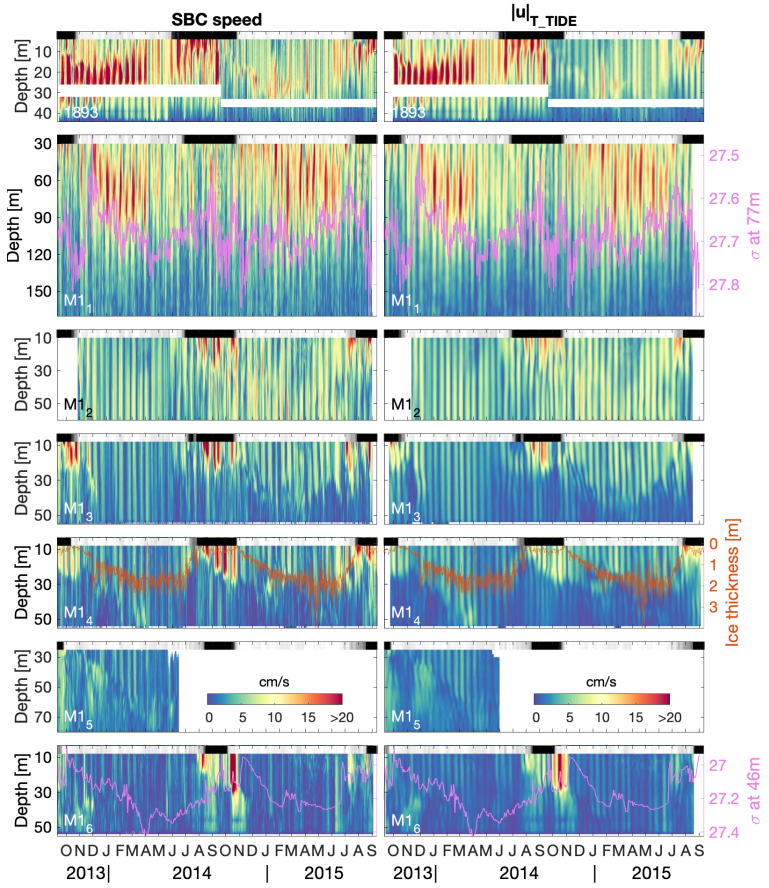

Figure 3.4: Left column: 10-14 h band pass filtered raw speed, representing near-inertial currents (SBCs). Right column: Total tidal current speed as derived from T_TIDE analysis ($|\mathbf{u}|_{\mathrm{T\_TIDE}}$). The apparent fortnightly oscillation of the signal stems from the superposition of the constituent pairs S_2* and M_2, and K_1* and O_1.

The prominent higher-frequency variability in SBCs speed often has a period of about two weeks, consistent with expectations from the spring-neap modulation of the dominant semidiurnal tidal constituents M_2 and S_2 identified in spectra (Fig. 3.3). However, the modulation period can vary, in some depth ranges for some moorings, in the range ∼1-4 weeks.

We attribute this variability to two factors; the addition of wind-forced inertial currents with timescales set by passage of weather systems, and broadening of tidal spectral peaks (Fig. 3.3) by the sensitivity of baroclinic tides to changing ocean background state.

Based on the presence of semidiurnal and diurnal tidal peaks in spectra (Fig. 3.3) and the roughly fortnightly (apparently spring-neap) modulation of SBCs, we carried out tidal analysis as described in **section 3.2.2**. Plots of total tidal current speed ($|\mathbf{u}|_{\text{T\_TIDE}}$, Fig. 3.4, right column) are similar to those for SBC speeds (Fig. 3.4, left column). This similarity is consistent with tidal currents providing a significant fraction of SBC energy. However, T_TIDE tidal analysis on one-month data segments may also be influenced by strong inertial currents, as we demonstrate in the following section.

3.4.3 *Influence of inertial currents on harmonic tidal analysis*

We demonstrate the potential influence of inertial currents on T_TIDE analysis using time series of simulated wind-driven inertial currents from the damped-slab model described in **section 3.2.4**. Time series of inertial currents at the $M1_6$ mooring location (Fig. 3.5, top) were evaluated for SML thicknesses of 10 m and 50 m, roughly representing summer and winter conditions, respectively. For a 10 m SML, simulated inertial currents frequently exceed 20 cm/s in every season, reaching a maximum of 36 cm/s in October 2014. This maximum is similar to maximum measured currents (Fig. 3.2) and SBCs (Fig. 3.4). Modeled values depend on the choice of the damping time scale, which we have taken to be 14 days to maximize the inertial response of the SML; however sensitivity to the damping scale is weak over a range of several days.

We applied the T_TIDE analysis described in **section 3.2.2** to the slab-model output to produce $|\mathbf{u}|_{\text{T\_TIDE}}$, and the associated tidal ellipse parameters. The T_TIDE analysis assigns a substantial portion of the near-inertial

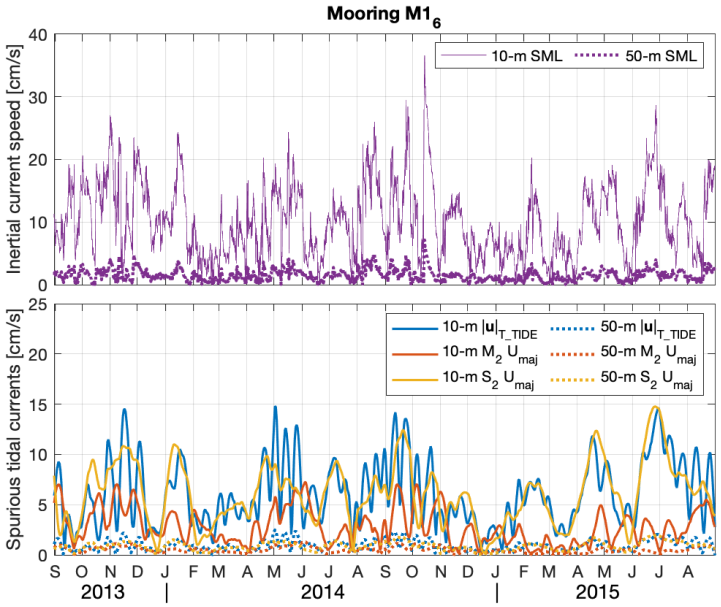

Figure 3.5: Top: Simulated inertial currents for idealized SML depths of 10 m and 50 m at mooring M16. Bottom: Output of T_TIDE tidal analysis from the purely inertial time series above.

energy to S_2* (maximum of 15 cm/s) and M_2 (maximum of 7 cm/s). We attribute the larger amplitude of the S_2* term, relative to M_2, to the proximity of f to the frequency of S_2. The time series of $|\mathbf{u}|_{\text{T\_TIDE}}$ has maximum values of about 15 cm/s, and is modulated at time scales of roughly two weeks, caused by the superposition of the spurious M_2 and S_2* constituents.

Simulated inertial currents are much weaker for an idealized 50-m thick SML, seldom exceeding 5 cm/s. Values of $|\mathbf{u}|_{\text{T\_TIDE}}$ average 1 cm/s with a maximum of 2.5 cm/s.

We conclude that, for shallow mixed layers during summers, T_TIDE analysis of one-month time intervals of data is substantially affected by wind-forced near-inertial motion, placing strong constraints on our analysis of tidal currents. During winter, however, when the SML is deep and the high-concentration ice cover damps excitation of inertial oscillations, inertial influence on tidal analysis is small and we expect that T_TIDE

results represent tides. This is supported by the clear fortnightly oscillations in the SBCs (Fig. 3.4, left), which are expected from spring-neap tidal cycles but inconsistent with the irregular weather-band forcing of inertial waves.

3.4.4 *Tidal properties*

With the caveat that strong wind-forced near-inertial oscillations may be misrepresented as tides in T_TIDE analysis on short records, we use time- and depth-dependent variability of tidal ellipses along the 125° E transect (Fig. 3.6) to identify possible contributions of tides to SBC variability. The ratio of major to minor axis amplitudes ($U_{maj}/|\ U_{min}|$) controls the eccentricity of the tidal ellipses, while the sign of the minor axis amplitude determines the direction of rotation. Note that the sampled depth range varies between moorings.

For both semidiurnal constituents, ellipses are nearly circular at all moorings, with eccentricities averaging 1.6 and 1.3 for all moorings for M_2 and S_2* , respectively. The ellipses for the diurnal constituents are relatively rectilinear with eccentricities averaging 3.1 and 3.2 for K_1* and O_1, respectively. However, major axis amplitudes for diurnal constituents are very small ($\leq$

1.5 cm/s except for K_1* at 1893), and mostly below the 95% confidence level (see Table 3.2). Orientation and phases vary widely between the moorings, but tend to behave similarly for frequencies that are close together (i.e. for the pairs M_2 and S_2* ,

and K_1* and O_1). There is greater similarity between the diurnal constituents K_1* and O_1, with differences between each other at all moorings averaging 2° for orientation and 10° for phases, compared to 15° and 23° , respectively, between the semidiurnals.

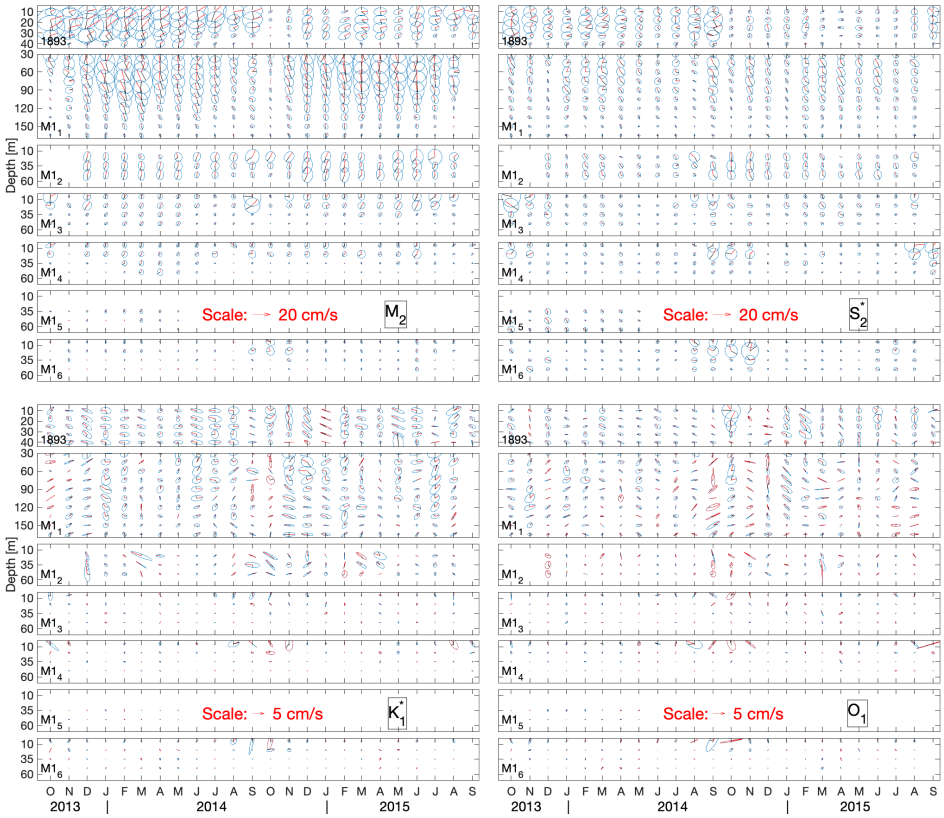

Figure 3.6: Tidal ellipses from T_TIDE for the leading semidiurnal frequencies (M_2 and S_2* , top) and the diurnal constituents K_1* and O_1 (bottom). Ellipses are interpolated on a monthly grid with 15m vertical resolution. Blue ellipses show clockwise rotation, red ellipses counter-clockwise rotation. Red lines indicate ellipse orientation and black lines indicate Greenwich phase (counter-clockwise from the right). Note the different scales for semidiurnal and diurnal constituents.

3.4.4.1 *Seasonal and spatial variability of semidiurnal tides*

Based on their analysis of earlier data from the location of mooring $M1_4$, Pnyushkov and Polyakov (2012) proposed that the upper-ocean baroclinic tidal energy in deep water in the eastern EB varies seasonally. Our analysis confirm this seasonal variability of M_2 and S_2* ellipses from T_TIDE (Fig. 3.6). Major axis amplitudes of M_2 and S_2* show two patterns of seasonality at almost all moorings across the array: wintertime deepening of current maxima (mostly M_2), and summertime surface amplification (especially for S_2*) (Fig. 3.7). We reiterate, however, that strong wind-forced inertial

oscillations, especially for shallow SMLs in early summer, may contaminate T_TIDE estimates of semidiurnal current ellipse properties (**section 4.3**).

The winter deepening pattern of M_2 tidal currents from T_TIDE analysis is most pronounced on the upper slope (mooring $M1_1$) where data are available throughout most of the water column. Deepening started with the freeze-up in late October and reached maximum depth in March for both winters (2013-2014 and 2014-2015), with M_2 major axis amplitudes reaching maxima of about 14 cm/s at around 70 m depth. These values are much greater than the values obtained by T_TIDE analysis of purely wind-forced inertial currents for deep SMLs (Fig. 3.5), indicating that the variability is truly tidal. The subsequent shoaling was gradual during spring 2014 with an intermittent deepening in May-June. In spring 2015, the shoaling progressed more quickly and happened almost entirely between mid-June and mid-July. At the peak of the shoaling in summer, the maximum appears to be above the 30 m depth limit of our observations at mooring $M1_1$. On the shelf, at mooring 1893, a similar seasonality with generally strong tidal currents occurred during the first deployment period (2013-2014). During the second deployment (2014-2015), seasonality was still present, but measured tidal amplitudes were generally much weaker. We are presently unable to explain this abrupt change. At the $M1_2$ mooring 11 km down the slope from $M1_1$, the general shape of winter deepening resembles that at mooring $M1_1$, but major axis amplitudes are much lower ($\sim$6 cm/s for the first winter and $\sim$10 cm/s for the second) and the deepening appears to be shallower, although below the observational limit of 60 m. Further offshore, the pattern becomes less visible with increased distance from the slope and the depth range of the deepening continues to decrease (reaching only $\sim$30 m depth during the second winter at mooring $M1_4$).

We propose that this pattern of variability is related to seasonal changes of stratification. At moorings $M1_1$ and $M1_6$, hydrographic records are

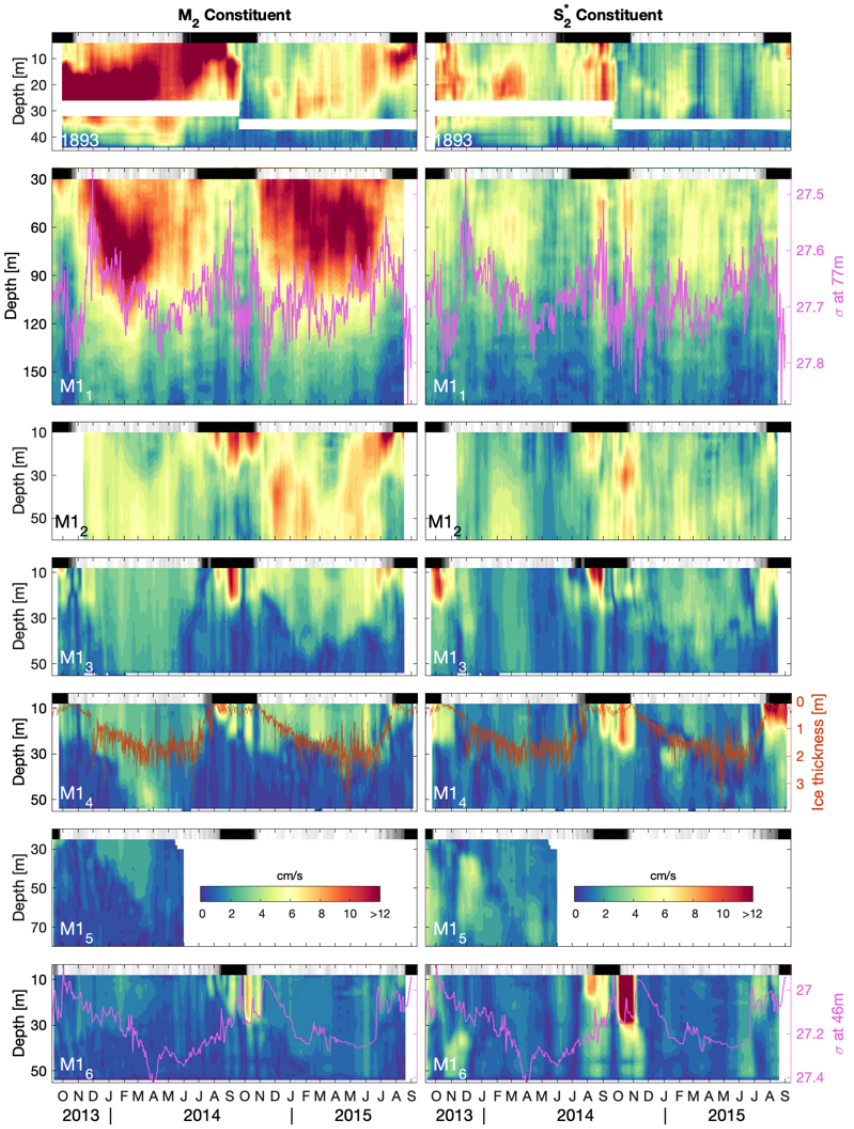

Figure 3.7: Time-depth plots of major axis amplitudes of the M_2 (left) and S_2* (right) constituents at the moorings across the continental slope. Gray shading at the top of the plots indicates sea-ice concentration (white= 100% , black=0%). Pink lines show detrended potential density (σ) at the shallowest available level (for moorings at which this level is above the deepest ADCP observations) and the red line in the $M1_4$ panel shows sea-ice thickness from upward looking sonar observations (one-day low-pass filtered).

available within the ADCP depth range, at 77 m for $M1_1$ and 46 m for $M1_6$. Density time series show a seasonal cycle with increasing density over the course of the winter and decreasing again in spring, which is in phase with the deepening and shoaling of elevated M_2 tidal currents. The limited hydrographic sampling and two-year lengths of the time series restrict our ability to quantitatively determine the relationship between stratification and tidal currents. Nonetheless, the observed seasonal cycle of density qualitatively supports a connection between the tidal amplitudes and stratification as has been shown, for example, by Janout and Lenn (2014) for a site on the Laptev Sea shelf.

Summertime surface amplification is observed at almost all moorings for both constituents (the only exceptions being M_2 at moorings 1893 and $M1_1$), and is most likely dominated by wind-driven inertial currents that are erroneously attributed to tidal constituents. S_2* reaches its greatest major axis amplitude of 18 cm/s at the northernmost $M1_6$ mooring location during October 2014, which is close to the maximum of 15 cm/s that T_TIDE produces from purely inertial input for this mooring (compare Fig. 3.7 and Fig. 3.5).

3.5 DISCUSSION

3.5.1 *Pronounced seasonality of semidiurnal currents*

Our analyses show a clear seasonal cycle of SBCs and $|\mathbf{u}|_{\text{T\_TIDE}}$. We expect that the primary controls on the time and depth distributions of these currents are stratification and sea ice, the latter being a strong control on the generation of wind-driven inertial oscillations in the SML and the damping of baroclinic tides.

Upper ocean hydrography is directly dependent on the seasonal cycle of sea ice: brine rejection during sea-ice formation leads to an increase

of upper ocean density and convection, which causes a deepening of the pycnocline. Conversely, springtime ice melt introduces buoyant freshwater and re-stratifies the upper ocean which is associated with a shoaling of the pycnocline. The vertical extent of measured SBCs (Fig. 3.4) and total tidal currents (Fig. 3.7) follow the winter deepening and subsequent springtime shoaling of the pycnocline. We argue that during these times and in these depths, the influence of wind-driven inertial currents is small and the signals are indeed of tidal origin. Baroclinic tidal currents are tightly linked to vertical density gradients and thus follows the seasonal evolution of the pycnocline (e.g. Janout and Lenn 2014).

Since the temporal variability of amplitudes of M_2 and S_2* (Fig. 3.7) represent a combination of changing baroclinic tide forcing, propagation and damping mechanisms as well as T_TIDE misrepresentation of wind-forced inertial motions as tides (**section 4.3**), we employ a baroclinic tidal model (see **section 3.2.5** for model description) to gain insight into the properties of tidal currents in the eastern EB. The model confirms that most near-surface tidal kinetic energy is concentrated on the shelf and at the continental slope (Fig. 3.8). The modeled near-surface fields of baroclinic major axis amplitudes (U_{maj}) are spatially patchy, highlighting the dependence of baroclinic tidal currents on topographical features as well as on background stratification. Major upper-ocean tidal hotspots in the region are the shelf areas around 115° E and 140° E with major axis amplitudes of M_2 exceeding 15 cm/s for both summer and winter stratification, although they are stronger in summer. Over the slope and deep basin, summer stratification yields slightly higher tidal amplitudes compared to winter (Fig. 3.8, top and middle). While most tidal energy is concentrated at the continental slope, the model qualitatively produces moderately enhanced S_2 tidal currents in the deep basin (as far as mooring $M1_5$) under summertime stratification (Fig. 3.8, top). Although major axis amplitudes are far smaller than suggested by tidal analysis (barely

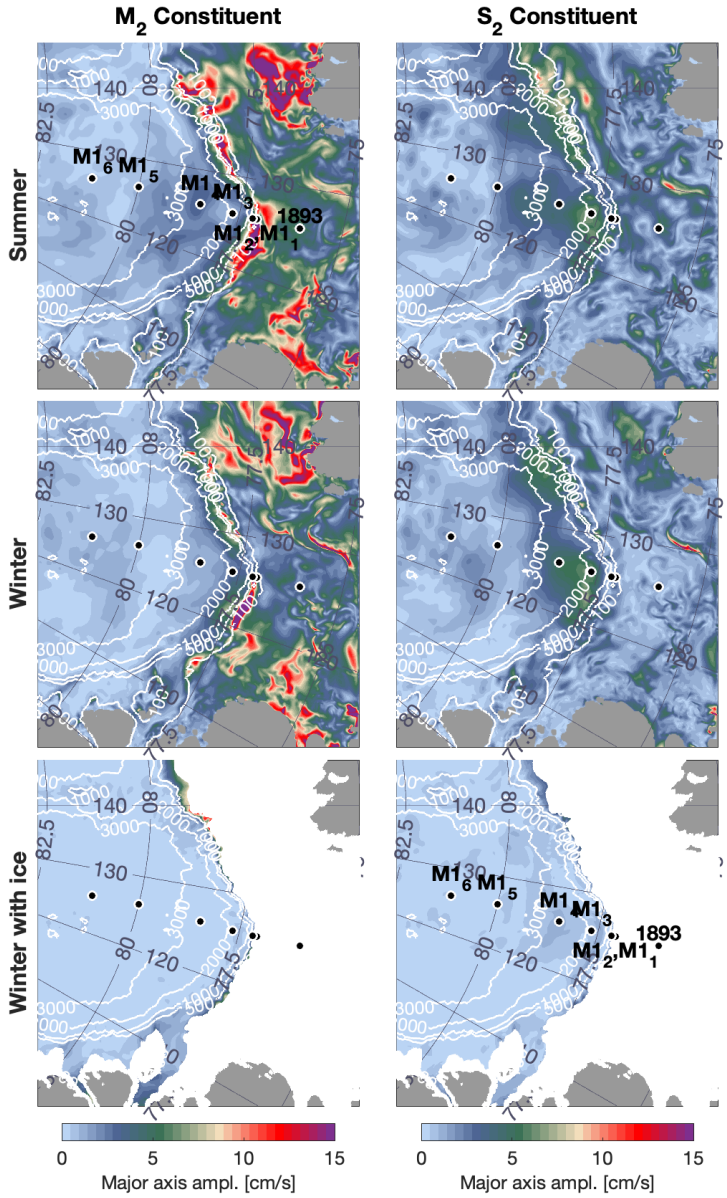

Figure 3.8: Regional maps of the eastern EB showing simulated surface baroclinic tidal amplitudes of M_2 (left) and S_2 (right) for different realistic background conditions (see **section 3.2.5** for model description): Summer stratification (top), winter stratification without ice (middle) and winter stratification with landfast ice (bottom). For the latter, values for bottom depths shallower than 150 m are omitted because much of the apparent baroclinic signal is associated with the frictional boundary layer under ice in the presence of strong barotropic currents.

reaching 5 cm/s offshore of the slope as opposed to ∼18cm/s). Simulated tidal energy fluxes show that the source regions of baroclinic tidal currents are at the steep continental slope. While the M_2 internal tide is confined by critical latitude effects and only propagates eastward along the slope, the S_2 internal tidal tide is shown to propagate offshore into the deep basin (Fig. 3.9). This demonstrates the possible pathway for enhanced tidal activity in the central basin.

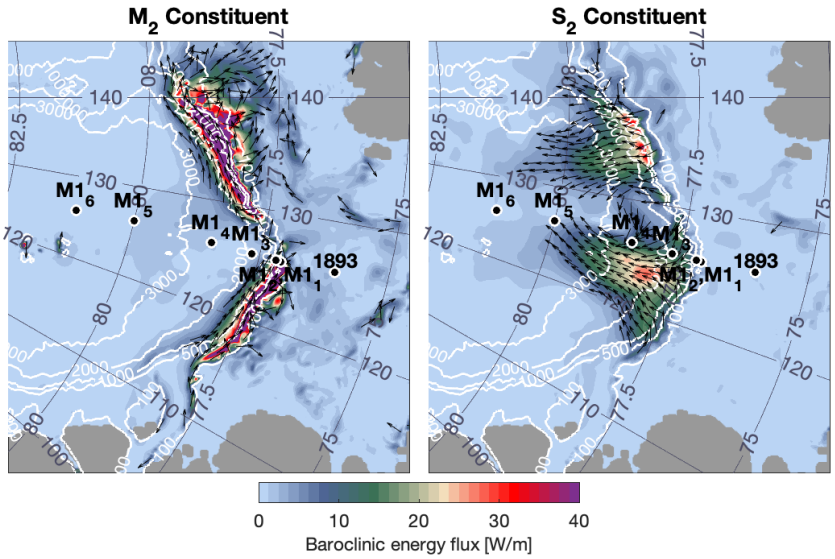

Figure 3.9: Top: Regional maps of the eastern EB showing vertically integrated horizontal baroclinic energy flux for simulated tidal currents of M_2 (left) and S_2 (right) constituents for summer stratification without sea ice. Colors indicate the amplitude, arrows show the direction of flux higher than 10 W/m. Dots indicate the locations of the moorings across the continental slope.

During periods of high ice concentration in winter, SBCs and $|\mathbf{u}|_{\text{T\_TIDE}}$ often show subsurface maxima, especially on the shelf (mooring 1893) and upper slope (moorings $M1_1$ and $M1_2$, Fig. 3.4). We attribute these patterns to the frictional effects of high-concentration ice cover (Morison et al. 1985; D'Asaro and Morison 1992). In our simulations with winter stratification and a land-fast ice cover providing a frictional surface, near-surface tidal currents are reduced over deep water (Fig. 3.8, bottom), with major axis amplitudes for M_2 being negligible and values for S_2 being less than 2

cm/s. We do not show baroclinic tides for water less than 150 m deep for the winter case with ice cover because much of the apparent baroclinic signal is associated with the frictional boundary layer in the presence of strong barotropic currents.

We conclude that changes in both ocean stratification and ice cover can produce seasonal cycles in baroclinic tides over the deep-water section of our mooring array, but that modeled amplitudes are small compared with measured values. At this time we do not know if this discrepancy is associated with deficiencies in our tide models or with underestimating the contribution of wind-forced inertial currents to tidal analysis with T_TIDE.

3.5.2 *Limitations of harmonic tidal analysis*

As we previously demonstrated (**section 4.3**, and Fig. 3.5), the proximity of the local inertial frequency to the semidiurnal M_2 and S_2 frequencies (Table 3.1) prevents a clean analytical separation of the frequencies within a 30-day window. Therefore, we cannot use tidal analysis to unambiguously separate wind-driven inertial variability from time-dependent variability of baroclinic tides.

We conducted further tests in which we applied seasonal tidal analysis with a 90-day window to the simulated inertial time series. This window is sufficiently long to formally separate inertial oscillations from tidal frequencies; see Table 3.1. Even in this scenario, some energy was erroneously attributed to tidal constituents, arguably due to the broad spread of inertial energy over the semi-see spectra in Fig. 3.3).

These tests highlight the limitations of classical harmonic tidal analysis for the study of baroclinic tidal currents within the upper Arctic Ocean, where inertial currents from wind input may be substantial.

Table 3.3: Averages of raw and SBC speed (| Raw| and | SBC| , respectively) and their ratio over the whole time and depth domain (same as in Table 3.2)

All time	|Raw| [cm/s]	|SBC| [cm/s]	|SBC| / |Raw| [%]
1893	12.35	8.77	71
$M1_1$	16.14	5.36	33
$M1_2$	12.16	6.23	51
$M1_3$	9.19	4.54	49
$M1_4$	8.41	4.12	49
$M1_5$	4.25	2.71	64
$M1_6$	6.64	3.21	48

3.6 SUMMARY & OUTLOOK

We have conducted extensive analyses of two-year time series of upper-ocean currents from moorings along 125°E from the continental shelf to the deep basin in the eastern Arctic. Combined with a slab model of surface mixed layer (SML) near-inertial response to realistic wind stress variability and a three-dimensional baroclinic tide model, these analysis provides insight into the variability of major sources of upper ocean kinetic energy as sea ice conditions and regional hydrography change through the year. The main findings of this study are as follows:

- Semidiurnal-band currents (SBCs, 10-14 h period) are a major contributor to current dynamics in the eastern EB region, with mean SBC speeds accounting for 33-71% of mean total current speed (Table 3.3). Tidal currents (dominated by the semidiurnal M_2 and S_2* constituents) are strongest over the upper slope and decrease toward the deep basin.

- During ice-free summer months, SBCs are strongly amplified in the upper ∼30 m, reaching amplitudes in excess of 40 cm/s far offshore in the eastern EB (Fig. 3.4). Between summer periods the depth of

strong SBCs varies, following the expected winter deepening and spring shoaling of the pycnocline.

- Models of inertial currents in the SML and baroclinic tide generation and propagation suggest that, while the wintertime SBCs appear to be predominantly of tidal origin, observed large near-surface SBCs in summer in the deep basin are caused primarily by wind forcing of inertial oscillations. However, we predict some contribution from baroclinic tides generated along the upper continental slope (Figs. 3.8 and 3.9). Critical latitude effects result in trapping of M_2 baroclinic tides to the slope; however, S_2 tides can radiate northwards into deep water.

- The close proximity of the inertial period to periods of energetic semidiurnal tides (Table 3.1), and the expected variability of inertial and tidal current phases and amplitudes, precludes the empirical separation of these two signals.

The eastern Arctic Ocean is presently experiencing rapid changes in sea ice and ocean states, including a long-duration summer period free of high-concentration and thick sea ice, and reduced upper-ocean stratification. We speculate that these trends will lead to substantial changes in semidiurnal-band kinetic energy that, in turn, may contribute to the ongoing changes through ocean stress on the sea ice and shear-induced mixing. The long-term changes in SBCs, and the effect on the ocean and sea ice, will depend on the individual and coupled contributions of baroclinic tides and wind-forced inertial oscillations. However, as we have shown, the time-dependence of these signals cannot be separated through purely empirical analysis of mooring data. Instead, we propose that further progress will require dedicated modeling studies that can separate the contributions from both sources of semidiurnal-band currents in a changing Arctic.

3.7 ACKNOWLEDGMENTS

The ship-based oceanographic observations in the eastern EB and Laptev Sea were conducted under the working frame of the NABOS project with support from NSF (grant AON-1203473). Analyses presented in this paper are supported by NSF grants 1249182 (TB, IP, LP, AP), 1708427 (TB, IP, AP, SD), 1708424 (LP), 1708289 (AN) and 1722729 (JH). TB was supported in part by a UAF Global Change Student Research Grant award with funds from the Cooperative Institute for Alaska Research. IF received support from the Research Council of Norway through the project 294396. MJ acknowledges financial support from the German Federal Ministry of Education and Research (BMBF grant 03G0833)This work used the Extreme Science and Engineering Discovery Environment (XSEDE), which is supported by National Science Foundation grant ACI-1548562. In particular, it used the Comet system at the San Diego Supercomputing Center (SDSC) through allocation TG-DPP180004.

3.8 APPENDIX: COMPARISON BETWEEN MODELED AND OBSERVED BAROTROPIC TIDAL CURRENTS

Barotropic tidal models are commonly used to investigate the spatial properties of tidal currents without including the much more complex baroclinic component. Here we compare the solutions of the barotropic models by Kowalik and Proshutinsky (∗ Kowalik and Proshutinsky 1994) and Padman and Erofeeva (2004) with our observations at the $M1_1$, M3 and M6 mooring locations (the full depth barotropic estimates from **Table A1 and Fig. A1**). The model solutions are taken from the respective grid point closest to each mooring location. The K&P model represents amplitudes at

Table A3.1: Barotropic tidal ellipse parameters for five constituents derived from currents averaged vertically over different depth ranges (see second to last row for ranges), as described in **section 3.2.3**. These values are used to create the ellipses in Fig. A3.1.

		$M1_1$	$M1_1(top)$	$M3$	$M3(top)$	$M6$	$M6(top)$
Major axis amplitude [cm/s]	M_2	3.55	8.08	1.08	1.53	0.85	0.37
	S_2	1.98	4.51	0.88	2.05	0.42	0.54
	N_2	0.85	1.69	0.2	0.31	0.15	0.11
	K_1	0.8	1.43	0.07	0.14	0.17	0.22
	O_1	0.39	0.8	0.03	0.09	0.08	0.04
Minor axis amplitude [cm/s]	M_2	-2.55	-6.76	0.68	0.16	-0.05	-0.07
	S_2	-1.35	-3.64	-0.29	-1.57	-0.08	-0.32
	N_2	-0.6	-1.44	0.16	-0.02	-0.01	0
	K_1	-0.6	-0.81	-0.02	-0.02	-0.04	-0.04
	O_1	-0.29	-0.65	0	-0.03	-0.01	-0.03
Orientation [° from East]	M_2	106	90	165	99	177	159
	S_2	113	104	13	3	178	49
	N_2	96	93	119	105	174	117
	K_1	24	35	137	150	144	102
	O_1	179	13	24	75	160	61
Phase [° from Greenwich]	M_2	270	276	307	235	212	208
	S_2	296	315	216	215	269	130
	N_2	260	262	230	204	189	136
	K_1	109	91	147	134	44	53
	O_1	292	99	350	218	14	188
Depth range [m]		30-230	30-65	200-450	10-60	200-450	10-60
Bottom depth [m]		250		1335		2710	

the $M1_1$ mooring location better than the P& E model (differences between model and observations averaged over all constituents are 1.3 cm/s for P& E and 0.5 cm/s for K&P, Fig. A3.2). Over the slope, tidal amplitudes are highly sensitive to local water depth; even small inaccuracies of topography used in the model may result in the observed differences. The orientation of the tidal ellipses at $M1_1$ is also generally better captured by K&P, while for phases the differences in model performance are small. At M3, amplitudes are generally much smaller, but K&P almost perfectly captures M_2 (differences in major axis, minor axis, orientation and phase are 0.12 cm/s, 0.08 cm/s, 10° and 34° , respectively) and S_2 (with difference in the rotation is 37°). At the same mooring, P& E underestimate the amplitudes of M_2 and S_2, with differences of 0.31 cm/s (∼29%) and 0.55 cm/s (∼62%), respectively. Furthermore, phases and orientation are off by about 90° .

Note that both models predict counter-clockwise rotating currents for M_2 and S_2 while observations show that the latter is clockwise polarized. At the M6 mooring location, the amplitude of M_2 is again best captured by K&P (difference 0.04 cm/s), but P& E values are reasonably close with a difference of 0.2 cm/s. Interestingly, in terms of orientation and phase, the models agree better with each-other than with the observations. For the S_2 constituent, on the other hand, model predictions look rather different. While K&P capture the amplitude very well (difference of 0.04 cm/s), orientation and phase are off by 55° and 27° respectively. The model of P& E underestimates the amplitude by 39% but orientation and phase are off by only 21° and 18° , respectively. The polarization of K&P opposes the observations at M_2 and S_2, however, since the trajectories are almost linear (very eccentric), the polarization becomes physically less important and can easily be misinterpreted.

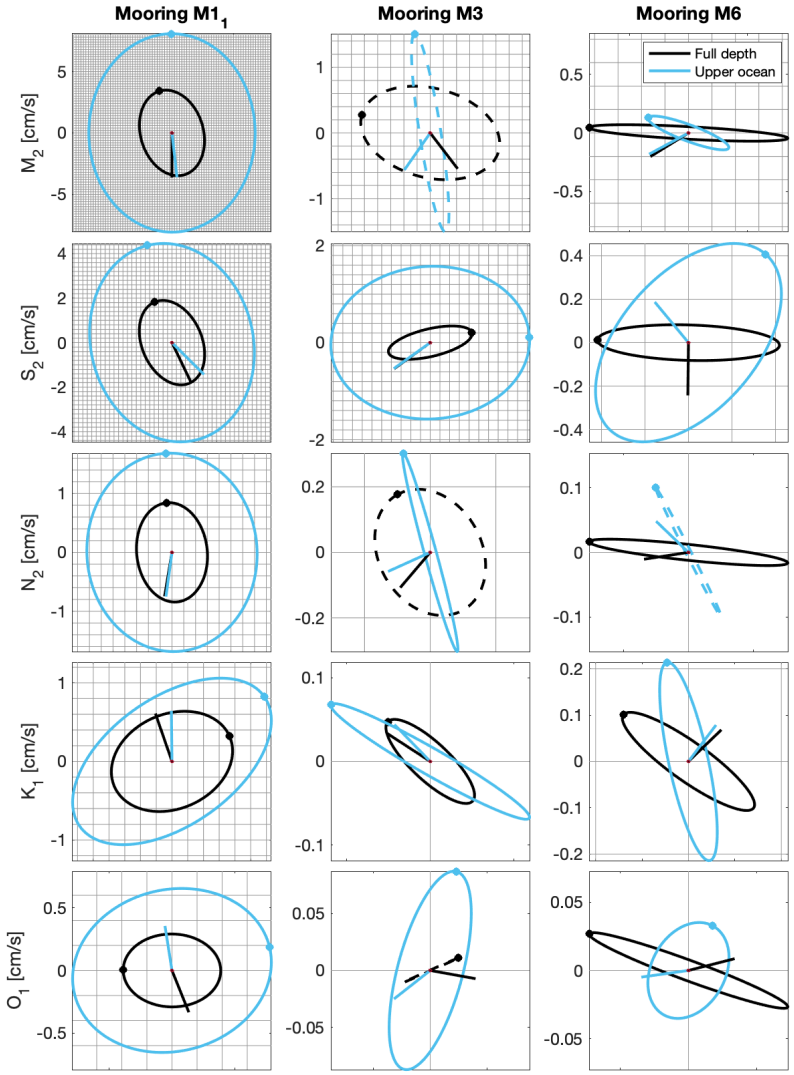

Figure A3.1: Barotropic tidal ellipses from full-depth observations (black) and "pseudo-barotropic" ellipses using only the upper 40m of observations at each mooring to compute barotropic ellipses (blue) for five constituents at three mooring locations ($M1_1$, M3 and M6). Dots on the ellipses denote the orientation; solid (dashed) lines mark (counter-) clockwise rotation. Lines around the origin of each plot indicate Greenwich phases (degrees counter-clockwise from the right). Gridlines are equally spaced (0.2 cm/s) in all plots.

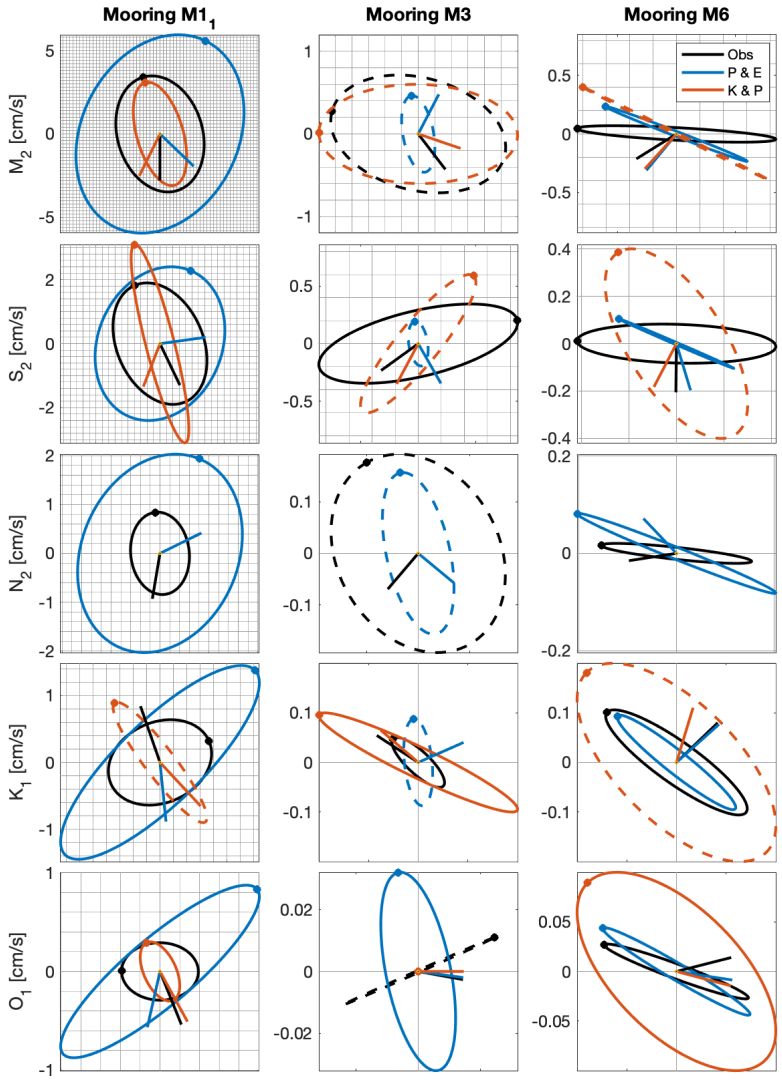

Figure A3.2: Barotropic tidal ellipses from observations (black) and the models of Padman and Erofeeva (P& E, blue) and Kowalik and Proshutinsky (K&P, orange) for five constituents at three mooring locations (ellipses are drawn as in Fig. A3.1).

3.9 REFERENCES

Aagaard, K., 1989: A synthesis of the Arctic Ocean circulation. Rapp. P.-v. Rcun. Cons. int. Explor. Mer, 188, 11–22, doi:10.4095/126774.

Alford, M. H., and M. H. Alford, 2001: Internal Swell Generation: The Spatial Distribution of Energy Flux from the Wind to Mixed Layer Near-Inertial Motions. J. Phys. Oceanogr., 31, 2359–2368, doi:10.1175/1520-0485(2001)031<2359:ISGTSD>2.0.CO;2.

Andreas, E. L., T. W. Horst, A. A. Grachev, P. O. G. Persson, C. W. Fairall, P. S. Guest, and R. E. Jordan, 2010: Parametrizing turbulent exchange over summer sea ice and the marginal ice zone. Quarterly Journal of the Royal Meteorological Society, 136, 927–943, doi:10.1002/qj.618.

Carmack, E., and Coauthors, 2015: Toward Quantifying the Increasing Role of Oceanic Heat in Sea Ice Loss in the New Arctic. Bull. Amer. Meteor. Soc, 96, 2079–2105, doi:10.1175/BAMS-D-13-00177.1.

Coachman, L. K., and C. A. Barnes, 1963: The Movement of Atlantic Water in the Arctic Ocean. ARCTIC, 16, 8–16, doi:10.14430/arctic3517.

Cole, S. T., J. M. Toole, L. Rainville, and C. M. Lee, 2018: Internal Waves in the Arctic: Influence of Ice Concentration, Ice Roughness, and Surface Layer Stratification. J. Geophys. Res. Oceans, 123, 5571–5586, doi:10.1029/2018JC014096.

Copernicus Climate Change Service, 2017: ERA5: Fifth generation of ECMWF atmospheric reanalyses of the global climate. https://cds.climate.copernicus.eu/cdsapp# !/home.

D'Asaro, E. A., 1985: The Energy Flux from the Wind to Near-Inertial Motions in the Surface Mixed Layer. J. Phys. Oceanogr, 15, 1043–1059, doi:10.1175/1520-0485(1985)015<1043:TEFFTW>2.0.CO;2.

D'Asaro, E. A., and J. H. Morison, 1992: Internal waves and mixing in the Arctic Ocean. Deep Sea Research Part A. Oceanographic Research Papers, 39, S459–S484, doi:10.1016/S0198-0149(06)80016-6.

Danielson, S., and Z. Kowalik, 2005: Tidal currents in the St. Lawrence Island region. J. Geophys. Res. Oceans, 110, 153, doi:10.1029/2004JC002463.

Dosser, H. V., and L. Rainville, 2016: Dynamics of the Changing Near-Inertial Internal Wave Field in the Arctic Ocean. JPO, doi:10.1175/JPO-D-15-0056.1.

Falahat, S., and J. Nycander, 2015: On the Generation of Bottom-Trapped Internal Tides. J. Phys. Oceanogr., 45, 526–545, doi:10.1175/JPO-D-14-0081.1.

Fer, I., 2014: Near-Inertial Mixing in the Central Arctic Ocean. J. Phys. Oceanogr, 44, 2031–2049, doi:10.1175/JPO-D-13-0133.1.

Fer, I., M. Müller, and A. K. Peterson, 2015: Tidal forcing, energetics, and mixing near the Yermak Plateau. Ocean Sci.,1812-0792, doi:10.5194/os-11-287-2015.

Fer, I., R. Skogseth, and F. Geyer, 2010: Internal Waves and Mixing in the Marginal Ice Zone near the Yermak Plateau∗ . J. Phys. Oceanogr, doi:10.1175/2010JPO4371.1.

Foreman, M., 1978: Manual for tidal currents analysis and prediction. Pacific Marine Science Report 78-6

Gimbert, F., D. Marsan, J. Weiss, N. C. Jourdain, and B. Barnier, 2012: Sea ice inertial oscillations in the Arctic Basin. The Cryosphere, 6, 1187–1201, doi:10.5194/tc-6-1187-2012.

Gonella, J., 1972: A rotary-component method for analysing meteorological and oceanographic vector time series. Deep Sea Research and Oceanographic Abstracts, 19, 833–846, doi:10.1016/0011-7471(72)90002-2.

Haidvogel, D. B., and A. Beckmann, 1993: Numerical Simulation of Flow around a Tall Isolated Seamount. Part I: Problem Formulation and Model Accuracy, 23, 1736–1753, doi:10.1175/1520-0485(1993)023<1736:NSOFAA>2.0.CO;2.

Haidvogel, D. B., H. G. Arango, K. Hedstrom, A. Beckmann, P. Malanotte-Rizzoli, and A. F. Shchepetkin, 2000: Model evaluation experiments in the North Atlantic Basin: simulations in nonlinear terrain-following coordinates. Dynamics of Atmospheres and Oceans, 32, 239–281, doi:10.1016/S0377-0265(00)00049-X.

Holloway, G., and A. Proshutinsky, 2007: Role of tides in Arctic ocean/ice climate. J. Geophys. Res, 112, 3069–10, doi:10.1029/2006JC003643.

Hughes, K. G., and J. M. Klymak, 2019: Tidal Conversion and Dissipation at Steep Topography in a Channel Poleward of the Critical Latitude. J. Phys. Oceanogr, doi:10.1175/JPO-D-18-0132.1.

Hutchings, J. K., and P. Heil, 2012: Subsynoptic scale spatial variability of sea ice deformation in the western Weddell Sea during early summer. Journal of Geophysical Research.

Jakobsson, M., and Coauthors, 2012: The International Bathymetric Chart of the Arctic Ocean (IBCAO) Version 3.0. Geophys. Res. Lett, 39, doi:10.1029/2012GL052219.

Janout, M. A., and Y.-D. Lenn, 2014: Semidiurnal Tides on the Laptev Sea Shelf with Implications for Shear and Vertical Mixing. J. Phys. Oceanogr, 44, 202–219, doi:10.1175/JPO-D-12-0240.1.

Kowalik, Z., and A. Y. Proshutinsky, 1994: The Arctic Ocean Tides. American Geophysical Union (AGU), Washington, D. C, 22 pp.

Kozlov, I., V. Kudryavtsev, E. Zubkova, O. Atadzhanova, A. Zimin, D. Romanenkov, A. Myasoedov, and B. Chapron, 2017: SAR observations of internal waves in the Russian Arctic seas. IGARSS 2015 - 2015 IEEE International Geoscience and Remote Sensing Symposium, IEEE, 947–949.

Kulikov, E. A., 2004: Barotropic and baroclinic tidal currents on the Mackenzie shelf break in the southeastern Beaufort Sea. J. Geophys. Res, 109, 307–318, doi:10.1029/2003JC001986.

Lenn, Y.-D., T. P. Rippeth, C. P. Old, S. Bacon, I. Polyakov, V. Ivanov, and J. H lemann, 2011: Intermittent Intense Turbulent Mixing under Ice in the Laptev Sea Continental Shelf. J. Phys. Oceanogr, 41, 531–547, doi:10.1175/2010JPO4425.1.

Levine, M. D., C. A. Paulson, C. A. Paulson, and J. H. Morison, 1985: Internal Waves in the Arctic Ocean: Comparison with Lower-Latitude Observations. doi:10.1175/1520-0485(1985)015<0800:IWITAO>2.0.CO;2.

Losch, M., D. Menemenlis, J.-M. Campin, P. Heimbach, and C. Hill, 2010: On the formulation of sea-ice models. Part 1: Effects of different solver implementations and parameterizations. Ocean Modelling, 33, 129–144, doi:10.1016/j.ocemod.2009.12.008.

Luneva, M. V., Y. Aksenov, J. D. Harle, and J. T. Holt, 2015: The effects of tides on the water mass mixing and sea ice in the Arctic Ocean. J. Geophys. Res. Oceans, 120, 6669–6699, doi:10.1002/2014JC010310.

Marshall, J., A. Adcroft, C. Hill, L. Perelman, and C. Heisey, 1997: A finite-volume, incompressible Navier Stokes model for studies of the ocean on parallel computers. J. Geophys. Res. Oceans, 102, 5753–5766, doi:10.1029/96JC02775.

Martini, K. I., C. A. Stoudt, J. K. Hutchings, 2014: Near-Inertial Internal Waves and Sea Ice in the Beaufort Sea∗ . J. Phys. Oceanogr., doi:10.1175/JPO-D-13-0160.1.

Morison, J. H., C. E. Long, and M. D. Levine, 1985: Internal wave dissipation under sea ice. J. Geophys. Res. Oceans, 90, 11959–11966, doi:10.1029/JC090iC06p11959.

Mueller, R. D., L. Padman, M. S. D., S. Erofeeva, H. A. Fricker, and M. A. King, 2012: Impact of tide-topography interactions on basal melting of Larsen C Ice Shelf, Antarctica. Journal of Geophysical Research, 117.

Mueller, R. D., T. Hattermann, S. L. Howard, and L. Padman, 2018: Tidal influences on a future evolution of the Filchner–Ronne Ice Shelf cavity in the Weddell Sea, Antarctica. The Cryosphere, 12, 453–476, doi:10.5194/tc-12-453-2018.

Munk, W., 1997: Once again: once again—tidal friction. Progress in Oceanography, 40, 7–35, doi:10.1016/S0079-6611(97)00021-9.

Munk, W., and C. Wunsch, 1998: Abyssal recipes II: energetics of tidal and wind mixing. Deep-Sea Research Part I, 45, 1977–2010, doi:10.1016/S0967-0637(98)00070-3.

Nguyen, A. T., V. Ocaña, V. Garg, P. Heimbach, and J. M. Toole, 2017: On the benefit of current and future ALPS data for improving Arctic coupled ocean-sea ice state estimation. Oceanography, 30, doi:10.2307/26201850.

Padman, L., A. J. Plueddemann, R. D. Muench, and R. Pinkel, 1992: Diurnal tides near the Yermak Plateau. J. Geophys. Res. Oceans, 97, 12639–12652, doi:10.1029/92JC01097.

Padman, L., and C. Kottmeier, 2000: High-frequency ice motion and divergence in the Weddell Sea. J. Geophys. Res. Oceans, 105, 3379–3400, doi:10.1029/1999JC900267.

Padman, L., and S. Erofeeva, 2004: A barotropic inverse tidal model for the Arctic Ocean. Geophys. Res. Lett, 31, 53–54, doi:10.1029/2003GL019003.

Padman, L., M. R. Siegfried, and H. A. Fricker, 2018: Ocean Tide Influences on the Antarctic and Greenland Ice Sheets. Reviews of Geophysics, 56, 142–184, doi:10.1002/2016RG000546.

Padman, L., S. Howard, and R. Muench, 2006: Internal tide generation along the South Scotia Ridge. Deep Sea Research Part II: Topical Studies in Oceanography, 53, 157–171, doi:10.1016/j.dsr2.2005.07.011.

Pawlowicz, R., B. Beardsley, and S. Lentz, 2002: Classical tidal harmonic analysis including error estimates in MATLAB using T_TIDE. Computers & Geosciences, 28, 929–937, doi:10.1016/S0098-3004(02)00013-4.

Pnyushkov, A. V., and Coauthors, 2018a: Heat, salt, and volume transports in the eastern Eurasian Basin of the Arctic Ocean from 2 years of mooring observations. Ocean Sci, 14, 1349–1371. https://doi.org/10.5194/os-14-1349-2018.

Pnyushkov, A. V., and I. V. Polyakov, 2012: Observations of Tidally Induced Currents over the Continental Slope of the Laptev Sea, Arctic Ocean. J. Phys. Oceanogr, 42, 78–94, doi:10.1175/JPO-D-11-064.1.

Pnyushkov, A. V., I. V. Polyakov, V. V. Ivanov, Y. Aksenov, A. C. Coward, M. Janout, and B. Rabe, 2015: Structure and variability of the boundary current in the Eurasian Basin of the Arctic Ocean. Deep Sea Research Part I: Oceanographic Research Papers, 101, 80–97, doi:10.1016/j.dsr.2015.03.001.

Pnyushkov, A., I. V. Polyakov, L. Padman, and A. T. Nguyen, 2018b: Structure and dynamics of mesoscale eddies over the Laptev Sea continental slope in the Arctic Ocean. Ocean Sci, 14, 1329–1347, doi:10.5194/os-14-1329-2018.

Pollard, R. T., and R. C. Millard Jr., 1970: Comparison between observed and simulated wind-generated inertial oscillations. Deep Sea Research and Oceanographic Abstracts, 17, 813–821, doi:10.1016/0011-7471(70)90043-4.

Polyakov, I. V., and Coauthors, 2017: Greater role for Atlantic inflows on sea-ice loss in the Eurasian Basin of the Arctic Ocean. Science, doi:10.1126/science.aai8204.

Polyakov, I. V., and Coauthors, submitted: Transition to a new ocean mixing regime increases eastern Arctic sea ice loss to Atlantic Ocean heat.

Prinsenberg, S. J., and E. B. Bennett, 1989: Vertical Variations of Tidal Currents in Shallow Land Fast Ice-Covered Regions. 1268–1278, doi:10.1175/1520-0485(1989)019<1268:VVOTCI>2.0.CO;2.

Rainville, L., and R. A. Woodgate, 2009: Observations of internal wave generation in the seasonally ice-free Arctic. Geophys. Res. Lett, 36, 1487–5, doi:10.1029/2009GL041291.

Rippeth, T. P., Ben J Lincoln, Y.-D. Lenn, J. A. M. Green, A. Sundfjord, and S. Bacon, 2015: Tide-mediated warming of Arctic halocline by Atlantic heat fluxes over rough topography. Nature Geoscience 2015 8:3, 8, 191, doi:10.1038/ngeo2350.

Rippeth, T. P., V. Vlasenko, N. Stashchuk, B. D. Scannell, J. A. M. Green, Ben J Lincoln, Sheldon Bacon, 2017: Tidal conversion and mixing poleward of the critical latitude (an Arctic case study). Journal of Geophysical Research.

Rudels, B., E. P. Jones, L. G. Anderson, and G. Kattner, 1994: On the Intermediate Depth Waters of the Arctic Ocean. The Polar Oceans and Their Role in Shaping the Global Environment, Vol. 188 of Johannessen/The Polar Oceans and Their Role in Shaping the Global Environment, American Geophysical Union, Washington, D. C., 33–46.

Shchepetkin, A. F., and J. C. McWilliams, 2005: The regional oceanic modeling system (ROMS): a split-explicit, free-surface, topography-following-coordinate oceanic model. Ocean Modelling, 9, 347–404, doi:10.1016/j.ocemod.2004.08.002.

Simmons, H. L., R. W. Hallberg, and B. K. Arbic, 2004: Internal wave generation in a global baroclinic tide model. Deep Sea Research Part II: Topical Studies in Oceanography, 51, 3043–3068, doi:10.1016/j.dsr2.2004.09.015.

Timofeev, V. T., 1960: Water Masses of the Arctic Basin. Gidrometeoizdat, p.190.

Towns, J., and Coauthors, 2014: XSEDE: Accelerating Scientific Discovery", Computing in Science & Engineering, vol.16, no. 5, pp. 62-74, doi:10.1109/MCSE.2014.80

Wunsch, C., 1975: Internal tides in the ocean. Reviews of Geophysics, 13, 167–182, doi:10.1029/RG013i001p00167.

4

ARCTIC TIDAL CURRENT ATLAS

Till M. Baumann[1], Igor V. Polyakov[1], Laurie Padman[2], Andrey V. Pnyushkov[3]

1 *International Arctic Research Center and College of Natural Science and Mathematics, University of Alaska Fairbanks (UAF), Fairbanks, AK, USA and Finnish Meteorological Institute, Helsinki, Finland*

2 *Earth & Space Research, Corvallis, OR, USA*

3 *International Arctic Research Center, UAF, Fairbanks, AK, USA*

corresponding author: Till Baumann (tmbaumann@alaska.edu)

This chapter is prepared for submission to *Nature Scientific Data* and is structured according to their specifications.

Abstract

Tidal and wind-driven near-inertial currents play a vital role in the changing Arctic climate and ecosystem. We compiled over 300 available moored current observations taken over the last two decades throughout the Arctic to assemble a pan-Arctic atlas of tidal band currents. The atlas contains different tidal current products designed for the analysis of tidal parameters from monthly to inter-annual time scales. On shorter time scales, wind-driven inertial currents cannot be analytically separated from dominant tidal constituents. Thus, we include 10-30h band-pass filtered currents, containing all semidiurnal and diurnal tidal constituents as well as wind-driven inertial currents for the analysis of high-frequency variability of ocean dynamics. This allows for a wide range of possible uses, including local case studies of baroclinic tidal currents, assessment of long-term trends in tidal band kinetic energy and Arctic-wide validation of ocean models. Furthermore, this atlas may be a valuable tool for industrial applications such as fisheries, navigation and offshore construction. Here we describe the contents of the atlas and provide guidance for prospective users.

4.1 BACKGROUND AND SUMMARY

In the relatively quiet Arctic Ocean, tidal currents are often the dominant source of current variability and play an important role in shaping the Arctic Ocean hydrography and sea ice cover; see, for example, Kowalik and Proshutinsky (1994), Holloway and Proshutinsky (2007) and Luneva et al.(2015). Beyond their direct climate impact, tidal currents are a key element shaping the marine ecosystem with impacts ranging from creating the habitat of the intertidal zone to mixing of nutrients and plankton. Furthermore, information about tidal currents is used for many practical

applications, such as navigation (source), fisheries (source) and marine structures and operations.

Barotropic tidal models (e.g. Kowalik and Proshutinsky 1994; Padman and Erofeeva 2004) based on the depth-integrated momentum and continuity equations provide tide height and depth-averaged currents for major tidal constituents throughout the Arctic. These comparatively simple models show very little tidal activity (<0.5 cm/s) in the central Arctic deep basins, but strong amplitudes (>10 cm/s) over portions of the continental shelves and slopes.

Where barotropic tidal currents flow across steep slopes or rough topography in the presence of stratification, energy can be converted from barotropic to baroclinic (internal) tides whose energy finally dissipates in mixing processes (e.g. Wunsch 1975; Simmons et al. 2004). The importance of baroclinic tidal processes was highlighted, for example, by Luneva et al. (2015), who found that the addition of tidal currents to an atmospherically forced three-dimensional simulation reduced pan-Arctic sea ice volume by $\sim$15% . The authors attributed this sea ice reduction to the entrainment of warm subsurface Atlantic Water into the cold near-surface waters by increased surface stresses, and by upper-ocean shear instabilities from the combination of baroclinic tides and the atmospherically forced three-dimensional circulation. In contrast to barotropic tides, the generation, propagation and dissipation of baroclinic tidal waves are sensitive to stratification, mean flow, and energy losses through friction and mixing within the water column. They may, therefore, change substantially with variations in the background ocean state associated with weather-band and seasonal changes in forcing, ocean mesoscale variability (e.g. eddies) and as the Arctic Ocean changes on longer time scales (e.g. Carmack et al. 2015).

Despite their importance for the Arctic Ocean and its sea ice, many ocean general circulation models used for climate projections do not

currently feature full 3-D tidal currents. Hitherto, comprehensive Arctic oceanographic data sets are limited to hydrographic variables (salinity, temperature and density) (e.g. The Arctic Ocean Atlas, compiled by the US-Russian Environmental Working Group with data spanning the 1950s to the 1980s (1997)) with little or no information about the complex dynamics. With the increased use of moored Acoustic Doppler Current Profilers (ADCPs) in the Arctic in the last two decades or so, more and more high-resolution current observations (predominantly of the upper ocean) are becoming available. Using these data, detailed analysis of tidal current dynamics have been carried out at several specific places in the Arctic such as the Beaufort Sea shelf (Kulikov 2004), the Yermak Plateau (Padman et al. 1992; Fer et al. 2015), the Canadian Passage (Münchow and Melling 2008), the Laptev Sea (Janout and Lenn 2014) and the eastern Eurasian Basin (Pnyushkov and Polyakov 2012; Baumann et al. submitted). These studies emphasize the importance of tidal currents to local ocean dynamics. However, a pan-Arctic perspective on observed 3-D tidal currents is required, both to synthesize and expand our understanding of tidal dynamics and its interactions with hydrography and sea ice and to validate numerical models. Here we present a uniquely comprehensive atlas of tidal currents from available moored current meter records spanning the past two decades in all sectors of the Arctic Ocean. The aim is to provide a data set enabling both, local in-depth analysis of time-depth dependent tidal currents as well as Arctic-wide reference points constraining model simulations. Furthermore, long time series may be used to identify and analyze trends of tidal-band current dynamics.

4.2 METHODS

4.2.1 *Data acquisition and pre-processing*

One of the targets for this atlas was to collect all available Arctic current profile records of at least 1-year length and 1 h resolution to resolve tidal oscillations. With the help of many colleagues (see list of contributors in table A4.1), we gathered over 300 records from all sectors of the Arctic, spanning the last two decades (Fig. 4.1).

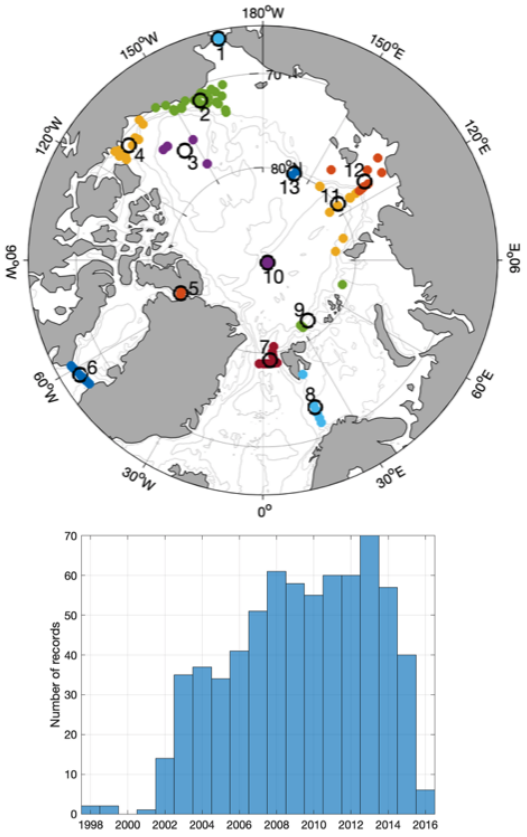

Figure 4.1: Spatial and temporal distribution of current velocity records contained in the atlas. Top: Map showing locations of the records (colored dots). Colors indicate grouping utilized for visualizations. Black circles show the centroid location and number of each cluster. Bottom: Histogram of record distribution over time.

the bulk of the observations stems from ADCPs of TELEDYNE RD Instruments (RDI) with the 300kHz variant being the most commonly used. ADCPs generally provide vertical profiles of horizontal velocity with a vertical resolution and range depending on the instruments frequency and set-up. In an Arctic application (with relatively few backscattering particles outside the shallow shelf regions), typical vertical resolutions range from 0.5 to 5 m with vertical range spanning 40 m to ∼300 m for 1200kHz and 75kHz ADCPs. Typical temporal resolution of the records is 1h (although some have a higher resolution of 15-30 min). While vertical resolution and range vary substantially between models of different frequencies, the expected accuracies for speeds and directions are generally similar and are given as ± 0.5 cm/s and $\pm 2^\circ$ for vertical averaging bin sizes of 2 m for the 300kHz ADCPs. Known issues with moored ADCP records are discussed in the section "Technical Validation". In the Barents Sea Opening region, where ADCP records were sparse, we complemented the atlas with data from Recording Current Meters (RCMs), which work analogous to mechanical anemometers and provide point-observations of currents at the depth they are moored. Aanderaa RCM7 have a starting velocity of 2 cm/s with expected accuracies of 1 cm/s or 4% of the actual speed (whichever is higher) and the accuracy for the direction is expected to be 5° (Aanderaa Instruments data sheet).

The data used in this atlas came from many different sources in many different formats. The number of steps required to arrange the data in a common format depended on the original format and state of processing. Generally the first step was to ensure a uniform grid of time and depth. It was not uncommon for the records to have a drifting clock or otherwise inconsisting time spacing. If the original time vector was not equally spaced throughout the length of the deployment, the data was interpolated on a synthetic time vector with 1h time interval. Data gaps of more than 1h were kept (and filled with NaNs). If depth information was available (either from

the pressure sensor of the ADCP itself or nearby deployed CTD sensors), the depth of each ADCP bin was adjusted at every time step. The data was then interpolated on a uniform pressure vector (spreading the whole depth range covered by observations while maintaining the original increment) at each time step. If no pressure record was available, the instrument deployment depth was taken and all bin-depths assumed to be constant over time. Since some depth information came in pressure units (dbar), others in distance from the surface (meters) without necessarily providing CTD data for conversion, we decided to treat any depth information as pressure. The error associated with this approximation is $\sim$1.1% of the water depth. Since most records only cover the upper ocean (<100 m), the error is small and tends to be less than 1 m.

The chosen standard format contained the following information:

- Time vector (days since 1.1.0000)
- Pressure vector (dbar)
- Current velocity (cm/s) arranged as matrix of the size length(time) x length(pressure) with u and v components as complex number.
- Latitude/longitude
- Mooring name
- Instrument type
- Institution of origin
- Region of deployment

A unique filename was created for each record consisting of region, mooring name, instrument type and deployment years (e.g. lapt_1893_ADCP300_2013-14).

4.2.2 *Tidal analysis*

We analyzed the current velocities using the T_TIDE Matlab toolbox (Pawlowicz et al. 2002), which is based on tidal analysis methods described by Foreman (1978). T_TIDE performs a harmonic analysis based on the known frequencies for up to 69 tidal constituents and calculates all relevant tidal ellipse parameters (major and minor axis amplitudes, orientation, sense of rotation direction and phase) with their confidence intervals.

The number of resolvable constituents is determined by the length of the time series. In most ocean environments, the bulk of the total tidal variance is in eight constituents, four semidiurnals (M_2, S_2, K_2, N_2) and four diurnals (O_1, K_1, P_1, Q_1). Tidal analysis on shorter windows ($<\sim$180 days, as commonly available from temporary tide gauge deployments, and as used in this atlas), report the combination of S_2 and K_2 as S_2 only, while K_1 and P_1 are reported as K_1. For barotropic tide heights, where amplitudes and phases are stable in time, these pairs can be separated in short records by "inference" (Foreman 1978; Pawlowicz et al. 2002). In the present analysis, however, we expect that much of the tidal energy is in time-varying baroclinic modes where the assumptions required for inference may not apply. For analysis of short records (30-day and 90-day analyses), we therefore define the inseparable sum of K_1 and P_1 as K_1* and the sum of S_2 and K_2 as S_2*.

The tidal parameters presented in this atlas are based on tidal analysis at each depth level over three different time periods: 30-day sliding windows (with original time increment), 90-day sliding windows (with 5 day increment) and the whole time series.

The rationale for these three different approaches is as follows:

30-day sliding windows, run over the whole record at each depth level. This analysis is standard practice and yields tidal parameters at the same time and depth coordinates as the raw data (excluding the first and last 15

days of each record). A major caveat of this analysis is the potential effect of wind-driven inertial currents that may influence and even dominate tidal analysis in the upper ocean (see "Technical Validation"). Because of the unknown, but potentially extensive effect of inertial currents on individual constituents, we recommend not to rely on this product for upper ocean (< ∼50 m) applications.

90-day analysis yields tidal parameters averaged over a longer period of time, substantially reducing the influence of short-term synoptic wind influences on the harmonic analysis. This analysis is designed to allow for detailed analysis of individual tidal constituent ellipses and their variability over depth and time on sub-seasonal to inter annual time scales.

Whole time analysis yields a single set of ellipse parameters for each constituent and provides a long-term average view on tidal currents. This is designed to provide robust tidal information largely independent of short-term influences. We note that the outcome of this analysis is not equivalent to averaging any of the previously discussed analyses over the whole time period. Although differences in major axis amplitudes are often relatively small, other important ellipse parameters (such as phase and orientation) may differ substantially.

In addition to harmonic tidal analysis, tidal band currents (TBC) are defined as currents that are component-wise band-pass filtered for periods between 10 h and 30 h. This comprises all semi-diurnal and diurnal tidal constituents as well as wind-driven inertial currents. This method does not require any averaging or smoothing over time and thus provides the full spectrum of high-frequency current amplitude and variability.

4.3 DATA RECORDS

The atlas is archived as a collection of netCDF files, one for each record. The pathway to access the data is via the "table of inventory", a human-

and machine-readable table that provides all relevant meta-information (file name, mooring name, region, start and end date, position, estimated bottom depth, instrument type, depth range covered and institution of origin), so that prospective users can efficiently identify the records suitable for their needs. Upon publication, the data will be accessible on the National Science Foundation Arctic Data Center (https://arcticdata.io).

4.4 TECHNICAL VALIDATION

4.4.1 *Instrument-related quality assessment*

ADCP measurements close to the surface inherently suffer from contaminations due to surface reflections of sidelobe energy. This error depends on the range, bin size and beam angle of the ADCP. Since for many records, precise instrument information was unavailable, we decided to provide a mask blanking out the top 10% of the range of any records that reach the surface.

In order function, ADCP measurements depend on particles drifting in the water column that reflect the ADCP's acoustic signal back to the instrument, where the Doppler shift of the signal is determined to calculate velocities. However, in the relatively quiescent Arctic, the amount of suspended particles can be very low, especially during winter, when biological primary production effectively halts. With weak echoes, the ranges of ADCP profiles are substantially reduced: RDI expects >150 m range for 300kHz ADCPs but in the Arctic, their effective range is ∼50-60 m. Exceedingly low back scatter amplitudes may also lead to greater errors for speed and direction. Most records compiled in this atlas do not provide the extensive metadata to investigate this issue consistently, but erroneous data is commonly discarded during standard processing procedures.

4.4.2 *Influence of wind-driven inertial currents on tidal analysis*

As noted by Baumann et al. (submitted), wind-driven inertial currents may substantially impact T_TIDE harmonic analysis in the Arctic, where the local inertial frequency lies between (and thus very close to) the two major semidiurnal tidal constituents M_2 and S_2. Baumann et al. (submitted) demonstrated the impact of wind-driven inertial currents on tidal analysis using a damped-slab model with two different idealized mixed layer depths (10 m and 50 m). Results suggested that effects are greatest for the 10-m SML case, which is representative of ice-free summers when surface mixed-layer depths are shallow. For the deeper 50-m case, the influence of wind-driven inertial currents is much reduced.

Here we use the same damped-slab model (described in Baumann et al. (submitted)) for reanalysis wind and ice conditions at a location offshore of the Laptev Sea continental slope to demonstrate the different effects on 30-day, 90-day and full-time tidal analysis. Due to the side-lobe effect alluded to above, much of the upper ocean observations throughout the atlas cannot be used, so that only 6% of the valid data are located within the top 10 m, whereas 54% lie between 10 and 50 m. Thus the 50-m SML case of the slab model is considered to be the more representative condition for this atlas.

Using an idealized tidal signal with seasonal variability similar to observed amplitudes in the Laptev Sea and upper eastern Eurasian continental slope region (compare Fig. 4.3), onto which slab-model-simulated inertial currents are added, we show the output of T_TIDE tidal analysis in Fig. 4.2. The 30-day analysis is marked by some substantial short-term variability, which is (in this case) erroneously attributed to tidal constituents. As a consequence, the range of currents attributed to tides, a simple measure of tidal variability of time, amounts to 8 cm/s instead of the "true" 6 cm/s (due to 3 cm/s seasonal amplitude), which constitutes an overesti-

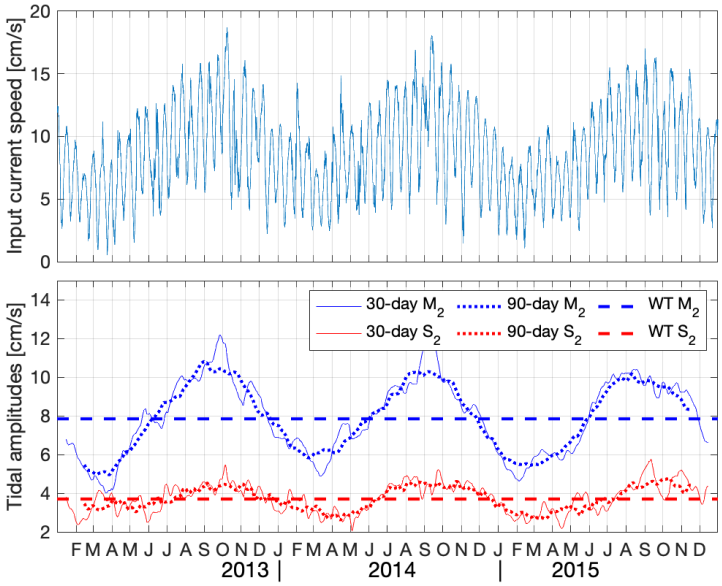

Figure 4.2: Tidal analysis using different window lengths performed on an artificial time series. The time series is constructed to resemble realistic conditions found at the eastern Eurasian continental slope (see Baumann et al. submitted) and consists of two cosine oscillations at M_2 and S_2 frequency (amplitudes are 8 cm/s and 4 cm/s, respectively, both of which undergo a seasonal cycle represented as cosine function with 360-day period and amplitude of 3 cm/s and 1 cm/s for M_2 and S_2, respectively). To this, we added inertial oscillations (average amplitude $\sim$2 cm/s) simulated from a slab-model with 50-m SML (see Baumann et al. submitted for details). The 30-day and 90-day analyses predominantly follow the seasonal cycle, but noise has a substantial impact on the 30-day analysis. Some minor distortions of the seasonal signal are also visible for the 90-day analysis. The whole time analysis produces a single set of tidal ellipse parameters with the major axis amplitude almost exactly matching the input.

mation of 33% . The 90-day analysis provides a clear seasonal cycle (and a range of 6.2 cm/s, i.e. 3% overestimation) and the whole time analysis provides tidal amplitudes matching those of the input, despite variability through seasonality and wind-driven inertial currents. We note that in conditions where inertial currents are continously strong (>half of tidal amplitude), inertial impact is high on the 90-day and even whole-time analysis as well. However, these conditions are only expected very close to the surface during ice-free summers.

4.5 USAGE NOTES

The wide range of possible applications (including climate modelling, fisheries, offshore construction, etc.) requires high flexibility of the atlas. Using the "table of inventory" described in "Data Records", users can easily identify the records useful to their specific task.

Large scale or pan-Arctic application may benefit from a grouping of a number of (or all) records using clustering algorithms. Due to the strong dependence of tidal currents on topography, we recommend that clustering take into account water depth as well as geographical location. An example of location and depth dependent clustering of all records is presented in Fig. 4.1. We use this clustering to illustrate pan-Arctic tidal current properties in the following section.

4.5.1 *Choosing the right atlas product*

4.5.1.1 *Whole-time analysis: Comparison to barotropic tidal models*

Barotropic tidal models are comparatively simple models that predict tidal currents and individual constituent ellipse parameters from gravitational tidal forcing and oceanic topography (Kowalik and Proshutinsky 1994; Padman and Erofeeva 2004). Results from these models are still widely used in scientific research and for practical applications. The vertically averaged results of whole-time tidal analysis are the closest approximation to barotropic tidal currents in the atlas. Using the clustering shown in (Fig. 4.1), the pan-Arctic spatial variability of major axis amplitudes for the six leading diurnal and semidiurnal constituents can be visualized (Fig. 4.3). Not only tidal amplitudes, but also the relative contribution of the individual constituents vary widely across the Arctic. Strongest tidal currents are observed in the Canadian Passage (cluster #5) and Davis

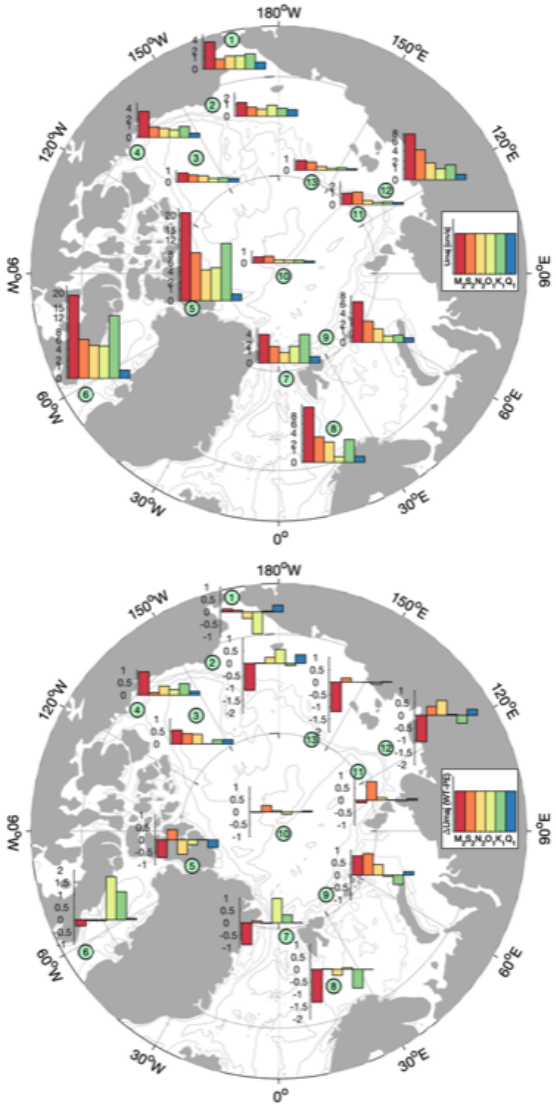

Figure 4.3: Time-and depth averaged tidal amplitudes and their differences compared to a barotropic tidal model across the Arctic. Top: Major axis amplitudes of tidal constituents (U_{maj}) from whole-time analysis. Amplitudes are averaged vertically and over all records within each each cluster. Bottom: Difference of U_{maj} for tidal constituents from whole-time analysis (see Fig. 4.3) and barotropic model output. Model data stems from Padman and Erofeeva (2004).

Strait (cluster #6), with M_2 major axis amplitudes exceeding 20 cm/s followed by the diurnal K_1 constituent with ∼12 cm/s. Other regions of substantial tidal activity include the Barents Sea Opening (cluster #8) with ∼12 cm/s for the leading M_2 tide and very minor diurnal contribution,

the western Eurasian Basin continental slope (cluster #9) and the Laptev Sea (cluster #12) with dominating M_2 amplitudes of 6-8 cm/s. While the Yermak plateau is known for intensive (diurnal) tidal currents (Padman et al. 1992; Fer et al. 2015), in this visualization it is clustered together with Fram Strait moorings, where the tidal signal is much weaker, yielding an average of only ∼4cm/s. Throughout deep basins (clusters #10, #11, #13 and #3) and the Pacific side shelves and continental slopes (clusters #1, #2 and #4), tidal amplitudes are much weaker compared to the Atlantic side continental slopes, barely reaching 4 cm/s. These data may be used to validate barotropic tidal models. For example, differences between the atlas and output from the model from Padman and Erofeeva (2004) (taken at the locations of every record in the atlas and performing the same averaging within each cluster) are relatively small (<2 cm/s, Fig. 4.3) with no systematic bias, and thus confirm the performance of the model.

4.5.1.2 *90-day analysis: Spatio-temporal structure and variability of tidal parameters*

While barotropic tidal models provide general tidal information, which is invariant over depth and time, this atlas additionally provides information on the spatio-temporal variability of tidal currents. 90-day analysis resolves the variability for individual tidal constituents on timescales from three months to years (depending on the length of the record) and includes the seasonal cycle. The range of this relatively low-frequency temporal variability is on average 5.4 cm/s or 119% of the mean (barotropic) amplitude across all records, with maxima in several cases exceeding 400% (Fig. 4.4). In absolute terms, even in regions with low average tidal amplitude (clusters #1-4), temporal variability can lead to M_2 tidal amplitudes exceeding 5 cm/s (while wind-driven inertial influence cannot be categorically excluded, at 50 m depth the influence should be negligible). Smallest variability is found in cluster #10, at the North Pole, where tidal currents

never exceed 2 cm/s (interestingly, the records within the deep Beaufort Sea (cluster #3) show a greater variability, sometimes exceeding 5 cm/s). Where tidal currents are strong, temporal variability is high as well, but its range is relatively smaller compared to the average amplitude. A standout region for high variability of relatively strong tidal currents is cluster #12, comprising the Laptev Sea and the eastern Eurasian Basin continental slope and was extensively discussed in Baumann et al. (submitted). Fig. 4.4 further demonstrates that the difference between records within a cluster in most cases exceeds temporal variability within a record, highlighting the great spatial variability of tidal currents.

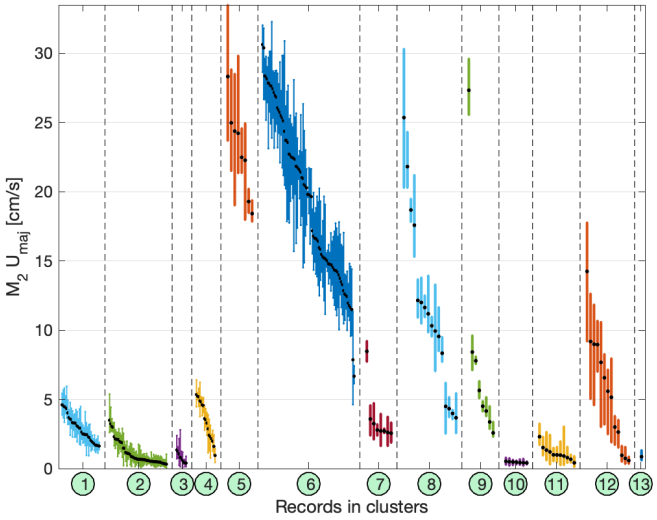

Figure 4.4: Spatio-temporal variability of tidal currents, illustrated by the range of M_2 U_{maj} (from 90-day analysis, at 50 m depth) for each record in each cluster. The records within each cluster are sorted by average U_{maj} (black dots). For readability, horizontal plotting space was stretched for clusters with a smaller number of records (clusters #5 and #7-#13).

The vertical structure (and thus shear) of baroclinic tidal currents is of major interest for the investigation of oceanic mixing processes. Tidal mixing can be extensive regionally (Holloway and Proshutinsky 2007; Janout and Lenn 2014; Fer et al. 2015; Padman et al. 1992) and was found to directly impact the sea ice cover in model simulations (e.g. Luneva et al.

2015). The vertical structure of M_2 major axis amplitudes varies regionally across the Arctic (Fig. 4.5). While cluster-average profiles cannot be used to identify mixing processes, they may indicate the regional tendency for baroclinicity. While some regions exhibit very barotropic profiles with little vertical structure (clusters #4, #7, #8, #10 and #13), others show a clear vertical change, with surface amplification (clusters #1, #2, #3 and #11) or other structures (clusters #5, #6 and #12).

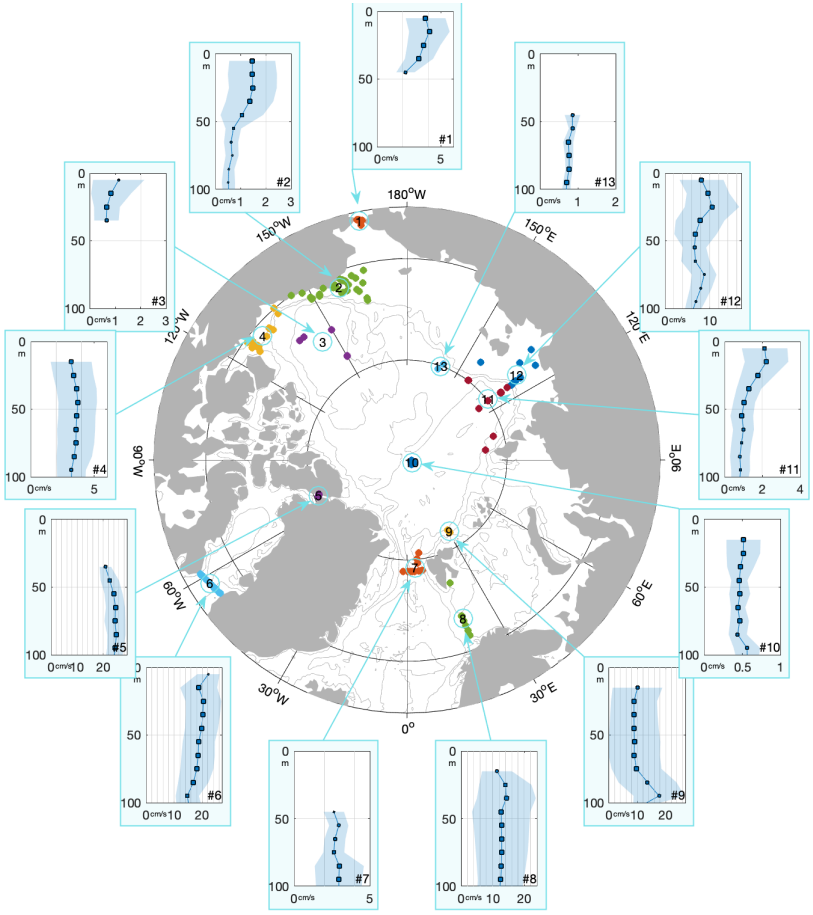

Figure 4.5: Cluster-average profiles of M_2 major axis amplitudes over the top 100 m. Averages were taken over 10 m bins with squares in the profiles showing the center of the bins and the sizes reflect the relative number of measurements in that bin. Shading denotes $\pm$ 1 standard deviation. The (linear) x-axis scales are different in each plot, but the vertical grid lines are always spaced by 2 cm/s.

4.5.1.3 *Tidal band currents: High-frequency variability and kinetic energy*

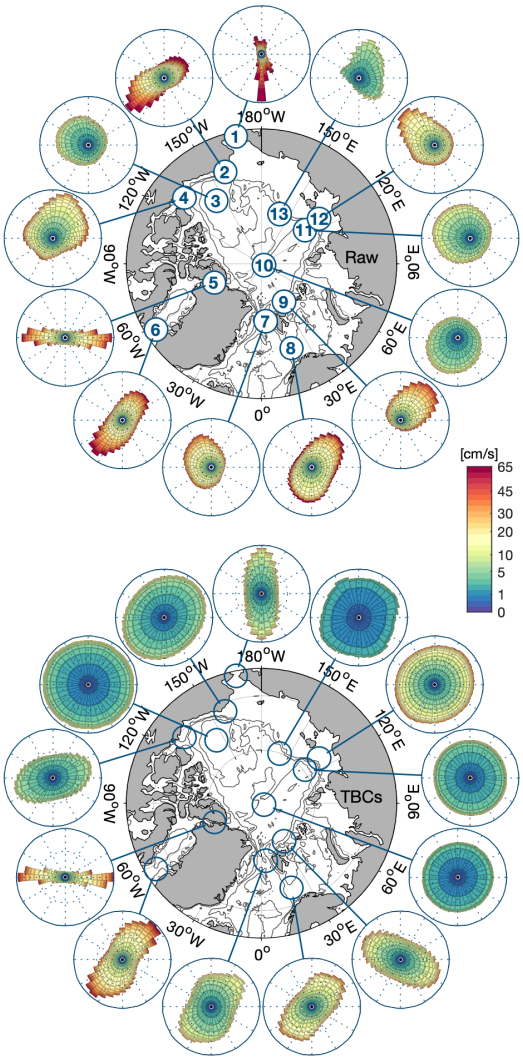

Figure 4.6: Regional current roses for observed raw (top) and tidal band currents (TBC, bottom). The roses are aligned with the true north of their respective centroid location (i.e. they fit in the map as they are without further rotation) and contain all observations within each cluster. The length of each 10° bin is proportional to the percentage of data within this bin. Speeds are marked by a nonlinear color scale.

Tidal band currents (TBCs) provide the full spectrum of amplitudes and variability exerted by the combination of wind-driven inertial and tidal currents. Since there is currently no way to separate the two components analytically, their properties have to be assessed jointly (however,

as discussed in "Technical validation", below ∼50 m depth, direct impact of wind-driven inertial currents is expected to be small). The relative importance of TBCs relative to the full spectrum of observed raw currents across the Arctic can be seen in Fig 4.6. Despite regionally strong currents in the Pacific sector of the Arctic (>50 cm/s at clusters #1, #2 and #3), TBCs are small throughout the region, barely reaching 10 cm/s. In the Atlantic sector, amplitudes of TBCs are often comparable to raw current amplitudes (clusters #5, #6, #8 and #12), indicating that tidal and inertial currents are the defining characteristics of the dynamics in these regions. Fig. 4.6 further reveals that TBCs can have a directional structure that fundamentally differs from the raw background currents (clusters #4, #7 and #9), likely caused by the interaction between tides and topographic features.

4.5.2 *Concluding remarks*

We here present a pan-Arctic dataset of tidal currents. Tidal currents play a vital role in the Arctic climate and ecosystem. The goal of the atlas is to provide a tool that enables investigations for practical purposes as well as for gaining a deeper understanding of regional high-frequency dynamics in a changing Arctic Ocean. As a ground-truth for the modelling community, this may contribute to more reliable projections of future Arctic Ocean states. In order to maximize utility, we provide different tidal products for different applications:

- Whole-time tidal analysis (e.g. for comparison to barotropic tidal models)
- 90-day tidal analysis (e.g. for the analysis of seasonal to interannual variability of tidal currents)

- 30-day tidal analysis (e.g. for intra-annual variability; it is also widely used standard procedure for tidal analysis). We caution the user to mind the potentially dominating effect of wind-driven inertial currents on tidal parameters in this product.
- Tidal band currents (TBCs, band-pass filtered over 10-30h), e.g. for analysis of high frequency variability without distinguishing between wind-driven inertial and tidal origin)

We expect that this atlas will find broad practical and scientific applications.

4.6 ACKNOWLEDGEMENTS

Analyses presented in this paper are supported by NSF grants 1249133 and 1249182. TMB was supported in part by a UAF Global Change Student Research Grant award with funds from the Cooperative Institute for Alaska Research.

4.7 AUTHOR CONTRIBUTIONS

TMB: Data processing, assembly of atlas and the data descriptor.
IVP & LP: Supervision of the processing and the data descriptor writing.
AVP: Collection of raw data.

The authors declare no competing interests.

4.8 APPENDIX: DATA CONTRIBUTIONS

Table A4.1: List of data contributors

Contact	**Institute**	**Online data access**
Arild Sundfjord	Norwegian Polar Institute	https://doi.org/10.21334/npolar.2017.73d0ea3a
Seth Danielson	University of Alaska Fairbanks	/
Leah McRaven	Norwegian Polar Institute, Woods Hole Oceanographic Institute	doi:10.18739/A25C41, doi:10.18739/A2956Z, doi:10.18739/A2DV9X, doi:10.18739/A21P1R
Bill Williams	Fisheries and Oceans Canada	/
Craig Lee	Applied Physics Laboratory	doi:10.18739/A21S72
Peggy Sullivan	Pacific Marine Environmental Laboratory	gov.noaa.nodc:0149848
Yasushi Fukamachi	Hokkaido Univeristy	doi:10.18739/A2MT1D
Laura de Steur	Norwegian Polar Institute	/
Harper Simmons	University of Alaska Fairbanks	doi:10.18739/A2X911

Rebecca Woodgate	Applied Physics Laboratory	http://psc.apl.washington.edu/HLD/Bstrait/Data/BeringStraitMooringDataArchive.html#Ascii_data, doi:10.5065/D64747X3
Rick Krishfield, Andrey Proshutinsky	Woods Hole Oceanographic Institute	https://www.whoi.edu/beaufortgyre
Andreas Munchow	University of Delaware	doi:10.18739/A2RR77, doi:10.18739/A23K67
Igor Polyakov	University of Alaska Fairbanks	doi:10.18739/A2N37Rm, doi:10.18739/A2HT2GB80
Markus Janout	Alfred Wegener Insitute	/
Roger Andersen	Applied Physics Laboratory	doi:10.5065/D6P84921
Robert Pickart	Woods Hole Oceanographic Institute	doi:10.5065/D6J964FR
Randi Ingvaldsen	Institute for Marine Research	/
Ilker Fer	University of Bergen	http://thredds.met.no/thredds/catalog/data/UiB/StorfjordADCP/catalog.html
Jean-Claude Gascard	Pierre and Marie Curie University, LOCEAN	doi:10.17882/51023

4.9 REFERENCES

Baumann, T.M., Polyakov, I.V., Padman, L., Danielson, S., Fer, I., Howard, S., Hutchings, J., Janout M., Nguyen, A., Pnyushkov, A.V., submitted. Semidiurnal Dynamics in the Arctic Ocean's Eastern Eurasian Basin. Journal of Physical Oceanography.

Carmack, E., and Coauthors, 2015: Toward Quantifying the Increasing Role of Oceanic Heat in Sea Ice Loss in the New Arctic. Bull. Amer. Meteor. Soc, 96, 2079–2105, doi:10.1175/BAMS-D-13-00177.1.

Environmental Working Group, 1997: Joint U.S.-Russian Atlas of the Arctic Ocean, Version 1. L. Timokhov and F. Tanis, Eds.

Fer, I., M. Müller, and A. K. Peterson, 2015: Tidal forcing, energetics, and mixing near the Yermak Plateau. 1812-0792, doi:10.5194/os-11-287-2015.

Foreman, M., 1978: Manual for tidal currents analysis and prediction. 1 pp.

Holloway, G., and A. Proshutinsky, 2007: Role of tides in Arctic ocean/ice climate. J. Geophys. Res, 112, 3069–10, doi:10.1029/2006JC003643.

Janout, M. A., and Y.-D. Lenn, 2014: Semidiurnal Tides on the Laptev Sea Shelf with Implications for Shear and Vertical Mixing. J. Phys. Oceanogr, 44, 202–219, doi:10.1175/JPO-D-12-0240.1.

Kowalik, Z., and A. Y. Proshutinsky, 1994: The Arctic Ocean Tides. American Geophysical Union (AGU), Washington, D. C, 22 pp.

Kulikov, E. A., 2004: Barotropic and baroclinic tidal currents on the Mackenzie shelf break in the southeastern Beaufort Sea. J. Geophys. Res, 109, 307–318, doi:10.1029/2003JC001986.

Luneva, M. V., Y. Aksenov, J. D. Harle, and J. T. Holt, 2015: The effects of tides on the water mass mixing and sea ice in the Arctic Ocean. J. Geophys. Res. Oceans, 120, 6669–6699, doi:10.1002/2014JC010310.

Münchow, A., and H. Melling, 2008: Ocean current observations from Nares Strait to the west of Greenland: Interannual to tidal variability and forcing. j mar res, 66, 801–833, doi:10.1357/002224008788064612.

Padman, L., A. J. Plueddemann, R. D. Muench, and R. Pinkel, 1992: Diurnal tides near the Yermak Plateau. J. Geophys. Res. Oceans, 97, 12639–12652, doi:10.1029/92JC01097.

Padman, L., and S. Erofeeva, 2004: A barotropic inverse tidal model for the Arctic Ocean. Geophys. Res. Lett, 31, 53–54, doi:10.1029/2003GL019003.

Pawlowicz, R., B. Beardsley, and S. Lentz, 2002: Classical tidal harmonic analysis including error estimates in MATLAB using T_TIDE. Computers & Geosciences, 28, 929–937, doi:10.1016/S0098-3004(02)00013-4.

Pnyushkov, A. V., and I. V. Polyakov, 2012: Observations of Tidally Induced Currents over the Continental Slope of the Laptev Sea, Arctic Ocean. J. Phys. Oceanogr, 42, 78–94, doi:10.1175/JPO-D-11-064.1.

Simmons, H. L., R. W. Hallberg, and B. K. Arbic, 2004: Internal wave generation in a global baroclinic tide model. Deep Sea Research Part II: Topical Studies in Oceanography, 51, 3043–3068, doi:10.1016/j.dsr2.2004.09.015.

Wunsch, C., 1975: Internal tides in the ocean. Reviews of Geophysics, 13, 167–182, doi:10.1029/RG013i001p00167.

5

CONCLUSIONS

In this dissertation, I present the results of the research I conducted in collaboration with several colleagues. Our investigations into the response of major modes of eastern Arctic Ocean variability to climate change include the analysis of the hydrographic seasonal cycles observed at the eastern Eurasian Basin continental slope and semidiurnal current dynamics in the same region. To facilitate further investigations into high-frequency current variability in the ocean, we assembled a pan-Arctic tidal current atlas. In the following, the major results of the three previous chapters are briefly summarized.

5.1 SUMMARY OF THE CHAPTERS

In chapter 2, we analyze the complex pattern of seasonality observed at the eastern Eurasian Basin. In the upper ocean in the deep eastern Eurasian Basin, wintertime cooling and salinification due to brine rejection during sea ice formation impact the upper ∼80 m of the water column. However, the greatest seasonal change is observed over the continental slope, where the Arctic Circumpolar Boundary Current is strongest and warm Atlantic Water is separated from cold shelf water masses by a hydrographic front. Due to a combination of seasonal advection changes, lateral front movement and upwelling, this region is subject to a strong seasonal cycle of temperature down to ∼ 600 m depth.

Finally, we observed a seasonal vertical displacement of isopycnals within the halocline of up to 36 m throughout large parts of the area with seasonal sea level changes being the likely driver.

In chapter 3, we conduct extensive analyses of two-year time series of upper-ocean currents from the same moorings used in chapter 2, supplemented with a slab model of surface mixed layer (SML) near-inertial response to realistic wind stress variability and a three-dimensional baroclinic tide model. Semidiurnal-band currents (SBCs, 10-14 h period) are a major contributor to current dynamics in the eastern EB region. During ice-free summer months, SBCs are strongly amplified in the upper $\sim$30 m, reaching amplitudes in excess of 40 cm/s far offshore in the eastern EB. During winter, the depth of strong SBCs varies, following the seasonal deepening and spring shoaling of the pycnocline.

Models of inertial currents in the SML and baroclinic tide generation and propagation suggest that, while the wintertime SBCs appear to be predominantly of tidal origin, observed large near-surface SBCs in summer in the deep basin are caused primarily by wind forcing of inertial oscillations, possibly with some contribution from baroclinic tidal currents. The close proximity of the inertial period to periods of energetic semidiurnal tides, and the expected variability of inertial and tidal current phases and amplitudes, precludes the empirical separation of these two signals.

In chapter 4, we present a uniquely comprehensive atlas of tidal currents we compiled from available moored current meter records spanning the past two decades in all sectors of the Arctic Ocean. The aim is to provide a data set enabling both, local in-depth analysis of time-depth dependent tidal currents as well as Arctic-wide reference points constraining model simulations. Furthermore, individual long time series exceeding one decade may be used to identify and analyze trends of tidal-band current dynamics.

5.2 RELEVANCE IN THE CONTEXT OF ARCTIC CHANGE

While the Pacific side of the Arctic Ocean is changing towards a more stable and less dynamic regime, the opposite is true for the Atlantic side. Ongoing *atlantification* of the eastern Arctic is both impacting and impacted by the major modes of oceanic variability which include seasonal cycles and semidiurnal current dynamics. A central feature of the recent change is the demise of sea ice, which is partly due to the observed vertical heat fluxes through the halocline; a quintessentially seasonal phenomenon (Polyakov et al. 2017). In this dissertation we show that seasonal variability is a major factor governing hydrographic properties as well as high-frequency dynamics in the region. Several processes and mechanisms we described are likely connected to the ongoing atlantification. The seasonality we observed in the halocline was stronger than previously documented (Dmitrenko et al. 2009), which implies that the associated vertical displacement of isopycnals has also been increasing. It seems plausible that this process may be linked to the observed increased heat fluxes through the halocline. Since we identified seasonal sea level change as a likely driver behind the seasonal isopycnal displacement, this would add a new aspect to the impact of oceanic heat on sea ice.

Furthermore, the large seasonal temperature difference of up to 1.4° C reaching deep into the ocean in the vicinity of the hydrographic front on the continental slope has a substantial impact on stratification. Combined with the overall warming trend in the eastern Arctic region, this may point towards an increased role of temperature in determining seawater density (e.g. Carmack 2007; Timmermans et al. 2016). Further research is needed to investigate these possibilities.

The rapid changes in sea ice conditions in recent years with prolonged periods free of high-concentration sea ice have a dramatic effect on semidiurnal current dynamics. During ice-free summers, wind-driven inertial

currents are strongly amplified and can reach >40 cm/s far offshore in the deep basin. The shear associated with these vigorous currents is expected to cause vertical mixing, which may enhance vertical heat fluxes and thus impede sea ice formation; a positive feedback loop. Furthermore, hydrographic changes impact the creation and propagation of baroclinic tidal currents and may thus lead to spatial and temporal changes of dynamical hotspots in the ocean. Dedicated model simulations will be necessary to assess specific regional impacts.

5.3 BROADER IMPACTS

From a biological perspective, much of the Arctic Ocean is an ecosystem where primary productivity is limited by the availability of nutrients, due to strong upper ocean stratification, and light, due to sea ice (plus snow) cover. In the changing eastern Arctic Ocean, both of these physical limitations are relaxing (e.g. Ardyna et al. 2014; Bluhm et al. 2015). In particular, the vigorous semidiurnal dynamics we observe during increasingly ice-free summers are a pathway to mixing and thus vertical transport of nutrients into the euphotic zone, enabling more primary production, even far away from the continental slope and known topographic hot spots. Additionally, ever-receding and thinning sea ice cover reduces the summertime light limitation.

Our area of study at the eastern EB continental slope coincides with the region of some of the highest zooplankton biomass in the Arctic due to the Atlantic inflows within the Arctic Circumpolar Boundary Current (Kosobokova et al. 2010; Bluhm et al. 2015). The vertical distribution of these zooplankton is unusually shallow in the Arctic Ocean (most biomass is within ∼100 m (e.g. Kosobokova et al. 2010) instead of ∼200 m as commonly found in the world ocean (Vinogradov, 1970), which has been linked in part to strong stratification. We speculate that the increasing

seasonal variability of upper ocean and halocline hydrography, together with generally decreasing stratification in this region may vertically expand the zooplankton habitat.

In the global climate system, the Arctic is a disproportionately important player. Receding sea ice cover leads to enhanced air-sea interactions and amplifies the role of the Arctic Ocean in climate change. As the Arctic Ocean is rapidly evolving, reaching states beyond historical precedence, numerical model simulations are the only viable tools to provide projections of future climate conditions. However, numerical models can only be as good as our understanding of the processes shaping the system and its variability. Hitherto, seasonal processes in the eastern EB are strongly underestimated in numerical models (Lique and Steele 2012). This work provides a detailed account of the different seasonal processes that govern the distribution and variability of hydrographic properties.

A central conundrum in numerical simulations is the representation of mixing in the ocean. Diapycnal mixing is believed to be a driver behind the increasing vertical heat fluxes in the eastern Arctic, with strong implications for the sea ice cover. Mixing processes generally occur on time and space scales beyond model resolution and thus cannot be directly simulated but depend on parameterizations fed by the relevant larger scale variables such as stratification and currents dynamics. In this work, we show that semidiurnal dynamics, from both, wind-driven inertial current as well as baroclinic tides are vigorous in the region with great potential to contribute to mixing. However, models to date do not commonly include baroclinic tidal currents. The tidal atlas we describe in chapter 4 may be of great utility in this endeavour. Furthermore, since the inertial period in the Arctic is relatively short ($\sim$12h), the generation of inertial currents can be strongly hampered by insufficient temporal resolution of atmosphere-ocean coupling (wind forcing with a resolution of $<\sim$3 h is required). Addressing these issues will be an important step for climate

models towards more realistic representations of Arctic Ocean dynamics and improved projections.

The Arctic Ocean has changed fundamentally since the early Arctic Explorers first documented its properties while braving some of the harshest conditions on the planet. Arctic amplification of globally rising temperatures is likely to yield an effectively ice-free Arctic during summers within the next two and a half decades (Wang and Overland 2012) and soon, standard open-water cargo ships may be traversing the Arctic on a regular basis (Smith and Stephenson, 2013). Along with the changing sea ice cover, the internal hydrography and dynamics of the Arctic Ocean will evolve towards new and as of yet unknown states. The work presented in this dissertation provides new insights into some of the major modes of variability governing the changing eastern Arctic Ocean. These findings deepen our understanding of oceanic processes in the new Arctic and may contribute to more robust projections of future Arctic climate and ecosystem conditions.

5.4 REFERENCES

Ardyna, M., M. Babin, M. Gosselin, E. Devred, L. Rainville, and J. É. Tremblay, 2014: Recent Arctic Ocean sea ice loss triggers novel fall phytoplankton blooms. Geophys. Res. Lett, 41, 6207–6212, doi:10.1002/2014GL061047.

Bluhm, B. A., K. N. Kosobokova, and E. C. Carmack, 2015: A tale of two basins: An integrated physical and biological perspective of the deep Arctic Ocean. 1–33, doi:10.1016/j.pocean.2015.07.011.

Carmack, E. C., 2007: The alpha/beta ocean distinction: A perspective on freshwater fluxes, convection, nutrients and productivity in high-latitude seas. Deep Sea Research Part II: Topical Studies in Oceanography, 54, 2578–2598, doi:10.1016/j.dsr2.2007.08.018.

Dmitrenko, I. A., and Coauthors, 2009: Seasonal modification of the Arctic Ocean intermediate water layer off the eastern Laptev Sea continental shelf break. J. Geophys. Res, 114, 11, doi:10.1029/2008JC005229.

Kosobokova, K. N., R. R. Hopcroft, and H.-J. Hirche, 2010: Patterns of zooplankton diversity through the depths of the Arctic's central basins. Mar Biodiv, 41, 29–50, doi:10.1007/s12526-010-0057-9.

Lique, C., and M. Steele, 2012: Where can we find a seasonal cycle of the Atlantic water temperature within the Arctic Basin? J. Geophys. Res. Oceans, 117, n/a–n/a, doi:10.1029/2011JC007612.

Polyakov, I. V., and Coauthors, 2017: Greater role for Atlantic inflows on sea-ice loss in the Eurasian Basin of the Arctic Ocean. Science, doi:10.1126/science.aai8204.

Smith, L. C., and S. R. Stephenson, 2013: New Trans-Arctic shipping routes navigable by midcentury. PNAS, 110, E1191–E1195, doi:10.1073/pnas.1214212110.

Timmermans, M.-L., S. R. Jayne, M.-L. Timmermans, and S. R. Jayne, 2016: The Arctic Ocean Spices Up. http://dx.doi.org/10.1175/JPO-D-16-0027.1, 46, 1277–1284, doi:10.1175/JPO-D-16-0027.1.

Vinogradov, M.Y., 1970. Vertical Distribution of Oceanic Zooplankton. Israel Program for Scientific Translations, Jerusalem, 339 pp.

Wang, M., and J. E. Overland, 2012: A sea ice free summer Arctic within 30 years: An update from CMIP5 models. Geophys. Res. Lett, 39, 341, doi:10.1029/2012GL052868.